Imperial College of Science Technology and Medicine
Department of Electrical and Electronic Engineering
Optical and Semiconductor Devices Group

Reconfigurable optically-controlled waveguide for terahertz applications

by

Elpida Episkopou

Dipl.–Ing. in Electrical and Computer Engineering

A dissertation submitted in partial fulfillment of the requirements for the degree of Doctor of Philosophy of Imperial College London and the Diploma of Imperial College London

October 2014

To my family

Declaration of Originality

I hereby declare that I am the only author of this thesis and that, this is an original work and any material used from other resources has been appropriately referenced.

Table of Contents

Acknowledgment

First, I would like to thank my supervisors Dr Stepan Lucyszyn and Prof. Andrew S. Holmes for their support, guidance and suggestions along the path of this research. They were always available for discussions providing interesting ideas for investigation. Also, my gratitude goes to Dr Munir Ahmad, Dr Anisha Mukherjee and Dr Kaushal Choonee for teaching me the intricate microfabrication process and for providing advise to subtle fabrication issues. Their help, particularly in the beginning, helped me lay the foundations. Moreover, I would like to thank Dr Yun Zhou for her advice at the beginning of my research and William Otter for his help with the waveguide measurements. A big thanks goes to the staff from level 1, May Tang and Victor Boddy, who were always more than happy to provide instant access to any equipment needed. Phil Jones from the mechanical workshop, is also gratefully acknowledged. His help and suggestions with the devices used for the assembly of the prototypes and in the experimental setup made things much simpler. Also, my appreciation goes to everyone in the Optical and Semiconductor Devices group for creating a joyful atmosphere to work.

My deepest thanks and gratitude goes to my beloved parents and brother who supported me in every possible way and have been there for me not just these last four years, but all through my life. Finally, I would like to thank Stergios, first because this work would not have been the same without his invaluable feedback but most importantly for his endless love and encouragement which made this difficult journey easier.

Abstract

The development of tunable waveguide components for systems that require multifunctionality, at terahertz frequencies is investigated using the photoconductivity effect. Specifically, by the photo-generation of free charged carriers highly conducting plasma regions are created and by changing the light pattern in real time, various tunable components can be implemented.

The aim of this thesis is to present a novel reconfigurable optically-controlled terahertz waveguide switch as an illustrative example of this approach, addressing the challenges and limitations involved in simulation, implementation and measurement of such devices and is organised in the following chapters.

Chapter 1 gives the background theory of the fundamental principles of optoelectronic devices and presents a literature survey of existing optically-controlled structures across a wide frequency spectrum.

Chapter 2 presents a comparative study of four commercial software packages with the aim to show that it is not always straightforward to select the most appropriate boundary conditions and define a materials parameter within a software when terahertz structures are modelled. A study of various modelling approaches using commercially-available software packages has been undertaken; a number of approaches have been identified and the most appropriate solutions are indicated.

Chapter 3 presents a microwave plasma switch as a proof-of-concept scaled demonstrator. In this preliminary experiment a metal pipe rectangular waveguide (similar to WR-650 standard) has been implemented, which can be reconfigured as an ON-OFF switch using a plasma column formed by commercially available discharge tubes. This provides a good starting point for more sophisticated devices as presented in the following chapters.

In Chapter 4 a novel optically-controlled waveguide plasma switch for terahertz applications is presented. The switch is excited by a continuous wave (CW) laser source and the photoconductivity profile, due to the laser illumination, is described in detail. The performance of the switch is studied by means of full-wave numerical simulations and various parametric studies are undertaken to provide physical insight in the device performance. The thermal characteristics of the device are also investigated.

Chapter 5 gives in detail the processing steps for the microfabrication of various prototypes with the assembly of the prototypes being also discussed. The waveguide experimental setup is described in detail and the measurement results obtained are presented. In particular, emphasis has been given on the alignment of the devices with the Vector Network Analyser waveguide heads.

Finally, Chapter 6 gives a summary of the work presented in this thesis and potentially new research directions are indicated as future work.

List of Figures

List of Tables

List of Abbreviations

BS	Beam Splitter
CST	Computer Simulation Technology
CW	Continuous Wave
CWB	Conducting Wall Boundary
C_4F_8	octafluorocyclobutane
DRIE	Deep Reactive Ion Etching
EMPro	Electromagnetic Professional
FCB	Finite Conductivity Boundary
FDTD	Finite-Difference Time-Domain
FEM	Finite-Element Method
FIT	Finite-Integration Technique
GaAs	Gallium Arsenide
HFSS	High Frequency Stucture Simulator
HMDS	Hexamethyldisilazane
HRS	High Resistivity Silicon
IB	Impedance Boundary
IPA	Isopropyl Alcohol
IR	Infrared
KDP	Potassium Dihydrogen Phosphate
LED	Light-Emitting Diode
LIB	Layered Impedance Boundary
LSE	Longitudinal Section Electric
LSM	Longitudinal Section Magnetic
MPRWG	Metal-Pipe Rectangular Waveguide
PEC	Perfect Electric Conductor
PMC	Perfect Magnetic Conductor
PPS	Periodically Photo-excited Section
PPWG	Parallel Plate Waveguide
SEM	Scanning Electron Microscope
SF_6	Sulfur Hexafluoride
Si	Silicon
SOLT	Short/Offset-short/Line/Thru
SPP	Surface Plasmon Polariton
SPS	Signal Pulse Selectror
SR	Surface Resistance
STS-ICP	Surface Technology Systems-Inductively Coupled Plasma
TE	Transverse Electric
TEM	Transverse Electric and Magnetic
THz	Terahertz
TM	Transverse Magnetic
UV	Ultraviolet
VBScript	Visual Basic Script
VNA	Vector Network Analyzer
WR	Waveguide Rectangular

Chapter 1

Introduction

Metal Pipe Rectangular Waveguides (MPRWG) are essential components in many high-performance systems operating across a wide frequency spectrum; from microwaves to terahertz waves. First introduced well over a century ago, the behaviour of the rectangular waveguides is well understood, while their simple structure makes their fabrication relatively easy. Recently, with the commercial development of Vector Network Analyser (VNA) systems operating up to 1.1 THz they have attracted renewed interest. However, a current limitation at this frequency range is the lack of real-time tunable rectangular waveguide components.

An efficient way to deal with the above problem is the use of the photoconductivity effect. This optoelectronic approach has already been used for optically-controlled microwave and millimetre-wave devices (i.e. sub-picosecond switches) because it provides several advantages such as fast response time, immunity to electromagnetic interference (EMI) and the possibility for monolithic integration with other components. This approach can be implemented with the use of short laser pulses or continuous wave illumination. In the latter case, the carrier diffusion and surface recombination processes have a significant effect on the induced photoconductivity, resulting in higher induced carrier concentration and thus higher photoconductivity. Also, longer plasma penetration depth is obtained and hence bulk plasma regions can be generated within a semiconductor material. Thus, with the use of high resistivity semiconductor materials with high carrier lifetimes (e.g. high resistivity silicon) high photoconductivity can be achieved.

The aim of the work presented in this thesis is to use the concept of the photoconductivity effect for the development of a terahertz optically-controlled waveguide switch as an illustrative example of this approach. First, a very exhaustive study of the full-wave simulation approaches is undertaken in order to investigate the weaknesses and limitations with commercially-available solvers. Moreover, at these high frequencies, manufacturing tolerances affect the device performance significantly; therefore, the limitations posed both by the current fabrication methods and the device requirements have to be taken into account. In addition, particular emphasis needs to be given on potential alignment issues. A further issue of the thermal challenges posed by the laser illumination need to be considered. Thus, the thermal characteristics of such devices need to be studied in conjunction with the illuminating power. Hence, a trade-off is required for improved device performance.

In this chapter a discussion of the fundamental principles of the laser excitation effects in a semiconductor material is presented in order to obtain a better understanding of the

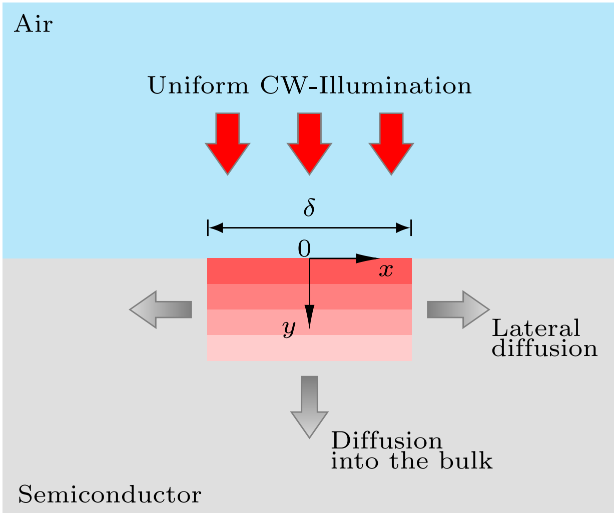

Figure 1.1: Cross-sectional illustration of a very long uniform semiconductor slab, uniformly illuminated by a CW optical source over a region of length δ at its center.

basics of optoelectronic devices. The aim of this section is to present a brief introduction of the various topics that will be used in the following chapters. A literature survey of existing optically-controlled structures across a wide frequency spectrum is also presented.

1.1 Background Theory

The operation of optoelectronic devices is based on the photo-generation of free electron-hole pairs within an illuminated semiconductor region when the photon energy is similar or larger than the semiconductor band-gap energy [1, 2]. Due to the laser excitation, the semiconductor is not in the equilibrium state, and hence effects on the electrons and holes motion, such as drift, diffusion and recombination occur. Drift of photo-excited carriers is the result of an electric field, diffusion is related to the random thermal motion due to the non-uniform spatial concentration, and recombination occurs so that both carriers return to equilibrium concentrations. Some of the general terms used to describe the above processes are briefly explained in the next sections where the distribution of photoconductivity within an illuminated semiconductor is studied. In specific, a simplified analysis will be used where the two dimensional distribution $\Delta\sigma(x, y)$ is approximated by the product of the horizontal and vertical profiles $\sigma(x)$ and $\sigma(y)$ with each of them calculated assuming an excitation model with perfect one-dimensional carrier flow [3].

1.1.1 Horizontal Distribution of Photoconductivity

Generally, in a semiconductor the total charge density is given by [1, 2]

$$\rho = e(N_{\mathrm{D}} - N_{\mathrm{A}} + p_0 - n_0) \tag{1.1}$$

where N_{D} and N_{A} is the charge of the excess donors and acceptors respectively in an extrinsic semiconductor and p_0, n_0 are the bulk concentrations of the free holes and electron carriers respectively. In a uniformly doped material at thermal equilibrium $\rho = 0$. In the more specific case of an intrinsic semiconductor, it can be assumed that $N_{\mathrm{D}} = N_{\mathrm{A}} = 0$ and $n_0 \simeq p_0$. If an intrinsic semiconductor slab is illuminated uniformly by a continuous-wave light over a region of length δ, producing hole-electron pairs at a rate g pairs/m^{3}s the charge density is

$$\rho = e[(p_0 + p') - (n_0 + n')] \tag{1.2}$$

with n' and p' being the photo-induced carrier densities. Due to the laser illumination (Fig. 1.1), hole and electron diffusion currents will flow in opposite directions, while hole and electron drift currents will flow in the same direction. To this end, it is assumed that the resulting effect of the non-equilibrium processes taking place is a superposition of the individual effects and the results are linearly dependent on their causes, with no thermo-electric effects occurring. Thus, the current densities of electrons and holes produced, are given by the relations [1, 2]

$$J_{\mathrm{h}} = e\mu_{\mathrm{h}} pE - eD_{\mathrm{h}} \nabla p \tag{1.3}$$

$$J_{\mathrm{e}} = e\mu_{\mathrm{e}} nE + eD_{\mathrm{e}} \nabla n \tag{1.4}$$

$$J = J_{\mathrm{e}} + J_{\mathrm{h}} \tag{1.5}$$

where $n = n_0 + n'$, $p = p_0 + p'$ is the total electron and hole density, μ_{e}, μ_{h} is the electron and hole mobility and $D_{\mathrm{e}} = \mu_{\mathrm{e}} \frac{k_{\mathrm{B}}T}{e}$, $D_{\mathrm{h}} = \mu_{\mathrm{h}} \frac{k_{\mathrm{B}}T}{e}$ the electron and hole diffusion coefficients respectively (with k_{B} being the Boltzmann constant and T the absolute temperature). Now, in a semiconductor substrate with uniform bulk carrier density, the equilibrium concentrations n_0 and p_0 are not functions of position. Thus, with the assumption that there is no carrier flow in the y-direction, the above equations for a one-dimensional problem (in x-axis direction) can be written as

$$J_{\mathrm{h}} = e\mu_{\mathrm{h}} pE - eD_{\mathrm{h}} \frac{dp'}{dx} \tag{1.6}$$

$$J_{\mathrm{e}} = e\mu_{\mathrm{e}} nE + eD_{\mathrm{e}} \frac{dn'}{dx} \tag{1.7}$$

With the condition that there is no external bias applied to the semiconductor slab $J = 0$. To this end, if it is assumed that n' and p' differ very little at every point, there is expected to be little difference between dp'/dx and dn'/dx and hence, the diffusion terms $D_{\mathrm{e}}(dn'/dx)$ and $D_{\mathrm{h}}(dp'/dx)$ of (1.6) and (1.7) are of comparable magnitudes. Also, with $n \simeq p$, and with μ_{e} and μ_{p} being comparable, the drift and diffusion terms for both electrons and holes may be comparable too.

Apart from drift and diffusion phenomena taking place due to the photoexcitation of a semiconductor, recombination of the excess free carriers also occurs so that the system can return back to the equilibrium state. In specific, a semiconductor region with thickness Δx and cross section A is assumed, where carriers (e.g. holes) flow into the region (across the x plane) with an incoming current density $J_{\mathrm{h}}(x)$ and at the same time flow out (across the $x+\Delta x$ plane) with an outgoing current density $J_{\mathrm{h}}(x + \Delta x)$, as shown in Fig. 1.2. Due to optical excitation, free carriers (i.e. hole-electron pairs) are generated inside the semiconductor with a generation rate g while the excess carriers recombine inside the semiconductor with a recombination rate [1] $r_{\mathrm{h}} = \frac{p'}{\tau_{\mathrm{h}}}$ and $r_{\mathrm{e}} = \frac{n'}{\tau_{\mathrm{e}}}$, where p' and n' is the excess holes and electrons density respectively (i.e. $p' = p - p_0$, $n' = n - n_0$) and τ_{h}, τ_{e} is the holes and electrons lifetime

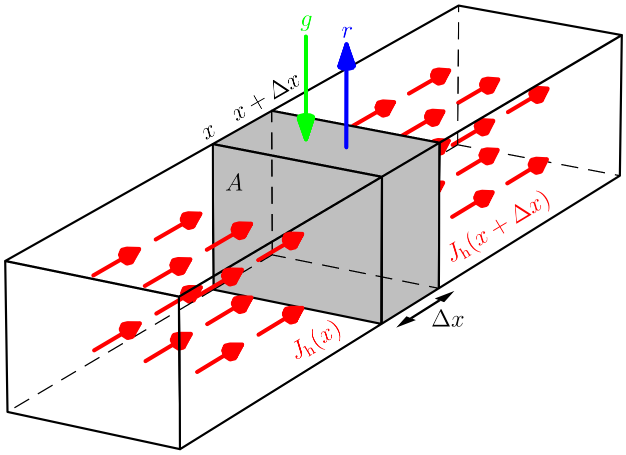

Figure 1.2: Schematic illustration of the continuity equation.

respectively. As a result of the above processes, the increase in the holes density per unit time $\partial p/\partial t$ is equal to [1, 2]

$$\frac{\partial p}{\partial t} = \frac{1}{e}\frac{J_{\mathrm{h}}(x) - J_{\mathrm{h}}(x+\Delta x)}{\Delta x} + g - \frac{p'}{\tau_{\mathrm{h}}} \tag{1.8}$$

With $\Delta x \to 0$ and assuming that the bulk carrier densities n_0 and p_0 are independent of time, the current change can be written in the form [1]

$$\frac{\partial p'}{\partial t} = -\frac{1}{e}\frac{\partial J_{\mathrm{h}}}{\partial x} + g - \frac{p'}{\tau_{\mathrm{h}}} \tag{1.9}$$

Thus, the continuity equations for both holes and electrons are

$$\frac{\partial p'}{\partial t} = -\frac{1}{e}\frac{\partial J_{\mathrm{h}}}{\partial x} + g - \frac{p'}{\tau_{\mathrm{h}}} \tag{1.10}$$

$$\frac{\partial n'}{\partial t} = \frac{1}{e}\frac{\partial J_{\mathrm{e}}}{\partial x} + g - \frac{n'}{\tau_{\mathrm{e}}} \tag{1.11}$$

Using (1.6) and (1.7) and the fact that $\partial p'/\partial t = \partial n'/\partial t = 0$ in the steady state, the continuity equations (1.10) and (1.11) yield

$$D_{\mathrm{h}}\frac{d^2 p'}{dx^2} - \mu_{\mathrm{h}}\frac{d(pE)}{dx} + g - \frac{p'}{\tau_{\mathrm{h}}} = 0 \tag{1.12}$$

$$D_{\mathrm{e}}\frac{d^2 n'}{dx^2} + \mu_{\mathrm{e}}\frac{d(nE)}{dx} + g - \frac{n'}{\tau_{\mathrm{e}}} = 0 \tag{1.13}$$

Now, multiplying (1.12) with $\mu_{\mathrm{e}} n$ and (1.13) with $\mu_{\mathrm{h}} p$ and adding the equations one gets

$$(\mu_{\mathrm{e}} n D_{\mathrm{h}} + \mu_{\mathrm{h}} p D_{\mathrm{e}})\frac{d^2 p'}{dx^2} + (\mu_{\mathrm{e}}\mu_{\mathrm{h}})(p-n)E\frac{dp'}{dx} + (\mu_{\mathrm{e}} n + \mu_{\mathrm{h}} p)\left[g - \left(\frac{p'}{\tau_{\mathrm{h}}} + \frac{n'}{\tau_{\mathrm{e}}}\right)\right] = 0 \tag{1.14}$$

when $n' \simeq p'$ and taking into account that n_0 and p_0 are not spatially dependent. After dividing (1.14) by $\mu_{\mathrm{e}} n + \mu_{\mathrm{h}} p$, it can be written as

$$D_a\frac{d^2 p'}{dx^2} + \mu_a E\frac{dp'}{dx} + g - \left(\frac{p'}{\tau_{\mathrm{h}}} + \frac{n'}{\tau_{\mathrm{e}}}\right) = 0 \tag{1.15}$$

where $D_a = \dfrac{\mu_e n D_h + \mu_h p D_e}{\mu_e n + \mu_h p}$ is the ambipolar diffusion coefficient and $\mu_a = \dfrac{\mu_e \mu_h (p - n)}{\mu_e n + \mu_h p}$ is the ambipolar mobility. Equation (1.15) is the ambipolar transport equation describing the behaviour of excess carriers (both electrons and holes). Using the relation $\dfrac{\mu_e}{D_e} = \dfrac{\mu_h}{D_h} = \dfrac{e}{k_B T}$ the ambipolar diffusion coefficient becomes $D_a = \dfrac{D_e D_h (n + p)}{n D_e + p D_h}$, which for an intrinsic semiconductor (i.e. $n_0 = p_0$) reduces to $D_a = \dfrac{2 D_e D_h}{D_e + D_h}$. For an intrinsic semiconductor with $n_0 = p_0$ and the assumption that $n' \simeq p'$ the second term in (1.15) can be neglected. Moreover, in the region $x > \delta/2$ where there is no light, $g = 0$, (1.15) reduces to

$$\frac{d^2 p'}{dx^2} - \frac{p'}{D_a \tau_a} = 0, \quad \text{for } x > \delta/2 \tag{1.16}$$

where $\tau_a = \dfrac{\tau_e \tau_h}{\tau_e + \tau_h}$ is the ambipolar lifetime. The solution of (1.16) should be equal to zero at $x \to \infty$ since the light source must vanish in great distance, so the solution is

$$p' = B e^{-x/L_a}, \quad \text{for } x > \delta/2 \tag{1.17}$$

where $L_a = \sqrt{D_a \tau_a}$ is the ambipolar diffusion length and B is a constant. In the region where the light generates carrier pairs ($0 < x < \delta/2$) at a constant rate g, from (1.15)

$$\frac{d^2 p'}{dx^2} - \frac{p'}{L_a^2} = -\frac{g}{D_a}, \quad \text{for } 0 < x < \delta/2 \tag{1.18}$$

The solution of this equation is

$$p' = C e^{-x/L_a} + D e^{x/L_a} + g\tau_a, \quad \text{for } 0 < x < \delta/2 \tag{1.19}$$

The current should vanish at $x = 0$ because otherwise, due to symmetry, a current source at $x = 0$ would be implied. Thus, the continuity equation would require a finite generation or recombination rate from a zero volume at $x = 0$ (Fig. 1.1), which can't be true. With this observation it can be calculated that [1]

$$C = D \tag{1.20}$$

Similarly, from the current continuity at the plane $x = \delta/2$ follows that [1]

$$B = C(1 - e^{\delta/L_a}) \tag{1.21}$$

Moreover, at the plane $x = \delta/2$ the total hole concentration $p = p_0 + p'$ must also be continuous and therefore with p_0 being constant, the hole concentration given by (1.17) and (1.19) must agree. Thus, from (1.17), (1.19), (1.20) and (1.21) the following expression is obtained at $x = \delta/2$

$$C = -\frac{g\tau_a}{2} e^{-\delta/2L_a} \tag{1.22}$$

Therefore, the equation for the hole concentration is [1, 4]

$$p'(x) = \begin{cases} g\tau_a \left(1 - e^{-\delta/2L_a} \cosh \dfrac{x}{L_a}\right), & \text{for } 0 \leqslant x < \delta/2 \quad (1.23a) \\[2ex] g\tau_a \left(\sinh \dfrac{\delta}{2L_a}\right) e^{-x/L_a}, & \text{for } x \geqslant \delta/2 \quad (1.23b) \end{cases}$$

Thus, when there is no carrier flow in the y-direction and with the photoconductivity of a semiconductor given by the expression $\sigma = e(n'\mu_{\rm e} + p'\mu_{\rm h}) \xRightarrow{p' \simeq n'} \sigma = ep'(\mu_{\rm h} + \mu_{\rm e})$, the horizontal distribution of the photoconductivity can be calculated using (1.23) as [1–4]:

$$\sigma(x) = \begin{cases} \sigma_m \left[1 - e^{-\frac{\delta}{2L_a}} \cosh\left(\frac{x}{L_a}\right)\right], & \text{for } 0 \leqslant x \leqslant \frac{\delta}{2} \quad (1.24\text{a}) \\ \sigma_m \left[e^{-\frac{x}{L_a}} \sinh\left(\frac{\delta}{2L_a}\right)\right], & \text{for } \frac{\delta}{2} \leqslant x \leqslant \infty \quad (1.24\text{b}) \end{cases}$$

where σ_m is the maximum photoconductivity at $x = 0$ and $L_a = \sqrt{\frac{2\tau_a\mu_{\rm e}\mu_{\rm h}}{\mu_{\rm e} + \mu_{\rm h}} \frac{k_{\rm B}T}{e}}$ being the ambipolar diffusion length corresponding to the ambipolar diffusion coefficient $D_a = 2D_{\rm e}D_{\rm h}/(D_{\rm e} + D_{\rm h})$ as explained above.

1.1.2 Vertical Distribution of Photoconductivity

In order to calculate the carrier density distribution in the y-direction (Fig. 1.1) a negligible carrier flow in the x-direction is assumed, with all other assumptions mentioned above still holding true. From the continuity equation (with trapping effects being neglected) [2]:

$$D_a \frac{d^2p'}{dy^2} - \frac{p'}{\tau_a} = g(y) \tag{1.25}$$

Due to the large value of the high resistivity silicon absorption coefficient and with a thickness of a few hundreds of microns it can be assumed that $w \gg 1/a$ and $w \gg L_a$ where w is the thickness of the wafer and a is the absorption coefficient, the solution of (1.25) is of the form [2]:

$$p' = Fe^{-y/L_a} - \frac{\tau_a g(y)}{(L_a^2 a^2 - 1)} \tag{1.26}$$

where F is a constant which can be determined from the boundary condition at the surface of the semiconductor ($y = 0$)

$$D_a \frac{\partial p'}{\partial y}\bigg|_{y=0} = v_{\rm s} p' \tag{1.27}$$

where $v_{\rm s}$ is the surface recombination velocity. The carrier generation rate is given from the expression [2]

$$g(y) = aQ(y) = a(1 - R_\lambda)Qe^{-ay} = aQ_0e^{-ay} \tag{1.28}$$

where R_λ is the reflectivity and Q_0 the photon flux penetrating the surface into the interior of the semiconductor given by the expression [2]

$$Q_0 = Q(1 - R_\lambda) \tag{1.29}$$

The photon flux incident on the surface Q can be calculated from the expression

$$Q = \frac{PS_\lambda}{E_{\rm ph}A} = \frac{PS_\lambda}{(\frac{hc}{\lambda})A} = \frac{PS_\lambda \lambda}{hcA} \quad [\text{photons/cm}^2\text{sec}] \tag{1.30}$$

where P is the illumination power incident on the surface of the semiconductor, S_λ is the photosensitivity of the semiconductor at the illumination wavelength, $E_{\rm ph}$ is the photon energy and A is the illumination area. Substituting (1.26) and (1.28) into (1.27) the constant F is calculated as

$$F = \frac{L_a Q_0 a(\tau_a v_s + aL_a^2)}{(a^2 L_a^2 - 1)(D_a + v_s L_a)} \tag{1.31}$$

Inserting the expression for F into (1.26) the vertical distribution of the excess carrier density inside the semiconductor is given by [2]

$$p' = \frac{Q_0 a}{(1 - a^2 L_a^2)} \left\{ \tau_a e^{-ay} - \left[\frac{L_a}{D_a + v_s L_a} (\tau_a v_s + aL_a^2) e^{-y/L_a} \right] \right\} \tag{1.32}$$

Using (1.32) and the expression for the photoconductivity $\sigma = e(p'\mu_h + n'\mu_e) \overset{p' \simeq n'}{\Longrightarrow} \sigma = ep'(\mu_h + \mu_e)$ one gets [2, 3]

$$\sigma(y) = e(\mu_h + \mu_e) \frac{Q_0 a \tau_a}{(1 - a^2 L_a^2)} \left\{ e^{-ay} - \left[\frac{L_a}{\tau(D_a + v_s L_a)} (\tau_a v_s + aL_a^2) e^{-y/L_a} \right] \right\} \tag{1.33}$$

From (1.29), (1.30) and (1.33) the expression for the photoconductivity is

$$\sigma(y) = \frac{\sigma_0}{(1 - a^2 L_a^2)} \left\{ e^{-ay} - \frac{\tau_a v_s + aL_a^2}{\tau_a (L_a + v_s \tau_a)} e^{-y/L_a} \right\} \tag{1.34}$$

where $\sigma_0 = \dfrac{q}{hc}(\mu_e + \mu_h)(1 - R_\lambda) a\lambda \dfrac{PS_\lambda \tau_a}{A}$.

From the above, the photoconductivity distribution inside the semiconductor can be approximately given by $\sigma(x, y) = \dfrac{\sigma(x)\sigma(y)}{\sigma_0}$ and thus the photoconductivity σ_m can be calculated using as [3]

$$\sigma_m = \frac{\sigma_0}{(1 + aL_a)} \left[\frac{1}{aL_a} \left(\frac{\tau_a v_s + aL_a^2}{\tau_a v_s + L_a} \right) \right]^{-aL_a/(1 - aL_a)} \tag{1.35}$$

In the above discussion the expressions for the induced photoconductivity inside an intrinsic semiconductor region at continuous-wave laser excitation are given. Although, a more accurate analysis solving the 2D continuity equations for the excess carrier density can be obtained, with this more simplified model a good approximation of the photoconductivity profile can be obtained.

1.2 Optically-Controlled Structures

1.2.1 Microwave and Millimeter-Wave Devices

The use of photo-induced plasma in semiconductors for optically-controlled structures has been exploited over the last decades as a means of developing tunable integrated devices (i.e. subpicosecond switches) at microwave, millimeter-wave and optical frequencies. This approach uses the photoconductivity effect to control the operation of such devices either with picosecond optical pulses [4–9] or continuous wave (CW) and quasi-CW illumination [10–12]. For the first time, in 1972, Jayaman and Lee investigated the photoconductivity effect in GaAs crystals as a result of picosecond laser illumination [5]. After this work Auston presented a picosecond optoelectronic switch for DC signals [6] which was further extended for microwave signals by Johnson and Auston in 1975 [7]. The switch performance is controlled by short optical pulses focused onto a microstrip gap; in this device however different

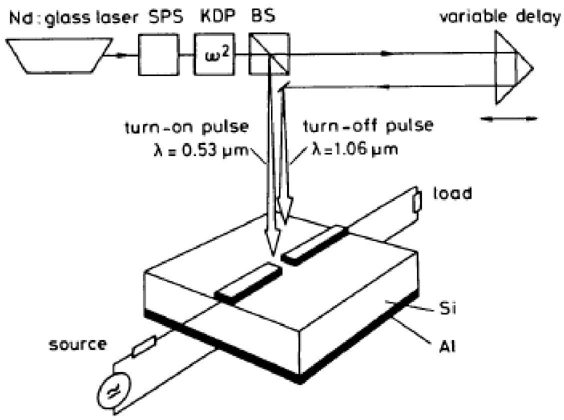

Figure 1.3: Microwave optoelectronic switch the operation of which is produced by two picosecond optical pulses, each one corresponding to a different absorption depth (SPS: signal pulse selector, KDP: crystal for second harmonic generation, BS: beam splitter) [7]

wavelength pulses are used for the two states of the switch. The infrared pulse is generated by extracting a single pulse from a train produced by a mode-locked Nd:glass laser. The green pulse is produced by second harmonic generation in a potassium dihydrogen phosphate (KDP) crystal. The pulses are then seperated in a beamsplitter and the infrared pulse is delayed relative to the green pulse. The microwave input signal is transmitted when the substrate is illuminated by the short green laser pulse, which produces a thin layer of photoconductivity near the surface. On the other hand, the signal is reflected when illuminated by the infrared pulse and hence, a region with bulk high photoconductivity across the substrate is created (Fig. 1.3).

In contrast to previous research on single-gap structures, where both turn-on and turn-off processes are obtained at the same region of the substrate, in 1976 Platte, based on Auston's method, reported a combined gap-shunt microstrip structure fabricated on a silicon substrate for high-speed switching and gating [8]. In this device, the turn-on and turn-off processes occur in different regions in the substrate, as shown in Fig. 1.4, by picosecond optical pulses of the same wavelength. When a turn-on pulse is focused on the microstrip gap the absorbed radiation results in a high photoconductivity region within the excited semiconductor and hence transmission occurs through the microstrip line. A delayed turn-off pulse is focused on the semiconductor shunt structure. Thus, the microstrip line is short-circuited preventing further transmission. With this technique, the turn-off time is independent of the carrier recombination time. Also, by using two optical pulses of the same wavelength a more simplified controlling optical technique is obtained.

In comparison with the above mentioned optically-controlled structures, where top-side excitation is employed, there has been proposed an alternative method via substrate-edge excitation [13, 14]. In this case, an open-ended GaAs microstrip section is illuminated by short laser pulses which are perpendicular to the microstrip cross section, as shown in Fig. 1.5. With no optical illumination, the input signal propagates along the microstrip line without significant attenuation and is reflected at the open end of the microstrip. It then passes through the microstrip section for the second time and reenters the circulator. When the device is optically excited with short laser pulses an exponentially decaying photoconductivity is generated between the strip and the ground plane, with the carrier diffusion being

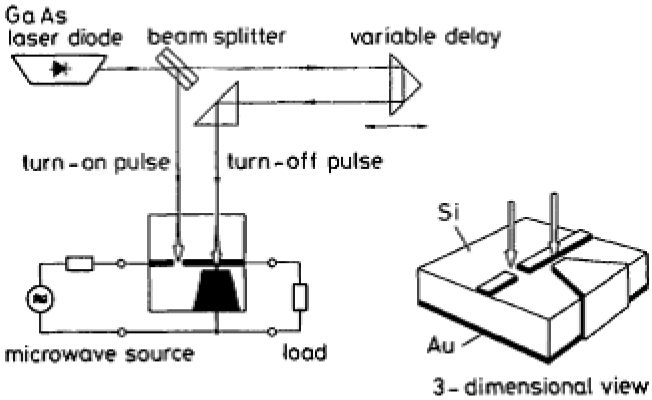

Figure 1.4: Combined gap-shunt microstrip structure [8]

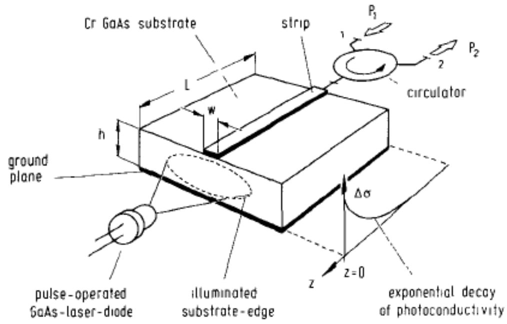

Figure 1.5: Substrate-edge excited optoelectronic microwave switch. [13].

neglected. Thus, the microwave signal is fully absorbed within this plasma region, which operates like a lossy tapered transmission line, causing zero level at port 2 of the circulator. From the above it is clear that the ON and OFF states of this device are inverted compared to top-side illuminated switches. Also, this switch requires lower pulse intensity returning automatically to its ON state due to the fast recombination time of the GaAs substrate. However, the need for a circulator or for the signal to be absorbed in the tapered plasma region could result in some variation in performance with frequency.

Moreover, with the design of optoelectronic switches having received much attention, the development of systems for measurements on high-speed devices (i.e. switching time of picosecond switching devices) was necessary. With the principle of operation based on Auston's work, a 10ps optoelectronic sampling system has been presented in [15]. An extension of this sampling system was presented by Everard *et al.* where the utilisation of already available picosecond optoelectronic switches for the development of three practical sampling systems has been presented [16]. In the first system two optical pulses with 10 ps duration and different wavelengths are used. In the final system a very low power laser source was used creating a 300 ps sampling system providing a much wider dynamic range than a conventional one.

While, there has been extensive research on microwave optoelectronic devices using picosecond laser illumination, mainly due to their picosecond precision, high-speed control and simplicity of operation, an alternative approach, of CW illumination has been investigated [3, 17–19]. As an example, a microwave Bragg reflecting filter where the grating

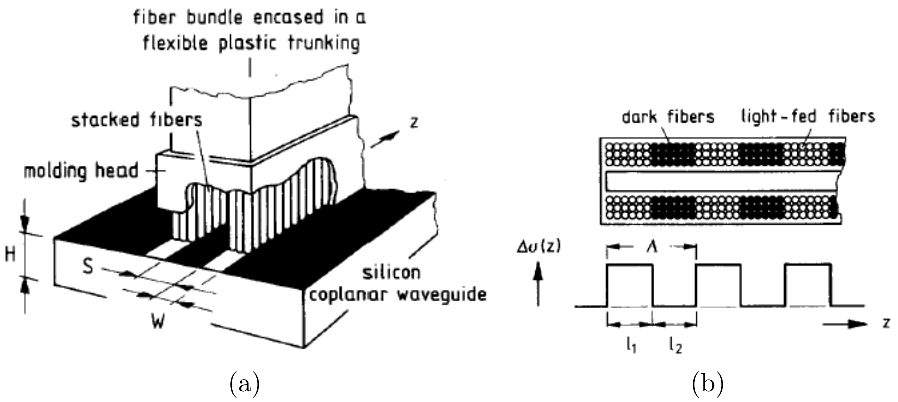

Figure 1.6: (a) Microwave Bragg filter illuminated by a fiber bundle array (b) Cross section of the molding head and the corresponding photoconductivity profile when the carrier diffusion is neglected [17].

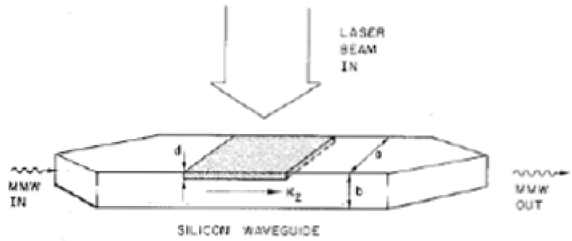

Figure 1.7: Millimeter-wave optically controlled phase shifter [20].

elements are produced by the periodic illumination of a silicon coplanar waveguide has been studied [17]. In this device an LED-fed fiber array generates photo-induced carriers inside the semiconductor with a periodic distribution and thus by changing the light pattern the operating center frequency of the filter is adjusted, as shown in Fig. 1.6

With microwave optoelectronic devices being the starting point and with increasing commercial interest in the frequency range from 30 GHz to 300 GHz further research was conducted on the optical control of millimetre-wave and sub-millimetre wave devices for a variety of applications such as phase shifters, frequency modulators and filters [20–25]. This new approach was applied for the first time by Lee, Mak and Defonzo in 1980 [20]. A millimeter-wave optically controlled phase shifter was proposed, consisting of a rectangular dielectric waveguide with tapered ends, minimizing the reflections as shown in Fig. 1.7. When the device is optically excited by a laser pulse and the plasma density exceeds the value at which the plasma frequency equals the frequency of the millimeter wave, an interaction between the plasma and the propagating wave occurs. A further increase in the plasma density results in a decrease in the skin depth; when the skin depth is equal to the thickness of the plasma layer, the illuminated region can be regarded as highly conductive and thus the dielectric waveguide becomes an image line. The imaging effect causes the phase shift of the propagating wave. As an extension to this method ultra-fast switching and gating has been demonstrated.

Moreover, an extensive study of optically induced plasma interaction with millimeter wave propagation in a slot line has been presented [21]. The proposed slot line configuration

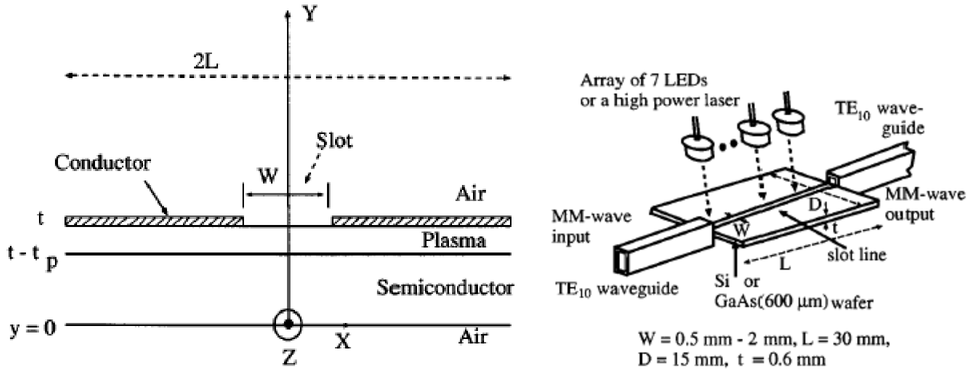

Figure 1.8: (a) Optically controlled slot line with a photo-induced plasma layer (b) Experimental demonstrator [21].

can also be used for the optical control of millimeter-wave attenuators and amplitude shift-keying modulators over a wide frequency range using weak optical illumination. Illumination from an array of seven LEDs at 870 nm was applied to induce optical plasma in the silicon substrate in the slot region (Fig. 1.8). Thus, an attenuation of more than 20 dB can be achieved with total optical power of 68 mW.

Apart from dielectric and coplanar waveguides which have been widely used for the implementation of optically controlled millimeter-wave structures, alternative designs based on rectangular metallic waveguides have been explored but only in preliminary stage. For example, a millimeter-wave phase shifter (Fig. 1.9.) which consists of a W-band rectangular metallic waveguide inhomogeneously filled with a rectangular semiconductor slab has been presented [22]. The semiconductor is optically excited by 100 nsec laser pulses through an aperture at the sidewall of the waveguide. A measured phase shift of 35^o with 14 dB of attenuation is obtained at 94 GHz. However, due to the large thickness of the silicon insert (985 µm) multimode propagation occurs.

Similarly, in a more recent work, a design of a milimeter-wave waveguide switch has been proposed [23]. The design presented, consists of a WR-10 metallic waveguide with a low conductivity rectangular silicon slab inserted across the waveguide cross section, as shown in Fig. 1.10. The silicon slab is illuminated with sub-nanosecond laser pulses at 1064 nm via an optical fiber through a sidewall slot. From the measured results presented so far, the operation frequency is at 94 GHz demonstrating an ON-OFF ratio of 30 dB over a narrow bandwidth of 1 GHz. However, in contrast with this work, by illuminating the silicon slab through the top and bottom walls (instead of the sidewalls), the interaction between the light and the input millimeter-wave signal is expected to be more significant and thus a higher ON-OFF ratio could be achieved.

1.2.2 Terahertz Optically-Controlled Components

With great commercial and research interest in the terahertz frequency spectrum increasing research emphasis is placed on manipulation of propagating THz waves, with high demand on components such as opto-THz switches, modulators and filters [26–33]. The technique of using the photoconductivity effect in high-resistivity semiconductors, which has been

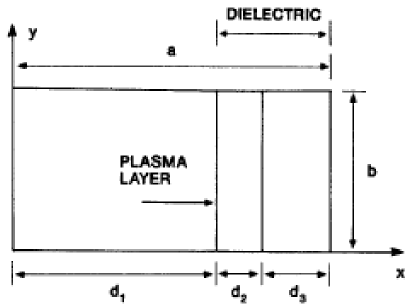

Figure 1.9: Configuration of a W-band millimeter-wave phase shifter with dimensions $d_1 = 1555\ \mu$m and $d_2 + d_3 = 985\ \mu$m [22].

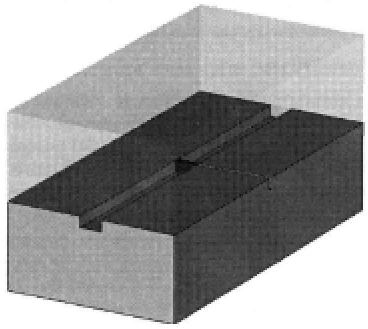

Figure 1.10: Millimeter-wave (i.e. WR-10) waveguide switch including a sidewall slot for laser excitation. [23].

extensively used for the development of tunable components at microwave and millimeter-wave frequencies, shows a big potential for THz applications as well. With optical excitation, free carriers are generated and thus strong interaction with THz waves is obtained resulting in interesting phenomena that can be used for THz modulation and switching.

In 2007, a parallel-plate waveguide (PPWG) THz modulator was demonstrated [26]. In this design the metal plates have been replaced with transparent conductive oxide films allowing the high resistivity silicon slab inside the waveguide to be optically excited by a CW laser source as shown in Fig. 1.11. With a laser power of 240 mW a 70% reduction of the peak electric field is obtained.

Another approach, is the use of photonic crystal structures for the development of opto-THz switches and modulators. A photonic crystal modulator for THz frequencies was demonstrated by L. Fekete *et al.* [27], consisting a one-dimensional photonic crystal with a GaAs wafer inserted in the middle as a defect layer. Illumination of the GaAs surface with 810 nm laser pulses results in ultrafast (approximately 110 ps) modulation of the THz incoming wave, obtaining a modulation of 50%.

Moreover, the control of a THz transmission through periodic arrays of subwavelength holes in thin metal films on a silicon substrate has been investigated [28]. As in the previous device, a photoexcitation of short laser pulses (in this case 150 fs) is used to obtain ultrafast switching with low visible light intensities.

With all the above advantages provided by the photoexcitation of semiconductors as a means of controlling the propagation of THz waves, this concept has also been applied to the

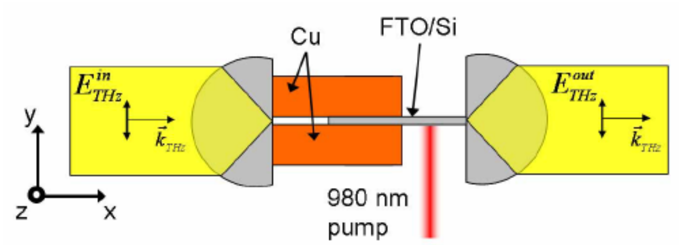

Figure 1.11: Sketch of the optical modulation setup. The incoming THz beam is coupled into the oxide-coated silicon PPWG through an air-filled copper PPWG. The optical excitation is provided by a 980 nm CW laser [26].

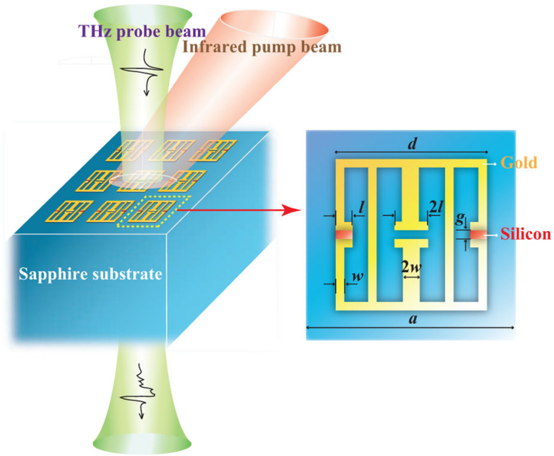

Figure 1.12: Sketch of a tunable metamaterial device. Left: Experimental configuration for the measurement of THz transmission. Right: unit cell of the structure [29].

field of metamaterials. Specifically, by incorporating photoconductive semiconductors, as elements of metamaterial resonators, the working frequency of the metamaterial resonator can be tuned through photoexcited carrier generation. As an example, the design of an optically implemented broadband blueshift switch with a tuning range of 26% has been presented [29]. The device is based on electric-field-coupled inductor capacitor (ELC) resonators with photoconductive silicon put within two side gaps of the metallic ELC resonator in each unit cell (Fig. 1.12). Due to photoexcitation, the silicon becomes conductive and the structure is forced to switch from mode 1 (lower frequency) to mode 2 (higher frequency).

Also, recently a novel substrate integrated waveguide technology was proposed. The RETINA (Reconfigurable Terahertz Integrated Architecture) concept is based on the photo-induced plasma that is extended from the top surface downwards towards the bottom surface of the semiconductor [30, 31]. As an example, instead of a traditional rectangular waveguide with metal sidewalls (i.e. WR-03), a RETINA structure can be used, in which the metal sidewalls are replaced by photo-induced conducting sidewalls within a high-resistivity silicon substrate (Fig. 1.13). By changing the light pattern on the surface of the substrate in real time various tunable components can be produced.

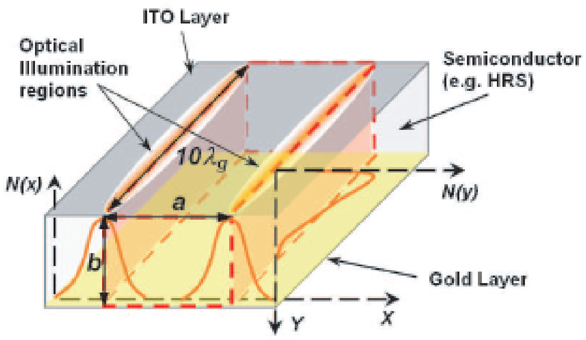

Figure 1.13: A RETINA waveguide and the plasma distribution inside the HRS substrate by a single-sided illumination [30].

1.3 Conclusion

A brief introduction to the effects of a laser excitation in a semiconductor material has been presented. Also, a comprehensive review of past and current attempts to design and realise optically-controlled microwave, millimeter-wave and THz structures has been conducted. With first attempts focused on the use of picosecond illumination, and later on with CW illumination receiving an increasing research interest, various optoelectronic devices for microwave and millimeter wave applications have been proposed. However, only recently the development of THz tunable components with the use of semiconductor structures, such as PPWGs and photonic crystals has been investigated. With rising demand for reconfigurable structures (e.g. switches and modulators) at the THz frequency range and with photoconductive semiconductors being a very attractive option, research in the emerging field of optically-controlled THz devices is still an important issue.

References

[1] R. B. Adler, A. C. Smith and R. L. Longini, "Introduction to Semiconductor Physics", *Wiley*, New York, 1964

[2] A. Ambroziak, "Semiconductor photoelectric devices", *Iliffe Books*, London, 1968

[3] W. Platte and B. Sauerer, "Optically CW-induced losses in semiconductor coplanar waveguides", *IEEE Trans. Microw. Theory Techn.*, vol. 37, no. 1, pp. 139-149, Jan. 1989

[4] W. Platte, "Effective photoconductivity and plasma depth in optically quasi-CW controlled microwave switching devices", *IEE Proc.-J Optoelectron.*, vol. 135, no. 3, pp. 251-254, Jun. 1988

[5] S. Jayaraman and C. H. Lee, "Observation of two-photon conductivity in GaAs with nanosecond and picosecond light pulses", *Appl. Phys. Lett.*, vol. 20, no. 10, pp. 392-395, May 1972

[6] D. H. Auston, "Picosecond optoelectronic switching and gating in silicon", *Appl. Phys. Lett.*, vol. 26, no. 3, pp. 101-103, Feb. 1975

[7] A. M. Johnson and D. H. Auston, "Microwave switching by picosecond photoconductivity", *IEEE J. Quant. Electron.*, vol. 11, no. 6, pp. 283-287, Jun. 1975

[8] W. Platte, "High speed optoelectronic switching in silicon gap-shunt microstrip structures", *Electron. Lett.*, vol. 12, no. 17, pp. 437-438, Aug. 1976

[9] C. H. Lee, "Picosecond optoelectronic switching in GaAs", *Appl. Phys. Lett.*, vol. 30, no. 2, pp. 84-86, Jan. 1977

[10] W. Platte, "Optoelectronic microwave switching", *IEE Proc.-J Optoelectron.*, vol. 132, no. 2, pp. 126-132, Apr. 1985

[11] C. H. Lee, "Picosecond optics and microwave technology", *IEEE Trans. Microw. Theory Techn.*, vol. 38, no. 5, pp. 596-607, May 1990

[12] W. Platte, "Effect of surface recombination on microwave performance of laser-induced DBR gratings in silicon coplanar waveguides", *IEE Proc.-J Optoelectron.*, vol. 139, no. 6, pp. 399-401, Dec. 1992

[13] W. Platte, "Optoelectronic microwave switching via laser-induced plasma tapers in GaAs microstrip sections", *IEEE Trans. Microw. Theory Techn.*, vol. 29, no. 10, pp. 1010-1018, Oct. 1981

[14] W. Platte, "Cutoff-taper performance of substrate excited optoelectronic switches", *IEE Proc.-I Solid-State Electron Dev.*, vol. 131, no. 2, pp. 45-50, Apr. 1984

[15] A. J. Low and J. E. Carroll, "10ps optoelectronic sampling system", *IEE J. Solid-State Electron Devices*, vol. 2, no. 6, pp. 185-190, Nov. 1978

[16] J. K. A. Everard and J. E. Carroll, "Practical comparison of optoelectronic sampling systems and devices", *IEE Proc. I Solid-State Electron Devices*, vol. 130, no.1, pp. 5-16, Feb. 1983

[17] W. Platte, "Spectral dependence of light-induced microwave reflection coefficient from optoelectronic waveguide gratings", *IEEE Trans. Microw. Theory Techn.*, vol. 43, no. 1, pp. 106-111, Jan. 1995

[18] W. Platte, S. Ruppik and M. Guetschow, "Optically induced mask-controlled time-variable periodic microwave structures", *IEEE Trans. Microw. Theory Techn.*, vol. 48, no. 5, pp. 846-851, May 2000

[19] P. J. Liu ; D. S. Zhao and B. Z. Wang, "Design of optically controlled microwave switch for reconfigurable antenna systems", *Int. Conf. Microw. Millim. Wave Techn.*, pp. 1-4, Apr. 2007

[20] C. H. Lee, P. S. Mak and A. P. Defonzo, "Optical control of millimeter-wave propagation in dielectric waveguides", *IEEE J. Quant. Electron.*, vol. 16, no. 3, pp. 277- 288, Mar. 1980

[21] S. K. Dana, H. Shimasaki and M. Tsutsumi, "Efficient optical control of millimeter waves in a slot line on semiconductor plasma substrate", *IEEE Trans. Microw. Theory Techn.*, vol. 50, no. 1, pp. 207- 210, Jan. 2002

[22] G. Hadjicostas, M. W. Scott and J. K. Butler, "Optically controlled millimeter wave phase shifter in a metallic waveguide", *Int. Microw. Symp.*, vol. 2, pp. 657-660, Jun. 1987

[23] P. A. S. Cruickshank, D. A. Robertson and G. M. Smith, "Nanosecond risetime optically-activated mm-wave waveguide switch", *Int. Conf. Infrared Millim. Terahertz Waves*, vol. 1, pp. 277-278, Sep.

[24] A. M. Vaucher, C. D. Striffler and C. H. Lee, "Theory of optically controlled millimeter-wave phase shifters", *IEEE Microw. Theory Techn.*, vol. 31, no. 2, pp. 209-216, Feb. 1983

[25] G. W. Webb, W. Vernon, M. S. Sanchez, S. C. Rose and S. Angello, "Optically controlled millimeter wave antenna", *Int. Microw. Photon.*, vol. 1, pp. 275-278, Nov. 1999

[26] D. G. Cooke and P. Uhd Jepsen, "Optical modulation of terahertz pulses in a parallel plate waveguide", *Opt. Express*, vol. 16, no. 19, pp. 15123-15129 Sep. 2008

[27] L. Fekete, F. Kadlec, P. Kuel and H. Nmec, "Ultrafast opto-terahertz photonic crystal modulator", *Opt. Lett.*, vol. 32, no. 6, pp. 680-682, Feb. 2007

[28] E. Hendry, M. J. Lockyear, J. Gmez Rivas, L. Kuipers, and M. Bonn, "Ultrafast optical switching of the THz transmission through metallic subwavelength hole arrays", *Phys. Rev. B*, vol. 75, no. 23, p. 235305, Jan. 2007

[29] N. H. Shen, M. Massaouti, M. Gokkavas, J. M. Manceau, E. Ozbay, M. Kafesaki, T. Koschny, S. Tzortzakis, and C. M. Soukoulis, "Optically Implemented Broadband Blueshift Switch in the Terahertz Regime", *Phys. Rev. Lett.*, vol. 106, no. 3, p. 037403, Jan. 2011

[30] Y. Zhou and S. Lucyszyn, "Modelling of reconfigurable terahertz integrated architecture (RETINA) SIW structures", *PIER*, vol. 105, pp. 71-92, Jun. 2010

[31] Y. Zhou, "Reconfigurable Terahertz Integrated Architecture (RETINA)", *PhD Thesis*, Imperial College London, 2009

[32] M. Sirbu,S. B. P. Lepaul and F. Aniel, "Coupling 3-D Maxwell's and Boltzmann's equations for analyzing a terahertz photoconductive switch", *IEEE Trans. Microw. Theory Techn.*, vol. 53, no. 9, pp. 2991-2998, Sep. 2005

[33] M. Tani, Y. Hirota, C. T. Que, S. Tanaka, R. Hattori, M. Yamaguchi, S. Nishizawa and M. Hangyo, "Novel Terahertz photoconductive antennas", *Int. J. Infrared Millim. Waves*, vol. 27, no. 4, Apr. 2006

Chapter 2

Defining Material Parameters in Electromagnetic Solvers for Arbitrary THz Structures

In this chapter an exhaustive study of the full-wave simulation approaches is undertaken in order to investigate the weaknesses and limitations with commercially-available solvers. This is found to be necessary based on issues reported in the open literature and after erroneous results obtained in the initial modelling of the devices. In general, frequency-domain solvers are used extensively for modelling arbitrary terahertz structures. Four well-known commercially available electromagnetic (EM) modelling software packages include HFSS™, CST Microwave Studio®, EMPro and RSoft. However, there are a number of issues that relate to how they can be used to obtain more meaningful and accurate results. Even experienced users of these and similar software packages may not fully appreciate some of the subtle ambiguities in defining boundaries and material parameters for use in THz applications. Here, a detailed comparative study has been undertaken, in consultation with all four vendors. First, in order to avoid introducing ambiguities, frequency dispersion in materials has to be clearly defined from first principles (in both intrinsic and effective forms). Different frequency dispersion models are then introduced for "metal-like" materials. To act as benchmark structures, conventional air-filled metal-pipe rectangular waveguides, associated cavity resonators and a spoof surface plasmon waveguide have been simulated, using a raft of different approaches, with a view to illustrating quantifiable weaknesses in commercial software packages for simulating arbitrary metal-based THz structures. This chapter highlights intuitive and logical approaches that give incorrect results and, where possible, makes recommendations for the most appropriate solutions that have hitherto not been given in technical notes.

2.1 Introduction

Over the past two decades, there has been increasing interest in the 0.3 to 10 THz frequency range for a variety of applications. Currently, the "THz gap" is used for highly specialised applications (e.g., radiometric imaging and spectroscopy). However, in order to fully exploit this part of the frequency spectrum and, thus, open up the "THz gap" to ubiquitous applications, there will be increasing reliance on the use of commercial electromagnetic (EM) modelling software (e.g., HFSS™ [1–9], CST Microwave Studio® [8–11] and RSoft [12–17]) to predict the performance of metal-based terahertz structures. However, in the 0.3 to 10 THz frequency range, dispersion in the conductivity of metal-based structures can affect results significantly and, therefore, has to be properly taken into account when passive components are modelled.

While commercially-available software packages can generally predict the performance of arbitrary 3D structures, the correct approach to selecting the most appropriate boundary conditions, defining a material's parameters and being able to enter its real or complex values within the software are not always straightforward [18]. Indeed, it has been found that some intuitive and logical approaches yield incorrect results, which may not be apparent to even experienced EM software users [19–21].

First, relevant background theory for assigning material parameters for frequency dispersive media is given. This is necessary in order to avoid introducing ambiguities and errors. This chapter then investigates various approaches to modelling benchmark metal-based THz structures, using four well-known software packages: Ansys' High Frequency Structure Simulator (HFSS™), CST Microwave Studio® (CST MWS), Agilent's newly released Electromagnetic Professional (EMPro) and RSoft.

With few detailed measurements of passive metal-based structures, operating within in the "THz gap", being reported in the open literature [22], the classical relaxation-effect (or Drude dispersion) model has been adopted as reference. This phenomenological analytical model has previously been shown to fit accurate room temperature measurements in the lower terahertz range [22], unlike more empirical models [23].

Here, classical air-filled metal-pipe rectangular waveguides (MPRWGs) and associated cavity resonators are used as benchmark structures to represent the millimeter-wave community moving up in frequency into the "THz gap", while spoof (or designer) surface plasmon waveguides represent the optics community moving down in frequency into the "THz gap".

Within HFSS™ its frequency-domain solver employs the finite-element method (FEM), with its ability to handle complex geometries efficiently, while within CST MWS, high frequency 3D EM field simulation can be performed using the frequency-domain solver based on the finite integration technique (FIT). Within EMPro its frequency-domain solver employs FEM, while within RSoft its FemSIM is a generalized mode solver based on FEM, which can calculate transverse and cavity modes of any 1D or 2D cross-section. In consultation with all four associated vendors, all possible modelling strategies have been investigated in depth and, for the first time, detailed recommendations for the most appropriates solutions are given.

2.2 Frequency Dispersion in Materials

2.2.1 Intrinsic and Effective Material Parameters

It will be seen later that one of the main issues associated with inaccurate modelling is related to ambiguities introduced during material parameter definition. For this reason, it is first necessary to reproduce textbook theory that underpins frequency-domain solvers. The relevant background to defining material parameters for frequency dispersive media starts with the generalized Ampere's law (with the associated variables having their usual meaning) [24]:

$$\nabla \times \mathbf{H} = \mathbf{J}_{\mathrm{f}} + \frac{\partial \mathbf{D}}{\partial t} \tag{2.1}$$

where $\mathbf{J}_{\mathrm{f}} = \mathbf{J}_{\mathrm{i}} + \mathbf{J}_{\mathrm{c}}$. Assuming that the impressed (external) current density $\mathbf{J}_{\mathrm{i}}$ is zero, the free current density $\mathbf{J}_{\mathrm{f}}$ reduces to the conduction current density $\mathbf{J}_{\mathrm{c}}$. For an isotropic, linear and dispersive medium the constitutive equations can be written as [24]:

$$\mathbf{D} = \varepsilon \mathbf{E} + \varepsilon_1 \frac{\partial \mathbf{E}}{\partial t} + \varepsilon_2 \frac{\partial^2 \mathbf{E}}{\partial t^2} + \varepsilon_3 \frac{\partial^3 \mathbf{E}}{\partial t^3} + \cdots \tag{2.2}$$

$$\mathbf{B} = \mu \mathbf{H} + \mu_1 \frac{\partial \mathbf{H}}{\partial t} + \mu_2 \frac{\partial^2 \mathbf{H}}{\partial t^2} + \mu_3 \frac{\partial^3 \mathbf{H}}{\partial t^3} + \cdots \tag{2.3}$$

$$\mathbf{J}_{\mathrm{c}} = \sigma \mathbf{E} + \sigma_1 \frac{\partial \mathbf{E}}{\partial t} + \sigma_2 \frac{\partial^2 \mathbf{E}}{\partial t^2} + \sigma_3 \frac{\partial^3 \mathbf{E}}{\partial t^3} + \cdots \tag{2.4}$$

where ε_q, μ_q and σ_q are weighting factors for the higher order terms. Now, (2.1)-(2.4) can be expressed for the steady-state frequency domain (with $e^{j\omega t}$ time harmonic dependence, where ω is the angular frequency) as follows:

$$\nabla \times \mathbf{H} = \mathbf{J}_{\mathrm{f}} + j\omega \mathbf{D} \tag{2.5}$$

$$\mathbf{D} = \varepsilon \mathbf{E} + j\omega \varepsilon_1 \mathbf{E} - \omega^2 \varepsilon_2 \mathbf{E} - j\omega^3 \varepsilon_3 \mathbf{E} + \cdots \equiv \Big(\underbrace{\varepsilon'(\omega) - j\varepsilon''(\omega)}_{\varepsilon(\omega)} \Big) \mathbf{E} \tag{2.6}$$

$$\mathbf{B} = \mu \mathbf{H} + j\omega \mu_1 \mathbf{H} - \omega^2 \mu_2 \mathbf{H} - j\omega^3 \mu_3 \mathbf{H} + \cdots \equiv \Big(\underbrace{\mu'(\omega) - j\mu''(\omega)}_{\mu(\omega)} \Big) \mathbf{H} \tag{2.7}$$

$$\mathbf{J}_{\mathrm{c}} = \sigma \mathbf{E} + j\omega \sigma_1 \mathbf{E} - \omega^2 \sigma_2 \mathbf{E} - j\omega^3 \sigma_3 \mathbf{E} + \cdots \equiv \Big(\underbrace{\sigma'(\omega) - j\sigma''(\omega)}_{\sigma(\omega)} \Big) \mathbf{E} \tag{2.8}$$

where $\varepsilon(\omega)$, $\mu(\omega)$ and $\sigma(\omega)$ describe the intrinsic bulk effects of polarization, magnetization and conductivity, in complex notation form, respectively. It is worth mentioning that with normal metals at room temperature $\varepsilon(\omega) \cong \varepsilon_0$, while with non-magnetic materials $\mu(\omega) = \mu_0$ and with low frequency room temperature modelling of materials $\sigma(\omega) \cong \sigma_0$ (intrinsic bulk conductivity at dc). In the more general case, (2.5)-(2.8) yield the following:

$$\begin{aligned} \nabla \times \mathbf{H} = \mathbf{J}_{\mathrm{c}} + j\omega \mathbf{D} &= \Big(\underbrace{\sigma(\omega) + j\omega\varepsilon(\omega)}_{\sigma_{\mathrm{eff}}(\omega)} \Big) \mathbf{E} \\ &= j\omega \Bigg(\underbrace{\varepsilon(\omega) - j\frac{\sigma(\omega)}{\omega}}_{\varepsilon_{\mathrm{eff}}(\omega)} \Bigg) \mathbf{E} \end{aligned} \tag{2.9}$$

From (2.9) it is obvious that the effective parameters $\varepsilon_{\mathrm{eff}}(\omega)$ and $\sigma_{\mathrm{eff}}(\omega)$ can be used interchangeably, being related to each other by the textbook expression:

$$\sigma_{\mathrm{eff}}(\omega) = j\omega \varepsilon_{\mathrm{eff}}(\omega) \tag{2.10}$$

where the effective permittivity $\varepsilon_{\mathrm{eff}}(\omega) = \varepsilon_0 \varepsilon_{\mathrm{r,eff}}(\omega)$ and $\varepsilon_{\mathrm{r,eff}}(\omega)$ is the relative effective permittivity, also referred to as the dielectric function. However, this should not be confused with the dielectric constant, which represents only the real part of the relative effective permittivity.

Now, partitioning (2.9) into its real and imaginary parts, the following is obtained:

$$\begin{aligned}\nabla \times \mathbf{H} &= \Big[\Big(\underbrace{\sigma'(\omega) + \omega\varepsilon''(\omega)}_{\sigma'_{\text{eff}}(\omega)}\Big) - j\Big(\underbrace{\sigma''(\omega) - \omega\varepsilon'(\omega)}_{\sigma''_{\text{eff}}(\omega)}\Big)\Big]\mathbf{E} \\ &= j\omega\Bigg[\Bigg(\underbrace{\varepsilon'(\omega) - \frac{\sigma''(\omega)}{\omega}}_{\varepsilon'_{\text{eff}}(\omega)}\Bigg) - j\Bigg(\underbrace{\varepsilon''(\omega) + \frac{\sigma'(\omega)}{\omega}}_{\varepsilon''_{\text{eff}}(\omega)}\Bigg)\Bigg]\mathbf{E}\end{aligned} \tag{2.11}$$

By rearranging (2.11) for $\varepsilon_{\text{eff}}(\omega)$ the effective dielectric loss tangent $\tan\delta_{\text{e}}(\omega)$ is defined (even for a metal [25]) as follows:

$$\begin{aligned}\varepsilon_{\text{eff}}(\omega) &= \varepsilon'_{\text{eff}}(\omega)\big(1 - j\tan\delta_{\text{e}}(\omega)\big) \quad \text{where} \\ \tan\delta_{\text{e}}(\omega) &\equiv \frac{\varepsilon''_{\text{eff}}(\omega)}{\varepsilon'_{\text{eff}}(\omega)} = \frac{\varepsilon''_{\text{r,eff}}(\omega)}{\varepsilon'_{\text{r,eff}}(\omega)} = \frac{\sigma'_{\text{eff}}(\omega)}{\sigma''_{\text{eff}}(\omega)}\end{aligned} \tag{2.12}$$

As can be seen from (2.12), the dielectric loss tangent quantifies the losses for a non-magnetic material but it does not distinguish the origins of different loss mechanisms. In other words, it does not give any information about the polarisation or conductivity loss contributions separately. This means that when material parameters are being evaluated experimentally the effective parameters (including $\tan\delta_{\text{e}}$) should be used. However, in the open literature, many authors loosely use the terminology "*complex permittivity*" or "*complex conductivity*" to describe the effective parameters, based on the fact that the effective parameters are complex numbers [26–30]. This can be confusing if not defined explicitly, since the intrinsic permittivity and conductivity themselves can be complex numbers. Thus, it may be ambiguous as to whether the authors are referring to the intrinsic parameters $\varepsilon(\omega)$, $\sigma(\omega)$ or to their associated effective parameters $\varepsilon_{\text{eff}}(\omega)$, $\sigma_{\text{eff}}(\omega)$ – with the latter set always being complex numbers, even when the former are represented by purely real quantities. For example, in the case where frequency dispersion of polarization can be neglected (e.g., metals having $\varepsilon'(\omega) \cong \varepsilon_0$ and $\varepsilon''(\omega) = 0$):

$$\varepsilon_{\text{eff}}(\omega) = \left(\varepsilon'(\omega) - \frac{\sigma''(\omega)}{\omega}\right) - j\left(\frac{\sigma'(\omega)}{\omega}\right) \tag{2.13}$$

$$\tan\delta_{\text{e}}(\omega) = \frac{\sigma'(\omega)}{\omega\varepsilon'(\omega) - \sigma''(\omega)} \tag{2.14}$$

To this end, (2.6)-(2.8) must always be compatible with the principle of conservation of energy, which in electromagnetic systems can be expressed by Poynting's theorem. Also, the passivity of such materials implies that the power dissipated per cycle per unit volume must be non-negative. Thus,

$$\Re\left\{\frac{1}{2}\mathbf{E}\cdot\mathbf{J}_{\text{c}}^* + \frac{j\omega}{2}\Big(\mathbf{B}\cdot\mathbf{H}^* - \mathbf{E}\cdot\mathbf{D}^*\Big)\right\} \geqslant 0 \tag{2.15}$$

with the equality only being valid for a lossless material. Substituting (2.6)-(2.8) into (2.15) and re-writing in quadratic form gives:

$$\Re\left\{\begin{bmatrix}\mathbf{E}^* & \mathbf{H}^*\end{bmatrix}\begin{bmatrix}\sigma'(\omega) + \omega\varepsilon''(\omega) + j\left(\sigma''(\omega) - \omega\varepsilon'(\omega)\right) & 0 \\ 0 & j\omega\left(\mu'(\omega) - j\mu''(\omega)\right)\end{bmatrix}\begin{bmatrix}\mathbf{E} \\ \mathbf{H}\end{bmatrix}\right\} \geqslant 0 \tag{2.16}$$

Using the general relationship:

$$\Re\Big\{\mathbf{A}^{*}\!\cdot\mathbf{M}\!\cdot\mathbf{A}\Big\} = \mathbf{A}^{*}\!\cdot\mathbf{M}'\!\cdot\mathbf{A} \text{ where } \mathbf{M}' = \frac{\mathbf{M}+\mathbf{M}^{\dagger}}{2} \tag{2.17}$$

where † represents the conjugate transpose matrix and taking into account that (2.16) holds for arbitrary electric and magnetic fields, the matrix $\mathbf{M}'$ must be positive semi-definite. This is ensured by the following two conditions:

$$\sigma'_{\text{eff}}(\omega) = \Big(\sigma'(\omega) + \omega\varepsilon''(\omega)\Big) \geqslant 0 \tag{2.18}$$

$$\text{and} \quad \mu''(\omega) \geqslant 0 \tag{2.19}$$

In order that (2.18) holds for arbitrary frequencies, the conditions $\sigma'(\omega) \geqslant 0$ and $\varepsilon''(\omega) \geqslant 0$ have to be verified.

When the classical relaxation-effect model for normal metals at room temperature is used, the intrinsic bulk conductivity is given by the following expression [20, 25]:

$$\sigma(\omega) = \frac{\sigma_0}{1+j\omega\tau} = \Bigg(\underbrace{\frac{\sigma_0}{1+\omega^2\tau^2}}_{\sigma'(\omega)}\Bigg) - j\Bigg(\underbrace{\frac{\sigma_0\omega\tau}{1+\omega^2\tau^2}}_{\sigma''(\omega)}\Bigg) \tag{2.20}$$

where τ is the phenomenological scattering relaxation time (also referred to as the collision time by HFSS™ and CST MWS) and both $\sigma'(\omega)$ and $\sigma''(\omega)$ are always positive numbers.

It is important to note that if a time dependence of the form $e^{-j\omega t}$ is used, all the previous equations must be replaced with their complex conjugate, resulting in material parameters being redefined by the forms $\varepsilon(\omega) = \varepsilon'(\omega)+j\varepsilon''(\omega)$, $\mu(\omega) = \mu'(\omega)+j\mu''(\omega)$, $\sigma(\omega) = \sigma'(\omega)+j\sigma''(\omega)$ and $\sigma_{\text{eff}}(\omega) = -j\omega\varepsilon_{\text{eff}}(\omega) = \sigma(\omega) - j\omega\varepsilon(\omega)$. While this point may seem obvious, errors will be introduced when parameters and equations that adopt different conventions (e.g., when originating from different sources) are inadvertently mixed during the modelling process. By default, HFSS™, CST MWS and EMPro adopt the $e^{j\omega t}$ convention; while RSoft adopts the $e^{-j\omega t}$ convention.

2.2.2 Frequency Dispersion in Metals

Equation (2.20) represents the classical relaxation-effect model for describing the frequency-temperature dispersion due to free carriers within a normal material; while the simple relaxation-effect model and the classical skin-effect model are derived by taking into account only the real parts of intrinsic bulk conductivity $\sigma'(\omega)$ and σ_0, respectively [20, 25]. For a generic material, its intrinsic impedance η (e.g., representing the surface impedance Z_{s} of a metal) is given by the following textbook expression:

$$\eta = \sqrt{\frac{\mu(\omega)}{\varepsilon_{\text{eff}}(\omega)}} = \sqrt{\frac{j\omega\mu(\omega)}{\sigma_{\text{eff}}(\omega)}} = \sqrt{\frac{j\omega\mu(\omega)}{\sigma(\omega)+j\omega\varepsilon(\omega)}} \equiv Z_{\text{s}} \tag{2.21}$$

With normal metals, one can neglect the dispersion effects in magnetization, so that $\mu'(\omega) = \mu_0\mu'_{\text{r}}$ and $\mu''(\omega)$=0 (while at terahertz frequencies $\mu'_{\text{r}} \sim 1$) [31] and assuming a metal with sufficiently high conductivity so that the displacement current term can be neglected (i.e., $\sigma_{\text{eff}}(\omega) \cong \sigma(\omega)$):

$$Z_{\text{s}} = R_{\text{s}} + jX_{\text{s}} \cong \sqrt{\frac{j\omega\mu_0\mu'_{\text{r}}}{\sigma(\omega)}} \tag{2.22}$$

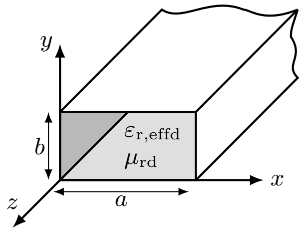

Figure 2.1: Uniform dielectric-filled MPRWG benchmark structure.

For the three aforementioned frequency dispersion models, (2.22) can be expanded out using the following expressions for the surface resistance and reactance [20, 25]:

Classical relaxation-effect (or Drude dispersion) model

$$\begin{aligned} R_{\text{s}} &= R_{\text{so}}\sqrt{\sqrt{1+(\omega\tau)^2}-\omega\tau} = X_{\text{s}}\left(\sqrt{1+(\omega\tau)^2}-\omega\tau\right) \\ X_{\text{s}} &= R_{\text{so}}\sqrt{\sqrt{1+(\omega\tau)^2}+\omega\tau} = R_{\text{s}}\left(\sqrt{1+(\omega\tau)^2}+\omega\tau\right) \end{aligned} \tag{2.23}$$

Simple relaxation-effect model

$$R_{\text{s}} = R_{\text{so}}\sqrt{1+(\omega\tau)^2} \text{ and } X_{\text{s}} = R_{\text{s}} \tag{2.24}$$

Classical skin-effect model

$$R_{\text{s}} = R_{\text{so}} = \sqrt{\frac{\omega\mu_0\mu_{\text{r}}'}{2\sigma_0}} \text{ and } X_{\text{s}} = R_{\text{s}} \tag{2.25}$$

2.3 THz Metal-Pipe Rectangular Waveguide Modelling

Metal-pipe rectangular waveguides and associated cavity resonators are simulated at THz frequencies, where frequency dispersion in conductivity has previously been found to affect predicted results [20, 32]. A MPRWG with internal dimensions $a \times b = 100 \times 50$ µm^2 (i.e., JPL-100 standard [20, 33]), with gold walls having room-temperature parameter values of $\sigma_0 = 4.517 \cdot 10^7$ S/m, $\tau = 27.135$ fs and $\mu_{\text{r}}' = 0.99996$ [22], was used as a benchmark structure, as illustrated in Fig. 2.1. To simplify the analysis, this waveguide is assumed to operate in the fundamental TE_{10} mode, so that closed-form analytical expressions can be used for direct comparison with the numerical simulation results. For example, the propagation constants γ_{mn} for a MPRWG supporting TE_{mn} modes can be calculated using the variational method [34], which can be expressed in the simpler form for TE_{m0} modes as follows [35]:

$$\gamma_{\text{m0}}^2 = \Gamma_{\text{d}}^2 - j\frac{2Z_s}{\omega\mu_0\mu_{\text{rd}}'b}\left[\left(\frac{\Gamma_{\text{d}}m\pi}{k_{\text{cd}}a}\right)^2 - k_{\text{cd}}^2\left(1+\frac{2b}{a}\right)\right] \tag{2.26}$$

$$\begin{aligned} \Gamma_{\text{d}}^2 &= k_{\text{cd}}^2 - k_{\text{0d}}^2 \\ k_{\text{cd}} &= \omega_{\text{c}}\sqrt{\mu_0\mu_{\text{rd}}'\varepsilon_0\varepsilon_{\text{r,effd}}'} \\ k_{\text{0d}} &= \omega\sqrt{\mu_0\mu_{\text{rd}}'\varepsilon_0\varepsilon_{\text{r,effd}}'(1-j\tan\delta_{\text{ed}})} \end{aligned}$$

where $\mu'_{\rm rd}$, $\varepsilon'_{\rm r,effd}$ and $\tan\delta_{\rm ed}$ are the relative permeability, dielectric constant and loss tangent for the dielectric filler, respectively.

In HFSS™, the classical skin-effect model is employed, by default, with σ_0 being entered in the material setup dialog box. Alternatively, the simple relaxation-effect model can be used by entering a data file containing the non-complex (i.e., real notation form) conductivity values calculated *a priori* at each discrete frequency point. In order to speed up the simulation times, solid metal walls can be replaced by boundaries. Both frequency dispersion models can be used in the material parameters for a 3D "solid object" or boundary condition. With the former, the use of bulk meshing is dependent on the threshold value of conductivity (for HFSS™ this is 10^5 S/m, by default). It must be noted, however, that the classical relaxation-effect model cannot be used directly, while current versions of HFSS™ (e.g., up to version 13) allow complex numbers to be entered into the conductivity value field it does not actually support these complex values [20], as will be explained here in greater detail.

For example, with the Finite Conductivity Boundary (FCB), complex conductivity values can be entered using the following syntaxes: $\sigma' - \sigma''j$ or $\sigma' - \sigma''i$. Here, the imaginary term σ'' is simply ignored in calculations, thus giving results that coincide with the simple relaxation-effect model [20]. Alternatively, complex conductivity values can be entered using the following suggested syntax [36]: $cmplx(\sigma', \sigma'')$, where $\sigma'' \geqslant 0$. Unfortunately, it has been found that this latter method gives incorrect results, as can be seen in Fig. 2.2 with the modelling of attenuation constant for a uniform air-filled MPRWG. However, with the Layered Impedance Boundary (LIB), $\varepsilon'_{\rm r,eff}$ and σ' can be entered directly, so long as the metal's dielectric loss tangent is set to zero, yielding the correct results. It should be pointed out that when only the intrinsic conductivity is entered, as described previously with the complex notation form, the problems associated with the LIB are also the same for the FCB. Alternatively, with the Impedance Boundary (IB), the appropriate complex surface impedance $Z_{\rm s}$ can be entered directly at each discrete frequency point. In this case, as can be seen in Fig. 2.2 the results reported by HFSS™are in excellent agreement with the classical relaxation-effect model with (2.26). It must be noted that since the complex value of surface impedance must be entered *a priori*, significant errors may result if tuning or optimisation routines are employed with structures where the spectral features of interest can shift to frequencies not represented by the list of discrete frequency points that give the associated values of complex surface impedances.

The above approaches are also found in CST MWS (e.g., versions up to 2011 service pack 7), where the simple relaxation-effect and classical skin-effect models can be applied to the bulk conductivity of a solid object or Conducting Wall Boundary (CWB). However, with the simple relaxation-effect model, the conductivity values have to be entered at each discrete frequency point, since the software does not currently support a data file import for conductivity. Alternatively, one could define a "normal material" type, whose permittivity is given by the relative effective value calculated using (2.13) and assuming $\sigma'' = 0$, and then enter a data file containing the permittivity values as a "user defined" dispersion model. However, the results were still found to be inaccurate, probably due to poor meshing inside the metal. Again, the classical relaxation-effect model cannot be used explicitly, but the "Surface Impedance" Material (SIM) type can be defined with a data file containing the complex surface impedance values at each discrete frequency point. Fortunately, CST MWS

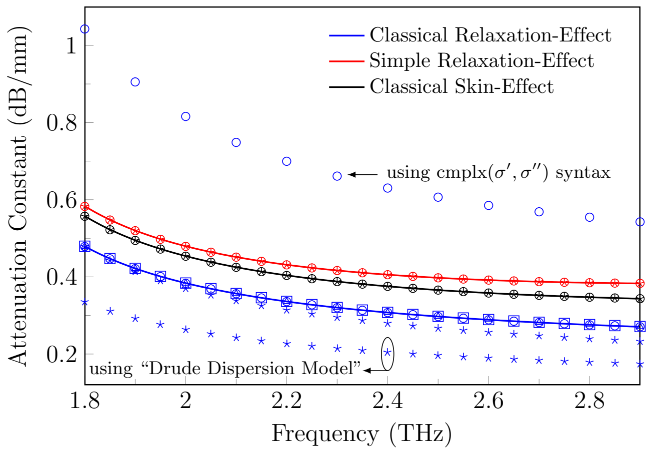

Figure 2.2: Attenuation constant for the dominant TE_{10} mode with the 100 µm JPL band gold MPRWG. Lines: calculated values from analytical models using (2.26). Discrete symbols: simulated values (circles: HFSS™, stars: CST MWS, triangles: EMPro and squares: RSoft).

interpolates between data points and thus tuning or optimization routines can be employed, in contrast to HFSS™. Although, as can be seen in Fig. 2.2, the results increasingly diverge from the analytical model as frequency increases; the reason for this is unknown. Alternatively, an "ohmic sheet" material type can be used where the surface impedance is defined at each discrete frequency point. However, this approach is also found to give incorrect results.

In principle, the solid walls of the waveguide can be treated as dielectrics (i.e., a "normal material" type) by defining for the metal $\varepsilon_r' = 1$, the angular plasma frequency $\omega_p = \sqrt{\frac{\sigma_0}{\varepsilon_0 \tau}}$ and collision damping angular frequency $\omega_\tau = \frac{1}{\tau}$ (this approach is also used in RSoft). This also gives incorrect results, as seen from the "Drude Dispersion Model" results shown in Fig. 2.2, probably due to poor meshing. All the above approaches for HFSS™ and CST MWS are summarised in Table 2.1.

With EMPro (e.g., version 2011.11) frequency dispersive metals are not supported. Although there are frequency dispersion models for dielectrics, which can emulate metals by entering appropriate parameters, the losses are underestimated because of inadequate mesh densities inside the metal. Thus, the only way to obtain accurate results is by using a non-dispersive "Surface Resistance" (SR) material type, which actually corresponds to the real and imaginary parts of the surface impedance, entered at each discrete frequency point (as with the IB in HFSS™). In other words, iterative simulations have to be reassigned with new values for surface impedance at every frequency point. In the current version of EMPro, the thickness in the material setup window must be set to zero, for correct results, otherwise the losses reported are greater than expected and these losses increase with increasing thickness. Alternatively, the intrinsic bulk dc conductivity σ_0 of the material can be entered, giving results that coincide with the classical skin-effect model.

Finally, with RSoft, standard linear dispersion models can be used by entering their characteristic parameters ω_p and ω_τ for the metal, producing results that are in excellent agreement with the classical relaxation-effect model.

2.4 THz Cavity Resonator Modelling

Simple rectangular waveguide cavity resonators, operating in the dominant TE_{101} mode, have also been simulated using eigenmode solvers that predict the complex eigenmode frequencies $\widetilde{\omega}_0 = \omega_0' + j\omega_0''$, with the imaginary part of the of the eigenmode frequency representing the losses in a cavity resonator. With a non-zero surface reactance X_s, due to contributions from both the classical skin-effect and kinetic surface inductances [25], the lossless (or driven) resonant angular frequency $\omega_0 = |\widetilde{\omega}_0|$ of the cavity is reduced from the ideal resonant angular frequency ω_I. Furthermore, a non-zero surface resistance R_s, due to ohmic losses, results in further frequency detuning, shifting the natural resonant angular frequency down from ω_0 to the damped (or undriven) resonant angular frequency ω_0'. Thus, the overall level of natural frequency detuning is $\Delta\omega_0' = (\omega_I - \omega_0')$ [20].

In summary, at terahertz frequencies, when compared to the classical relaxation-effect model [20, 25] the classical skin-effect model overestimates the surface resistance (i.e., inflating losses) and underestimates surface reactance (i.e., undervaluing frequency detuning), while the simple relaxation-effect model gives reasonably good predictions for detuning, but greatly inflates losses.

Assuming losses are small enough, one can use the well-known expressions, derived using perturbation theory [20, 37], for calculating the lossless resonant frequency and the unloaded quality factor at this frequency, where the quality factor is generally defined as 2π times the ratio of the energy stored in the cavity resonator to the energy dissipated per cycle in the cavity. Solving (2.27) for the lossless resonant frequency ω_0 [20], from (2.28) the corresponding unloaded quality factor, Q_u can be easily obtained.

$$X_s(\omega_0) - 2\Gamma\left(\omega_I - \omega_0\right) = 0 \tag{2.27}$$

$$R_s(\omega_0) = \frac{\omega_I \Gamma}{Q_u(\omega_0)} \tag{2.28}$$

For the TE_{101} mode, Γ represents the geometrical factor given by the textbook expression

$$\Gamma = \mu_0 \left(\frac{abd\left(a^2 + d^2\right)}{2\left[2b\left(a^3 + d^3\right) + ad\left(a^2 + d^2\right)\right]} \right) \quad [\mathrm{H}] \tag{2.29}$$

It should be noted that both HFSS™ and CST MWS use frequency $f = \omega/2\pi$, rather than angular frequency ω, when entering parameters or displaying results, unless explicitly stated (e.g., plasma angular frequency in CTS MWS).

The simulated and calculated values for the unloaded Q-factor $Q_u(f_0)$ and the overall frequency detuning $(f_I - f_0')$ are plotted in Fig. 2.3, for a variety of gold rectangular cavities having respective internal width, height and length dimensions of $a \times b \times d = a \times a/2 \times \sqrt{2}a$ [20]. With the classical skin-effect model, without and with the displacement current term, respectively, both the FCB and LIB can be used by entering σ_0. However, for the simple and classical relaxation-effect models, the user must follow one of the approaches outlined below.

2.4.1 HFSS$^{\text{TM}}$ with Finite Conductivity Boundary and Impedance Boundary

With the simple relaxation-effect model, the FCB and IB can be used by entering the conductivity $\sigma'(f_{\text{I}})$ and complex surface impedance $Z_{\text{s}}(f_{\text{I}})$ values, respectively, with values calculated at the ideal resonant frequency f_{I}. As can be seen in Fig. 2.3, the convenient choice of using the ideal resonant frequency gives a reasonably good approximation, in terms of predicting the amount of frequency detuning $(f_{\text{I}} - f_0')$ and unloaded quality factor $Q_{\text{u}}(f_0)$.

Note that, in HFSS™, the unloaded Q-factor is calculated with the assumption that the eigenfrequency of a mode can be represented by the complex resonant frequency of a lumped-element RLC resonator, i.e., defined by the following [37]:

$$Q_{\text{u}}(f_0) = \frac{f_0}{2f_0''} \tag{2.30}$$

where $f_0 = |\tilde{f}_0|$ and $\tilde{f}_0 = f_0' + jf_0''$. It will be seen that (2.30) is inherently sensitive to errors in the complex resonant frequency $\tilde{f}_0$.

With the classical relaxation-effect model, the FCB cannot be used (as it does not support complex conductivity values). However, by entering $Z_{\text{s}}(f_{\text{I}})$, IB can give excellent results when frequency detuning is not too large.

For this benchmark structure, given its simple geometrical shape, the ideal resonant frequency can be easily calculated for large conductivities. However, with a more complicated geometrical structure, it may not be possible to predict the ideal resonant frequencies for each and every mode and so this approach cannot be used to give accurate results.

2.4.2 HFSS$^{\text{TM}}$ with Layered Impedance Boundary

With the LIB, unlike with the FCB, the eigenmode solver supports frequency-dependent material parameters and can be used for arbitrary structures *without a priori* knowledge of the ideal resonant frequency. However, for accurate results, the starting frequency that the user enters during setup has to be very close to the real part of the complex eigenfrequency f_0' (but lower than f_0', so that the solver does not skip the mode of interest) in order for the software to accurately calculate f_0''. Otherwise, the results may contain significant errors in both f_0'' and unloaded quality factor $Q_{\text{u}}(f_0)$ calculated using (2.30). Unfortunately, the resonant frequency of an arbitrary structure is *not known a priori*.

To overcome this problem, one needs to simulate the structure using a single iteration, where the starting frequency in the iteration is very close (but lower) than the real part of the resonant frequency generated by the initial simulation. This is necessary in order for the software to accurately calculate f_0'' and, hence, $Q_{\text{u}}(f_0)$.

Alternatively, when the ideal resonant frequency f_I and unloaded Q-factor $Q_{\text{u}}(f_{\text{I}})$ are of most interest, rather than the damped resonant frequency f_0', it has been found that one can avoid the iterative simulation, without a priori knowledge of the resonant frequency, by having the starting frequency f_{s} well below resonance (i.e., $f_{\text{s}} \ll f_0'$). The damped resonant frequency obtained with this approach tends to the ideal resonant frequency (the lower the starting frequency the closer $f_0' \to f_{\text{I}}$). However, f_0'' and, hence, $Q_{\text{u}}(f_0)$ using (2.30) will be completely incorrect. Therefore, instead of using (2.30), the fields calculator can be employed to compute the unloaded quality factor from the following expression

$$Q_\mathrm{u}(f_0') = \frac{2\pi f_0'\Gamma}{R_\mathrm{s}(f_0')} \approx \frac{2\pi f_\mathrm{I}\Gamma}{R_\mathrm{s}(f_\mathrm{I})} = Q_\mathrm{u}(f_\mathrm{I}) \tag{2.31}$$

where f_0' is the real part of the complex eigenfrequency reported by the solver, $R_\mathrm{s}(f_0')$ is the surface resistance calculated at that frequency, given by (2.23) when neglecting the displacement current term, and Γ is the geometrical factor

$$\Gamma = \mu_0 \frac{\iiint\limits_V \mathbf{H}\cdot\mathbf{H}^* dV}{\iint\limits_S \mathbf{H}_\mathrm{t}\cdot\mathbf{H}_\mathrm{t}^* dS} \tag{2.32}$$

where V represents the internal volume of the cavity, S the internal surface area of the cavity walls and suffix "t" represents the field components tangential to the internal surface of the walls. This approach gives correct results for the unloaded quality factor $Q_\mathrm{u}(f_\mathrm{I})$, since it takes into account the fields distribution and, thus, its accuracy is not significantly compromised by errors in the complex eigenfrequencies. However, the user needs to manually mesh the dielectric filler (e.g., air in this case) inside the cavity to make it dense enough so that the corresponding fields are captured accurately. Furthermore, for sufficiently high conductivities, f_0' (and, therefore, f_0) tends to f_I, thus (2.31) approximately gives $Q_\mathrm{u}(f_\mathrm{I})$; the percentage error of $\left|\frac{Q_\mathrm{u}(f_0) - Q_\mathrm{u}(f_\mathrm{I})}{Q_\mathrm{u}(f_\mathrm{I})}\right| < 0.1\%$ is very small, which practically means that $Q_\mathrm{u}(f_0) \cong Q_\mathrm{u}(f_\mathrm{I})$ to a good approximation. Also, it should be noted that for faster convergence the box "*convergence on real frequency only*" must be ticked.

Although this latter approach produces accurate results for the unloaded Q-factor, it cannot provide accurate results for the frequency detuning and, thus, its use is limited to cases where only the ideal resonant frequency f_I and $Q_\mathrm{u}(f_\mathrm{I})$ are of interest.

2.4.3 CST MWS

In contrast to HFSS™, with CST MWS, the walls of the cavity are assumed to be Perfect Electric Conductors (PEC), because its eigenmode solver does not support lossy metals; the unloaded quality factor can be extracted by entering the conductivity of the metal at the post-processing stage. It should be noted that a normal metal can be emulated by a dielectric material, but this still requires a high meshing density; making it impractical. However, CST MWS does not report the actual complex eigenfrequency of the cavity, only the ideal resonant frequency f_I. The approximate complex eigenfrequency $\widetilde{\omega}_0$ can be calculated using the general solution for the lumped-element RLC resonators [37], adopted by HFSS™, but with the lossless resonant frequency f_0 and associated unloaded quality factor values $Q_\mathrm{u}(f_0)$ replaced by those generated by CST MWS, more specifically

$$\widetilde{f}_0 \sim f_\mathrm{I}\sqrt{1 - \left(\frac{1}{2Q_\mathrm{u}(f_\mathrm{I})}\right)^2} + j\frac{f_\mathrm{I}}{2Q_\mathrm{u}(f_\mathrm{I})} \tag{2.33}$$

Not surprisingly, as can been seen in Fig. 2.3, this approach results in a significant error when predicting frequency detuning. Once again, only real conductivity values can be entered and so this approach can only be used for the simple relaxation-effect and classical skin-effect models.

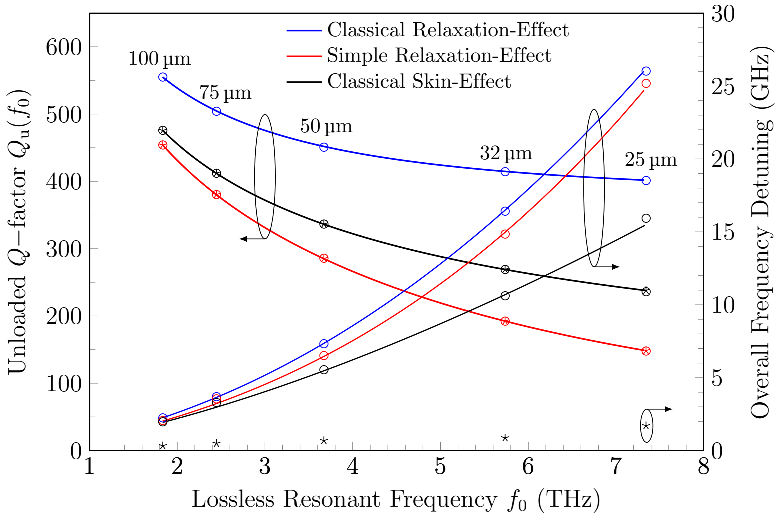

Figure 2.3: Unloaded Q-factor $Q_u(f_0)$ and frequency detuning $(f_I - f_0')$ for the TE_{101} mode gold cavity resonators for different cavity width dimensions a. Lines: calculated values from analytical models (2.27-2.29, 2.30). Circles: simulated values using HFSS™. Stars: simulated values using CST MWS (almost identical results for the frequency detuning with both simple relaxation-effect and classical skin-effect models).

2.4.4 EMPro and RSoft

With EMPro its eigenmode solver does not support frequency dispersive metals (this also applies to its FEM solver) and, thus, it cannot be used with either relaxation-effect models for arbitrary structures. However, in the unusually special case where the resonant frequency is known *a priori*, the surface impedance at the resonance can be entered (as with HFSS™), but this approach suffers from the same issues described previously.

Lastly, RSoft does not provide a 3D eigenmode solver and so the user has to excite the structure using its FullWave module, in order to obtain the damped resonant frequency f_0'. The use of its Finite-Difference Time-Domain (FDTD) solver is beyond the scope of this study. Table 2.1 summarises the modelling strategies for all the eigenmode solvers.

2.5 Spoof Surface Plasmon Waveguide Modelling

Spoof surface plasmons are a type of surface waves that are supported by a patterned metallic surface and widely modelled in various simulation domains [38–40]. Although a complete analysis is beyond the scope of this work, it will be shown using the available commercial frequency-domain software packages that there are differences in the simulation results. The benchmark structure has periodically spaced rectangular blind holes (i.e., open cavities) that do not completely perforate the metal film [41], as illustrated in Fig. 2.4. The width w and length l dimensions of the holes' aperture are 150 µm and 500 µm, respectively, with a periodicity d of 250 µm and depth h of either 100, 140 or 635 µm

Fig. 2.5 shows a comparison for PEC structures using the results from [41], obtained by FDTD simulations, and corresponding HFSS™ simulations, while Fig. 2.6 shows a comparison of the experimental measured results from [41],obtained by taking the Fourier

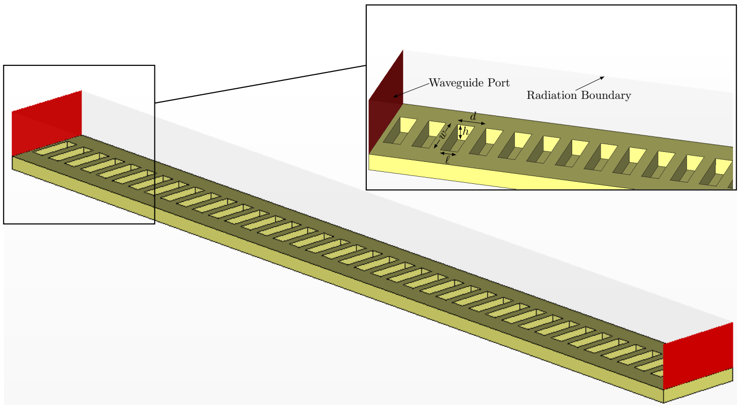

Figure 2.4: Spoof surface plasmon waveguide benchmark structure with 40 blind holes, having a 10 mm total length.

transform of time-domain measurements, and corresponding HFSS™ simulations using the FCB to model the fabricated aluminum structure. With $\sigma_0 = 3.767 \cdot 10^7$ S/m, $\tau = 7.407$ fs and $\mu_r' = 1.000021$ [22], $\sigma'(f)$ was calculated for use in the simple relaxation-effect model.

It is seen in Figs. 2.5 and 2.6 that HFSS™ predicts a much sharper upper cut-off frequency response than the corresponding results given in [41], which in turn gives a slightly higher frequency for the peak in transmission. However, they do agree in that as depth increases the upper cut-off frequency of the dominant mode shifts down in frequency. The data presented also differs because transmission is calculated from the amplitude of the electric field component along the propagation direction in [41], rather than by the S_{21} in HFSS™. In addition, from [41], the differences between their predicted and measured results shown in Figs. 2.5(a) and 2.6(a), respectively, are due to the introduction of ohmic losses (represented by the non-zero R_s) that degrades the slope of the cut-off frequencies and frequency detuning (represented by the non-zero X_s) that shifts the response down in frequency. In addition, there could be further detuning attributed to poor fabrication tolerances from the non-ideal manufacturing process. It should be noted that the data presented in [41] has been normalized with scaling factors that are not specified in their paper, therefore the HFSS™ results cannot be scaled to match those in [41].

Since HFSS™ modelling has been shown to behave as expected, CST MWS and EMPro were also used to simulate the structure in Fig. 2.4 having blind holes in a gold substrate.

The FCB boundary (or its equivalent) was used by all three software packages, as they were able to solve this problem in the frequency domain with waveguide excitations. RSoft was not considered for this more complicated 3D structure (i.e., having a non-uniform cross section, when compared to the MPRWG) because it would require the use of its time-domain solver, which is beyond the scope of this study.

The results are given in Fig. 2.7, showing that initial simulations with just the single dominant mode S_{21} provide widely varying predictions from each software package. Further simulations were then performed with the lowest five modes excited at the ports, but with the results extracted for the dominant mode S_{21}, as shown in Fig. 2.7. It can be seen that the software packages agree when more modes are included.

Fig. 2.8 shows that there is little difference between the various boundaries and frequency dispersion models employed when 5 modes are excited at the ports and then the total

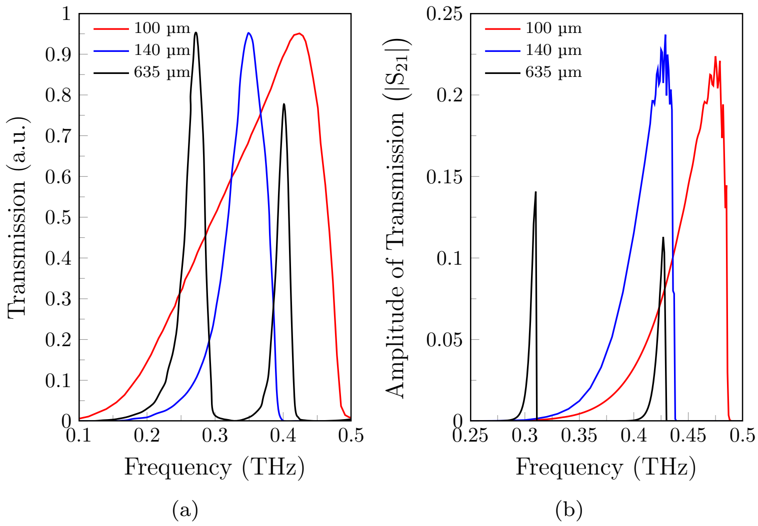

Figure 2.5: Simulated transmission results for PEC structure with different blind hole depths from: (a) results in [41] and (b) HFSS™.

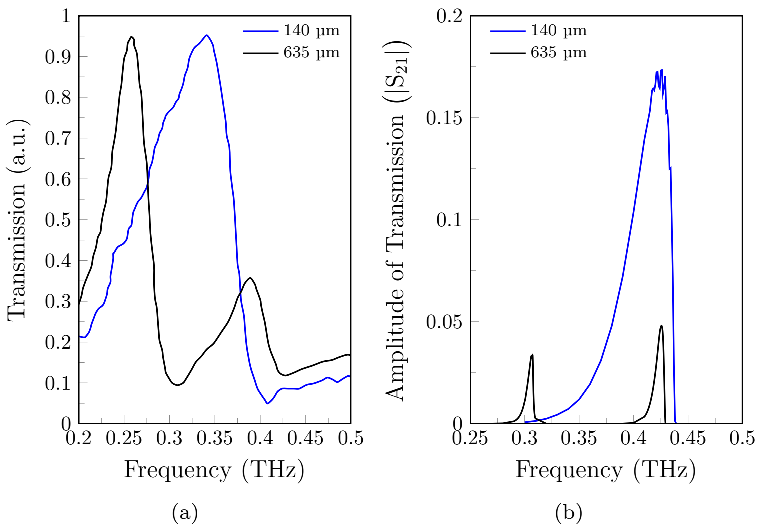

Figure 2.6: Transmission results for aluminum structure from: (a) experimental results in [41] and (b) FCB simulation results using HFSS™.

transmission is calculated by the linear summation of all the five $|S_{21}|$ values for the dominant port mode. Since the maximum simulation frequency is only 0.45 THz, the results obtained with FCB (using the classical skin-effect model) are almost identical to those obtained with the LIB (using the classical relaxation-effect model). However, this may not be the case when the dominant mode is at significantly higher frequencies. However, with EMPro there is a notable difference in the predicted transmission heights and levels of detuning.

This section has highlighted the need for multiple-mode excitation, even if only the results for the dominant mode are needed. If the computational burden is not significantly increased, more modes should be calculated at the output for each excited port mode to achieve more accurate results.

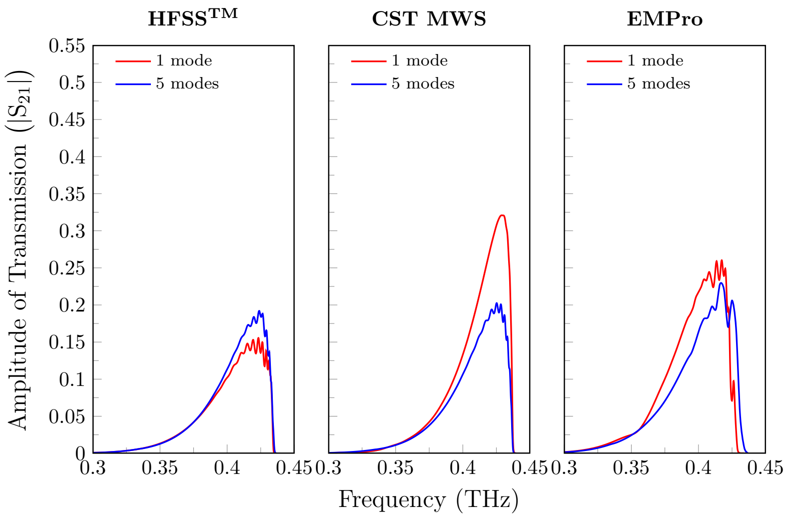

Figure 2.7: Simulated transmission results of gold spoof surface plasmon waveguides for the dominant mode. (Left: HFSS™, middle: CST MWS and right: EMPro).

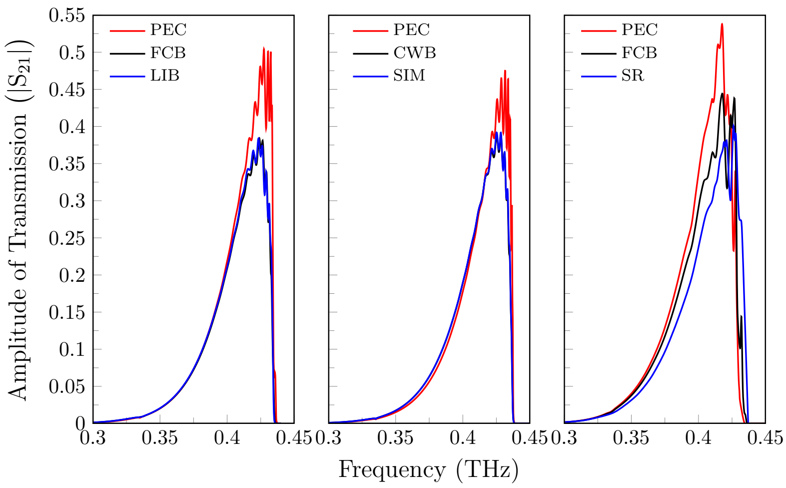

Figure 2.8: Simulated transmission results for the spoof surface plasmon waveguide with 5 modes excited at the ports. (Left: HFSS™, middle: CST MWS and right: EMPro).

2.6 Discussion

It has been shown that finding the correct modelling strategy is not always straightforward, when employing even well-known commercial EM solvers, for modelling metal-based THz structures. It is important to understand how the software code runs in the background and what input data it expects the user to enter. For example, in the HFSS™ Technical Notes (version 13) it is stated that permittivity can be complex and the effective permittivity can is formulated as:

$$\varepsilon_{\text{eff}} = \varepsilon_0 \boldsymbol{\varepsilon}_{\mathbf{r}} \left(1 - j \tan \boldsymbol{\delta} - j \frac{\boldsymbol{\sigma}}{\omega \varepsilon_0 \boldsymbol{\varepsilon}_{\mathbf{r}}} \right) \tag{2.34}$$

In order to avoid introducing further confusion, in this section, parameters in bold font correspond to input parameters in HFSS™ (rather than vectors, found in previous sections).

Now, it is not unambiguously stated that all input parameters must be real numbers, including relative permittivity $\boldsymbol{\varepsilon_{\mathrm{r}}}$ and bulk conductivity $\boldsymbol{\sigma}$, in order for the code to calculate $\varepsilon_{\mathrm{eff}}$, which is the only parameter needed by the solver. Unlike CST MWS, HFSS™ does not check for invalid input arguments (i.e., complex-valued parameters) and so no errors or warnings appear during setup or simulations. This can leave the user with a false sense of security, after the final results are reported by HFSS™. As can be seen in (2.34), the three input parameters are the relative permittivity $\boldsymbol{\varepsilon_{\mathrm{r}}}$, the dielectric loss tangent $\boldsymbol{\tan\delta}$ and the bulk conductivity $\boldsymbol{\sigma}$.

For the general case, where both the intrinsic relative permittivity and intrinsic bulk conductivity are represented by complex numbers (i.e., $\varepsilon(\omega) = \varepsilon'(\omega) - j\varepsilon''(\omega)$ and $\sigma(\omega) = \sigma'(\omega) - j\sigma''(\omega)$, respectively), the HFSS™ parameters that should be entered so that (2.34) is consistent with (2.12) are $\boldsymbol{\varepsilon_{\mathrm{r}}} \to \varepsilon'_{\mathrm{r,eff}}(\omega)$, $\boldsymbol{\tan\delta} \to \dfrac{\varepsilon''_{\mathrm{eff}}(\omega)}{\varepsilon'_{\mathrm{eff}}(\omega)}$ and $\boldsymbol{\sigma} \to 0$, resulting in $\varepsilon_{\mathrm{eff}} = \varepsilon_0\varepsilon'_{\mathrm{r,eff}}\left(1 - j\dfrac{\varepsilon''_{\mathrm{eff}}}{\varepsilon'_{\mathrm{eff}}}\right)$. However, because $\boldsymbol{\sigma} \to 0$, the "solve inside" function is automatically enabled. Therefore, this approach is impractical for metals, due to the excessive computational resources and processing time needed for the very high mesh densities associated with this function.

Alternatively, for the metal-like case, where a material is described by a real-valued intrinsic permittivity and complex-valued intrinsic bulk conductivity (e.g., metals with $\varepsilon_{\mathrm{r}} \cong 1$ and $\sigma(\omega) = \sigma'(\omega) - j\sigma''(\omega)$) the parameters $\boldsymbol{\varepsilon_{\mathrm{r}}} \to \varepsilon'_{\mathrm{r,eff}}(\omega)$, $\boldsymbol{\tan\delta} \to 0$ and $\boldsymbol{\sigma} \to \sigma'(\omega)$ yield the correct results and (2.34) gives $\varepsilon_{\mathrm{eff}}(\omega) = \varepsilon_0\varepsilon'_{\mathrm{r,eff}}(\omega)\left(1 - j\dfrac{\sigma'(\omega)}{\omega\varepsilon_0\varepsilon'_{\mathrm{r,eff}}(\omega)}\right)$. An example of this approach was used to simulate plasma-walled MPRWGs [43].

Similarly, for the dielectric-like case, where a material is described by complex-valued intrinsic permittivity and real-valued intrinsic bulk conductivity (e.g., dielectrics with $\varepsilon(\omega) = \varepsilon'(\omega) - j\varepsilon''(\omega)$ and $\sigma(\omega) = \sigma'(\omega)$) the HFSS™ parameters $\boldsymbol{\varepsilon_{\mathrm{r}}} \to \varepsilon'_{\mathrm{r}}(\omega)$, $\boldsymbol{\tan\delta} \to \dfrac{\varepsilon''(\omega)}{\varepsilon'(\omega)}$ and $\boldsymbol{\sigma} \to \sigma'(\omega)$ yield $\varepsilon_{\mathrm{eff}}(\omega) = \varepsilon_0\varepsilon'_{\mathrm{r}}\left(1 - j\dfrac{\varepsilon''(\omega)}{\varepsilon'(\omega)} - j\dfrac{\sigma_0}{\omega\varepsilon_0\varepsilon'_{\mathrm{r}}(\omega)}\right)$. This is a valid approach, but only for the simple relaxation-effect and classical skin-effect models.

These three scenarios are summarized in Table 2.2. The important message to note is that loose terminology leads to ambiguities and potentially significant errors. To the best of our knowledge, this is the first time that a clear and unambiguous description has been given for correctly entering material parameters for HFSS™.

For metal-based THz structures, instead of using solid metal objects, boundaries can be employed to avoid the problems related with the "solve inside" function. Macros can be used by writing a Visual Basic Script (VBScript) to define various dispersion models for materials that can then be employed in a "solid object" or boundary. For example, the VBScript suggested by Ansys [36] calculates the material parameters based on Drude's classical relaxation-effect model, by entering the intrinsic bulk dc conductivity σ_0 and the phenomenological scattering relaxation time τ. As with the general case, the calculated material parameters $\left(\boldsymbol{\varepsilon_{\mathrm{r}}} \to \varepsilon'_{\mathrm{r,eff}}(\omega),\ \boldsymbol{\tan\delta} \to \dfrac{\varepsilon''_{\mathrm{eff}}(\omega)}{\varepsilon'_{\mathrm{eff}}(\omega)}\right)$ are then used as input parameters for (2.34). However, as explained previously, this general-case modelling approach requires $\boldsymbol{\sigma} \to 0$ and, thus, the material created by the VBScript cannot be used with the FCB, LIB or IB. As a result, the material can only be used to define "solid objects" with the "solve

Table 2.1: Summary of different modelling strategies for metal structures using HFSS™ and CST MWS

		HFSS™		CST MWS	
		Eigenmode Solver	**Other solvers**	**Eigenmode Solver**	**Other solvers**
Solid object definition	**Input parameters**	σ_0 or data file of $\sigma'(f)$		σ_0 or data file of $\varepsilon'_{\mathrm{r,eff}}(f)$ and $\varepsilon''_{\mathrm{r,eff}}(f)$	σ_0 or discrete points of $\sigma'(f)$ or ω_{p} and ω_τ
	Error	significant	negligible	significant	negligible/significant
	Model	(1) classical skin-effect (2) simple relaxation-effect (3) classical relaxation-effect[1]		(1) classical skin-effect (2) simple relaxation-effect (3) classical relaxation-effect	
	Comments	without "solve inside" function enabled		With (1), σ_0 is ignored and PEC is assumed. Post-processing is then required. With (2) and (3), impractical resources are required.	For (1) and (2) the error is negligible, for (3) the error is significant.
FCB (HFSS™) and **CWB** (CST MWS)	**Input parameters**	σ_0 or $\sigma'(f_{\mathrm{I}})$	σ_0 or data file of $\sigma'(f)$	σ_0	σ_0 or $\sigma'(f)$
	Error	negligible/small	negligible	negligible	negligible
	Model	(1) classical skin-effect (2) simple relaxation-effect			
	Comments	In general f_{I} is not known *a priori* so (2) is of limited use.		Input parameters are ignored, lossy metals are considered as PEC and σ is entered at the post-processing stage.	Input parameters should be entered at each discrete frequency point.
LIB (HFSS™)	**Input parameters**	data file of $\varepsilon'_{\mathrm{r,eff}}(f)$ and $\sigma'(f)$	data file of $\varepsilon'_{\mathrm{r,eff}}(f)$ and $\sigma'(f)$		
	Error	negligible	negligible		
	Model	(1) classical skin-effect (2) simple relaxation-effect (3) classical relaxation-effect			
	Comments	In general, this is a two-run simulation.			
IB (HFSS™) and **SIM** (CST MWS)	**Input parameters**	$R_{\mathrm{s}}(f_{\mathrm{I}})$, $X_{\mathrm{s}}(f_{\mathrm{I}})$	$R_{\mathrm{s}}(f)$, $X_{\mathrm{s}}(f)$	Data file of $R_{\mathrm{s}}(f)$, $X_{\mathrm{s}}(f)$	
	Error	negligible	negligible	negligible	significant
	Model	(1) classical skin-effect (2) simple relaxation-effect (3) classical relaxation-effect		(1) classical skin-effect (2) simple relaxation-effect	(1) classical skin-effect (2) simple relaxation-effect (3) classical relaxation-effect
	Comments	In general f_{I} is not known *a priori* so (2) and (3) are of limited use.	Input parameters should be entered at each discrete frequency point.	Input parameters are ignored, lossy metals are considered as PEC and σ is entered at the post-processing stage.	

[1]If the "solve inside" function is disabled the results will not be correct. However, with the "solve inside" enabled and with the input parameters shown later the results should be correct, although this approach is impractical as explained in the Discussion section.

inside" function automatically enabled. Again, this approach does not give accurate results when metal-based structures are modelled, due to inadequate meshing inside the metal.

HFSS™ can generally give accurate results once the user has properly set up the simulation. Although this may seem trivial, the user has many more options (compared to the other software packages being investigated) to define materials but not all of them lead to correct solutions. However, HFSS™ is the only one (among the software packages) that has a full 3D eigenmode solver capable of producing accurate and meaningful results.

On the other hand, in CST MWS and RSoft, it is straightforward to define the material parameters; the software automatically blocks the parameter fields that conflict with one other. In addition, once the input parameters are entered, their validity is checked, with error messages appearing in the case of an unexpected input.

Table 2.2: Material input parameters for HFSS™

Material Type	Input Parameters		
	Relative permittivity ε_r	**Bulk Conductivity** σ	**Dielectric loss tangent** $\tan\delta$
General Case complex intrinsic permittivity complex intrinsic bulk conductivity	$\varepsilon'_{r,eff}(f)$	0	$\dfrac{\varepsilon''_{eff}(f)}{\varepsilon'_{eff}(f)}$
Metal-like Case real intrinsic permittivity complex intrinsic bulk conductivity	$\varepsilon'_{r,eff}(f)$	$\sigma'(f)$	0
Dielectric-like Case complex intrinsic permittivity real intrinsic bulk conductivity	$\varepsilon'_r(f)$	$\sigma'(f)$	$\dfrac{\varepsilon''(f)}{\varepsilon'(f)}$

2.7 Conclusion

For the first time, an exhaustive comparative study has been made to investigate the use of well-known commercial frequency domain solvers for the modelling of metal-based THz structures. Using the documentation provided by each of the four EM software package vendors, and in consultation with their technical support teams, various approaches to modelling benchmark metal-based THz structures have been studied. As suitable references, classical frequency dispersion models were applied to define material parameters. Since few measured results are available in the open literature for THz metal-pipe rectangular waveguides [22], or their associated cavities, only those for the spoof surface plasmon waveguide could be found using time-domain techniques for limited comparison [41].

While accurate verification measurements for this work are highly desirable, in practice it is believed that this very important task is not generally possible and so beyond the scope of this study. The reason for this is that traceable standards do not yet exist for frequency-domain metrology between 0.3 and 10 THz. Therefore, the corresponding measurement errors at such short wavelengths are likely to swamp those found in this numerical simulation study.

It has been found that the correct approach to selecting the most appropriate boundary conditions, defining a material's parameters and being able to enter its real or complex values within the software are not always straightforward. This chapter highlights intuitive and logical approaches that give incorrect results and, where possible, makes recommendations for the most appropriate solutions that have hitherto not been given in Technical Notes.

This work has highlighted important weaknesses in well-known commercial frequency-domain EM modelling software packages currently being used for THz simulations. While the use of time-domain solvers has been beyond the scope of this work, it is believed that similar challenges to obtaining accurate results will be found.

It is believed that this work gives, for the first time, a detailed comparative insight into the most appropriate use of commercial EM solvers for the numerical simulation of arbitrary metal-based THz structures. As a result, newcomers to the field of numerical EM simulators, as well as experienced designers, will be able to predict the performance of passive metal-based THz components with more confidence in the generated results.

Finally, the findings presented in this work could act as a benchmark for the comparison and development of existing and future numerical simulation software intended for THz applications. It is hoped that this study will encourage the development of more accurate frequency-domain solvers and help engineers and scientists design more accurate THz structures.

References

[1] H. Kazemi, S. T. Wootton, N. J. Cronin, S. R. Davies, R. E. Miles, R. D. Pollard, J. M. Chamberlain, D. P. Steenson and J. W. Bowen, "Active micromachined integrated terahertz circuits", *Int. J. Infrared Millim. Waves*, vol. 20, no. 5, pp. 967-974, Mar. 1999

[2] F. Maiwald, S. Martin, J. Bruston, A. Maestrini, T. Crawford and P. H. Siegel, "2.7 THz waveguide tripler using monolithic membrane diodes", *IEEE Int. Microw. Symp.*, vol. 3, pp. 1637-1640, May 2001

[3] J. W. Bowen, S. Hadjiloucas, B. M. Towlson, L. S. Karayzas, S. T. G. Wootton, N. J. Cronin, S. R. Davies, C. E. McIntosh, J. M. Chamberlain, R. E. Miles, and R. D. Pollard, "Micromachined waveguide antennas for 1.6 THz", *IET Electron. Lett.*, vol. 42, no. 15, pp. 842-843, Jul. 2006

[4] A. Pavolotsky, D. Meledin, C. Risacher, M. Pantaleev, and V. Belitsky, "Micromachining approach in fabricating of THz waveguide components", *Microelectr. J.*, vol. 36, pp. 683-686, Jun. 2005

[5] C. D. Nordquist, M. C. Wanke, A. M. Rowen, C. L. Arrington, M. Lee, and A. D. Grine, "Design, fabrication, and characterization of metal micromachined rectangular waveguides at 3 THz", *Int. Symp. Antennas Propag.*, pp. 1-4, Jul. 2008

[6] T. H. Hand, Y. Yuan, S. Palit, C. Bingham, M. Rahm, D. R. Smith, W. J. Padilla, N. Jokerst and S. A. Cummer, "Dual-band planar electric thz metamaterial with resonator yield analysis", *2008 Conf. Lasers Electro-Opt.*, pp. 1-2, May 2008

[7] N. Llombart and P. H. Siegel, "Cylindrically periodic dielectric waveguide at submillimeter waves", *Int. Symp. Antennas Propag.*, pp. 1-4, Jul. 2008

[8] W. Miao, Y. Delorme, F. Dauplay, G. Beaudin, Q. J. Yao and S. C. Shi, "Simulation of an integrated log-spiral antenna at terahertz", *Int. Symp. Antennas Propag. EM Theory*, pp. 58-61, Nov. 2008

[9] K. R. Jha, S. V. R. K. Rao and G. Singh, "Constructive interference in Yagi-Uda type printed terahertz antenna on photonic crystal substrate", *IEEE Sarnoff Symp.*, pp. 1-5, Apr. 2010

[10] M. Theuer, C. Imhof, G. Torosyan, F. Ellrich, R. Zengerle and R. Beigang, "Pump beam diameter dependent terahertz generation from surface emitters - experiment and simulation", *Int. Conf. Infrared Millim. Terahertz Waves*, pp.1-2, Sep. 2008

[11] K R. Jha and G. Singh, “Analysis of Dielectric Permittivity and Losses of Two-layer Substrate Materials for Microstrip Antenna at THz Frequency”, *Int. Conf. Advances Recent Technol. Commun. Comput.*, pp. 672-675, Oct. 2009

[12] C. J. Lin, C. H. Lin, Y. T. Li, R. P. Pan and C. L. Pan, “Electrically controlled liquid crystal phase grating for terahertz waves”, *IEEE Photon. Technol. Lett.*, vol. 21, no. 11, pp. 730-732, Jun. 2009

[13] F. Zhan, G. Qiaoqiang, Y.J. Ding and F.J. Bartoli, “From waveguiding to spatial localization of THz waves within a plasmonic metallic grating”, *IEEE J. Sel. Top. Quant. Electron.*, vol. 14, no. 2, pp. 486-490, Mar. 2008

[14] B. Y. Shew, H. C. Li, C. L. Pan and C. H. Ko, “X-ray micromachining SU-8 resist for a terahertz photonic filter”, *J. Phys. D: Appl. Phys.* vol. 38, no. 7, pp. 1097-1103, Mar. 2005

[15] G. Qiaoqiang and F. J. Bartoli, “Graded metallic gratings for ultrawideband surface wave trapping at THz frequencies”, *IEEE J. Sel. Top. Quant. Electron.*, vol. 17, no. 1, pp. 102-109, Jan. 2011

[16] D. Sanchez-Escuderos, M. Ferrando-Bataller, M. Baquero-Escudero and J. I. Herranz, “EBG structures for antenna design at THz frequencies”, *IEEE Int. Symp. Antennas Propag.*, pp. 1824-1827, Jul. 2011

[17] P. Peier, H. Merbold, V. Pahinin, K. A. Nelson and T. Feurer, “Imaging of THz waves in 2D photonic crystals structures embedded in a slab waveguide”, *New J. Phys.*, vol. 12, p. 013014, Jan. 2010

[18] E. Episkopou, S. Papantonis, W. J. Otter and S. Lucyszyn, “Demystifying material parameters for terahertz electromagnetic simulation”, *4th UK/Europe-China Conf. on Millim. Waves Terahertz Technol.*, pp. 80-81, Sep. 2011

[19] J. Y. Choi and S. Lucyszyn, “HFSS™ modelling anomalies with electrically thin-walled metal-pipe rectangular waveguide simulations”, *10th IEEE High Freq. Postgrad. Student Colloq.*, pp. 95-98, Sep. 2005

[20] Y. Zhou and S. Lucyszyn, “HFSS™ modelling anomalies with THz metal-pipe rectangular waveguide structures at room temperature”, *PIERS*, vol. 5, no. 3, pp. 201-211, 2009

[21] J. Hoffmann, C. Hafner, P. Leidenberger, J. Hesselbarth and S. Burger, “Comparison of electromagnetic field solvers for the 3D analysis of plasmonic nano antennas”, *Proc. SPIE* vol. 7390, 73901G, Feb. 2010

[22] S. Lucyszyn, “Investigation of anomalous room temperature conduction losses in normal metals at terahertz frequencies”, *IEE Proc. Microw. Antennas Propag.*, vol. 151, no. 4, pp. 321-329, Aug. 2004

[23] S. Lucyszyn, “Investigation of Wang’s model for room temperature conduction losses in normal metals at terahertz frequencies”, *IEEE Trans. Microw. Theory Techn.*, vol. 53, no. 4, pp. 1398-1403, Apr. 2005

[24] R. F. Harrington, “Time-harmonic electromagnetic fields”, *Wiley-IEEE Press*, 2001

[25] S. Lucyszyn and Y. Zhou, “Engineering approach to modelling frequency dispersion within normal metals at room temperature for THz applications”, *PIER*, vol. 101, pp. 257-275, Feb. 2010

[26] C. P. Smyth, “Dielectric behavior and structure: dielectric constant and loss, dipole moment, and molecular structure”, 1st ed., *McGraw-Hill*, 1955

[27] F. A Grant, “Use of complex conductivity in the representation of dielectric phenomena”, *J. Appl. Phys.*, vol. 29, no.1, pp. 76-80, Jan. 1958

[28] K. L. Ngai and R. W. Rendell, “Interpreting the real part of the dielectric permittivity contributed by mobile ions in ionically conducting materials”, *Phys. Rev. B*, vol. 61 no. 14, pp. 9393-9398, Apr. 2000

[29] T. W. Kim, W. P. Beyermann, D. Reagor and G. Gruner, “Complex conductivity measurements at several frequencies in the millimetre wave spectral range”, *Rev. Sci. Instrum.*, vol. 59, no. 7, Jul. 1988

[30] U. Kaatze, “Complex permittivity of water as a function of frequency and temperature”, *J. Chem. Eng. Data*, vol. 34, no. 4, pp. 371-374, Oct. 1989

[31] S. Lucyszyn, “Microwave characterization of nickel”, *PIERS*, vol. 4, no. 6, pp. 686-690, Jun. 2008

[32] S. Lucyszyn and Y. Zhou, “THz applications for the engineering approach to modelling frequency dispersion within normal metals at room temperature”, *PIERS*, vol. 6, no. 3, pp. 293- 299, Feb. 2010

[33] ISO 497:1973, “Guide to the choice of series of preferred numbers and of series containing more rounded values of preferred numbers”, 1973, http://www.iso.org/iso/iso_catalogue/catalogue_tc/catalogue_detail.htm ?csnumber=4548

[34] R. E. Collin, “Field theory of guide waves”, 1st ed., *Wiley-IEEE Press*, 1991

[35] S. Lucyszyn, D. Budimir, Q. H. Wang, and I. D. Robertson, “Design of compact monolithic dielectric-filled metal-pipe rectangular waveguides for millimetre-wave applications”, *IEE Proc. Microw. Antennas Propag.*, vol. 143, no. 5, pp. 451-453, Oct. 1996

[36] D. Edgar, Ansys Corporation, *Private Communication*, Nov. 2010

[37] J. C. Slater, “Microwave electronics”, *Rev. Mod. Phys.*, vol. 18, no. 4, pp. 441-512, Oct. 1946

[38] Z. Yu, G. Veronis, S. Fan, and M. L. Brongersma, "Design of midinfrared photodetectors enhanced by surface plasmons on grating structures", *Appl. Phys. Lett.*, vol. 89, no. 15, Oct. 2006

[39] B. K. Juluri, S. C. Lin, T. R. Walker, L. Jensen, and T. J. Huang, "Propagation of designer surface plasmons in structured conductor surfaces with parabolic gradient index", *Opt. Express*, no. 17, pp. 2997-3006, Feb. 2009

[40] S. A. Maier, S. R. Andrews, L. Martin-Moreno, and F. J. Garcia-Vidal, "Terahertz surface plasmon-polariton propagation and focusing on periodically corrugated metal wires", *Phys. Rev. Lett.*, vol. 97, p. 176805, Oct. 2006

[41] G. Kumar, S. Pandey, A. Cui and A. Nahata, "Planar plasmonic terahertz waveguides based on periodically corrugated metal films", *New J. Phys.*, vol. 13, p. 033024, Mar. 2011

[42] M. Rütschlin, CST, *Private Communication*, Mar. 2012

[43] Y. Zhou and S. Lucyszyn, "Modelling of reconfigurable terahertz integrated architecture (RETINA) SIW structures", *PIER*, vol. 105, pp. 71-92, Jun. 2010

Chapter 3

Microwave Discharge Plasma Switch

In this chapter a proof-of-concept demonstrator of a microwave discharge plasma switch is studied in the frequency region from 1 GHz to 2 GHz. The scope of this preliminary experiment is to investigate the interaction between the plasma developed inside the tube and the incoming microwave signal, with the aim to obtain a qualitative description of the device behaviour. In this experiment, a gas discharge plasma tube is vertically inserted across an in house manufactued WR-650 rectangular waveguide ($a \times b = 165 \times 82.5$ mm^2) section. When the discharge tube is on, the ionised gas inside the tube acts as a highly conductive plasma column and hence the input microwave power is reflected and dissipated from the discharge tube. The performance of the prototype is studied through numerical modelling and measurements of the power loss characteristics.

3.1 Introduction

With plasma physics providing a wide range of applications in different fields, it has received considerable interest over the last decades. Particularly, the interaction of plasma with electromagnetic waves is well studied and the use of plasma tubes for the development of plasma structures, such as plasma antennas, switches and attenuators with potential applications in radar systems has been proposed [1–7]. In these works, plasma is either created from plasma sources built especially for the needs of the specific system or from commercially-available plasma tubes, such as fluorescent tubes [8–11]. In the latter case, experimental setup is simple and inexpensive to build and thus can be used as a proof-of-concept prototype.

As already shown [1–3, 5, 7], plasma columns and particularly, fluorescent tubes can effectively replace the metal parts of certain devices (e.g. plasma antennas). It is well known that fluorescent tubes consist of a glass tube filled with a gas (in this case argon) with the inner tube surface coated with phosphorus [1]. At both ends of the tube an electrode is fixed which acts as a cathode. When an AC voltage is applied across the tube's cathodes, the electrodes are heated, with current passing through them, and thus electrons are emitted. Due to collisions between the free electrons and the gas atoms, ultraviolet (UV) light is generated. The fluorescent coating at the inner surface of the tube is then excited by the UV radiation and thus the UV light is converted into visible light. Therefore, when the lamp is on, a plasma column (with high electron density and hence high conductivity) is formed

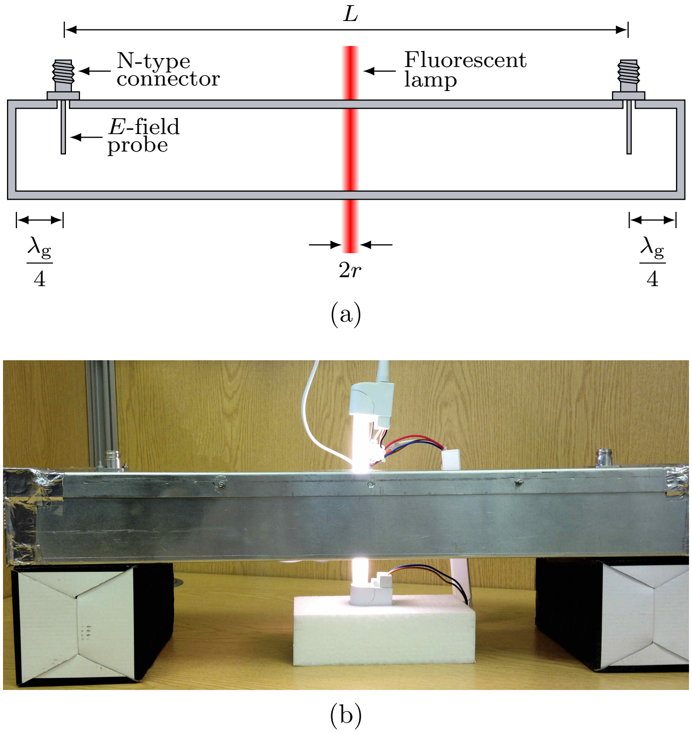

Figure 3.1: (a) Illustration of the experimental setup showing the waveguide section and the fluorescent tube when the lamp is ON. (b) Manufactured prototype.

due to the ionisation of the gas inside the lamp. In this chapter, we will study the effect of such plasma columns on the performance of a WR-650 rectangular waveguide section. This is a proof-of-concept demonstration in order to obtain a qualitative study of the general concept which is then applied into a more sophisticated manner, at terahertz frequencies.

3.2 Plasma Switch Prototype

The experimental setup consists of a WR-650 metal pipe rectangular waveguide with internal spatial dimensions of $a \times b = 165 \times 82.5$ mm^2, having both ends short circuited. The waveguide is manufactured from two aluminium sheets with thickness of 1.5 mm, one of them forming the bottom wall and the two sidewalls of the waveguide, and the second one forming the top wall. The metal pieces are then bolted together and shielded with aluminium tape at the edges. The microwave energy is coupled into the waveguide through two N-type coaxial electric field probes, which are located at a distance of $\frac{\lambda_g}{4}$ from the short circuited ends. At this distance from the short-circuited ends a maximum value of the electric field E occurs and hence more efficient coupling between the electric field and the probes is obtained. In general, the guided wavelength for an air-filled rectangular waveguide is related with the free space wavelength $\lambda_0 = 2\pi c/\omega$ with the textbook expression [12]

$$\lambda_g = \frac{\lambda_0}{\sqrt{1 - \left(\frac{\lambda_0}{\lambda_c}\right)^2}} \tag{3.1}$$

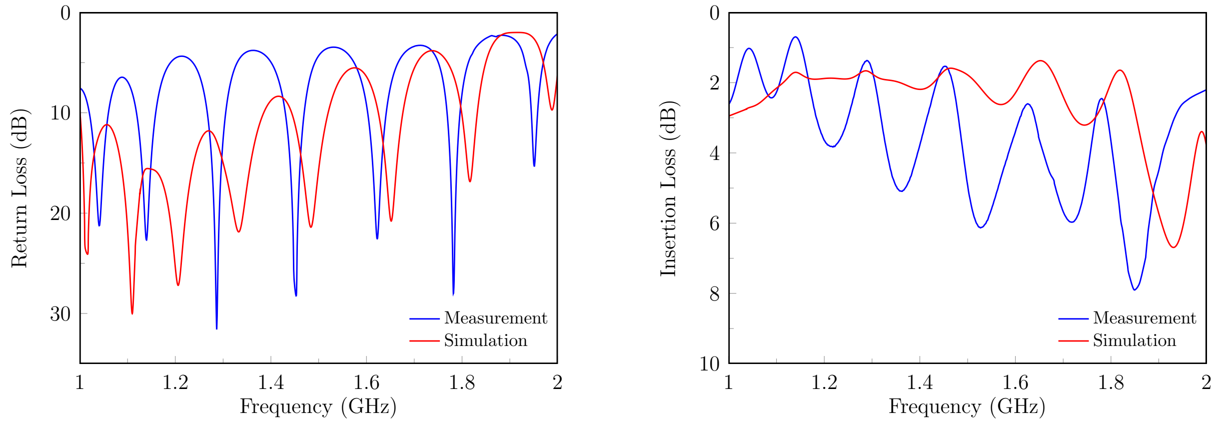

(a) (b)

Figure 3.2: Measured and simulated results of (a) the return loss and (b) the insertion loss in the case that the fluorescent tube is OFF.

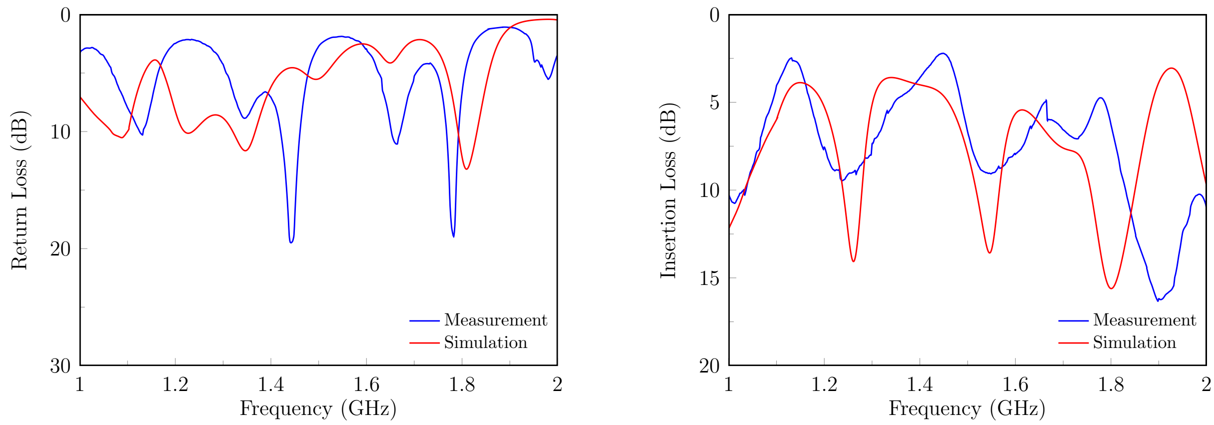

(a) (b)

Figure 3.3: Measured and simulated results of (a) the return loss and (b) the insertion loss when the lamp is ON.

where the cut-off wavelength λ_c for a TE_{mn} propagating mode is defined as [12]:

$$\lambda_c = \frac{2\pi}{k_c} = \frac{2\pi}{\sqrt{k^2 - \beta^2}} = \frac{2\pi}{\sqrt{\left(\frac{m\pi}{a}\right)^2 + \left(\frac{n\pi}{b}\right)^2}} \tag{3.2}$$

From the above expressions the guided wavelength for the dominant TE_{10} mode in a WR-650 rectangular waveguide at 1.5 GHz is equal to $\lambda_g = 250$ mm.

The plasma tube used in this experiment is a fluorescent tube with diameter $2r = 2$ cm, placed across the waveguide, through two circular holes at the center of the waveguide's broad walls. The holes' diameter is approximately the same as the diameter of the tube and with their size significantly smaller than the guided wavelength the power loss due to the holes can be assumed to be negligible.

The transmission and reflection characteristics are studied both numerically and experimentally. The modelling of the device is done in CST Microwave Studio while the measured

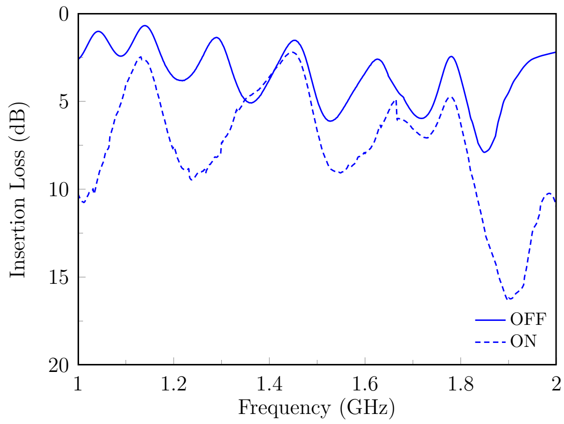

Figure 3.4: Comparison of the measured results for the insertion loss when the fluorescent lamp is OFF and ON.

S-parameters, are obtained through calibrated measurements using a vector network analyser. A Short/Open/Load/Through (SOLT) calibration was performed with the calibration reference plane being at the N-type connectors. In this experimental setup (Fig. 3.1), an AC voltage of 230V (mains current) is applied to the fluorescent tube through a commercially available electronic ballast, which is essential in order to start the lamp and regulate the current through the lamp.

For the modelling of the fluorescent plasma source it has been assumed a uniform electron density of $1.5 \cdot 10^{11}$ cm^{-3} inside the tube, based on previous experimental measurements of the electron density for a fluorescent plasma lamp [13]. Also, instead of assuming the ideal case with alluminium walls with no manufacturing imperfections, a more realistic modelling approach has been used where defects are introduced at the joint between the top and bottom part of the waveguide. A comparison of the measured and simulation results are shown in Fig. 3.2 and Fig. 3.3 when the lamp is OFF and ON respectively. As can be seen, there is some discrepancy between the experimental and simulation results, which can be attributed to manufacturing tolerances and specifically to air gaps at the joint between the top wall and sidewalls of the waveguide. This is also confirmed by simulation results obtained when an airgap is introduced at the sidewalls of the waveguide. The results show an increase of the insertion loss with increasing airgap. Although, an attempt to include this effect is made by introducing a uniform airgap at the sidewalls, in practice, the two parts of the waveguide are bolted together and thus non-uniform air gaps are created in between. Furthermore, the plasma lamp characteristics have been modelled with the assumption of a uniform carrier density along the plasma tube and based on measurement results from literature. Hence, in the full-wave modelling only a rough approximation of the plasma characteristics is included.

Fig. 3.4. shows a comparison of the experimental results for the insertion loss, with and without current flowing in the plasma tube. It can be noticed that there is a drop in the insertion loss across the frequency band, giving an average drop of approximately 3 dB.

Moreover, modelling of the device with an array of plasma tubes placed inside the waveguide has been conducted. In this case a more profound impact on the device performance is noticed and particularly, for an array of three and four fluorescent tubes, with diameter $2r = 20$ mm and distance between adjacent lamps equal to $\lambda_g/4$ at 1.5 GHz, an average ON-OFF switching ratio of approximately 4 dB and 6.5 dB, respectively is achieved. This

Table 3.1: Average values of the simulated reflection and insertion loss for different number of lamps.

	1 Lamp	2 Lamps	3 Lamps	4 Lamps
Average S_{11} (dB)	-4.8	-5.2	-4.2	-4
Average S_{21} (dB)	-5.9	-6.5	-7.7	-11.2
Average ON-OFF ratio (dB)	2.8	3.3	4.1	6.5

effect is a result of the ionised gas inside the tube, which can be considered conductive when the plasma frequency is larger than the frequency of the incoming microwave signal. These results are summarised in Table 3.1

3.3 Conclusion

In this chapter a qualitative study of a microwave plasma switch is presented. With the aim of using this preliminary experiment as a proof-of-concept demonstrator, an inexpensive experimental setup was built consisting of an in-house manufactured aluminium waveguide and a commercially-available fluorescent tube. Although there are some discrepancies between the measured and simulation results obtained, which are mainly due to manufacturing tolerances and the simplified model for the plasma characteristics, the general concept of controlling the microwave propagation with the use of a plasma column is demonstrated. In the following chapters this concept will be applied in more complicated systems at THz frequencies for the development of reconfigurable waveguide components, with the plasma column being replaced by a photoconductive semiconductor material inside a miniaturised waveguide.

References

[1] V. Kumar, M. Mishra and N. K. Joshi, "Study of a fluorescent tube as plasma antenna", *PIER Lett.*, vol. 24, pp. 17-26, May 2011

[2] H. M. Zali, M. T. Ali, N. A. Halili, H. Jaafar and I. Pasya "Study of monopole plasma antenna using fluorescent tube in wireless transmission experiments", *Int. Symp. Telecom. Technol.*, pp. 52-55, Nov. 2012

[3] A. Ffield and R. Wolfson "Microwave measurements of a fluorescent lamp plasma", *Am. J. Phys.*, vol. 55, no. 7, pp. 637-641, Jul. 1987

[4] G. G. Borg, J. H. Harris, N. M. Martin, D. Thorncraft, R. Milliken, D.G. Miljak, B. Kwan, T. Ng and J. Kircher, "Plasmas as antennas: Theory, experiment and applications", *Phys. Plasmas*, vol. 7, no. 5, May 2000

[5] Z. Dai, S. Liu, Y. Chen and N. Gao, "Development and investigation of reconfigurable plasma antennas", *Microw. Millim. Wave Technol.*, pp. 1135-1137, May 2010

[6] I. Alexeff, T. Anderson, S. Parameswaran, E. P. Pradeep, J. Hulloli and P. Hulloli, "Experimental and theoretical results with plasma antennas", *IEEE Trans. Plasma Sci.*, vol. 34, no. 2, pp. 166-172, Apr. 2006

[7] V. Kumar, M. Mishra and N. K. Joshi, "Study of fluorescent tube as plasma antenna", *PIER Lett.*, vol. 24, pp. 17-26, May 2011

[8] R. Kumar, "Controlling of microwave propagation in metallic photonic crystal using plasma column", *Appl. Electrom. Conf.*, pp. 1-4, Dec. 2009

[9] H. Conrads and M. Schmidt, "Plasma generation and plasma sources", *Plasma Sources Sci. Technol.*, vol. 9, no. 4, pp. 441-454, Nov. 2000

[10] J. Orr and R. Wolfson, "Cyclotron resonance effects in a fluorescent lamp plasma", *Am. J. Phys.*, vol. 58, no. 10, pp. 968-973, Oct. 1990

[11] X. He, J. P. Chen, Y. Wu, Y. D. Chen, X. J. Zeng, H. C. Quin and X. W. Ni, "Microwave Diagnostics for studies of electromagnetic scattering by fluorescent lamp plasma", *J. Microw. Sci. Instr.*, vol. 1, no. 1, pp. 54-57, Mar. 2010

[12] C. A. Balanis, "Advanced engineering electromagnetics", *Wiley*, 1989

[13] M. K. Howlader, Y. Yang, and J. R. Roth "Time-resolved measurements of electron number density and collision frequency for a fluorescent lamp plasma using microwave diagnostics", *IEEE Trans. Plasma Sci.*, vol. 33, no. 3, pp. 1093-1099, Jun. 2005

Chapter 4

Analysis and Design of a Novel THz Waveguide Plasma Switch

In this chapter a novel design of a real-time tunable optically-controlled THz plasma switch with high ON-OFF ratio is presented. The device consists of a metal-pipe rectangular waveguide (MPRWG) partially filled with high resistivity silicon (HRS). The switch operates from 0.325 THz to 0.5 THz and is excited by a continuous wave (CW) laser source, thus photo-induced conductive regions are created within the HRS emulating plasma behaviour. The photoconductivity profile inside the HRS slab is described in detail and the performance of the switch is studied using an industry standard electromagnetic modelling software package, CST Microwave Studio. Various parametric studies are undertaken in order to evaluate its performance. Furthermore, in order to provide deeper insight in the behaviour of the device, a modal analysis is presented and its thermal characteristics are discussed.

4.1 Introduction

The last two decades there has been increasing commercial interest in the terahertz frequency range. Very recently, the latest generation of Vector Network Analyser (VNA) waveguide systems operating up to 1.1 THz was introduced, highlighting the need for THz waveguide components at these frequencies. However, with the majority of the components forming permanent structures, they suffer from poor reconfigurability. An efficient way to deal with the above problem is the use of the photoconductivity effect. As explained in more detail in Chapter 1, this optoelectronic approach has been widely used for the development of optically-controlled microwave and millimeter-wave devices and shows a big potential for THz applications as well.

This chapter presents a thorough study of a THz optically-controlled waveguide plasma switch. The structure is excited by a continuous wave (CW) laser source, thus photoexcited free carriers are generated inside the HRS slab creating highly conducting plasma regions. The characterisation of the plasma regions inside the HRS slab is first undertaken with the results used as an input to the full-wave electromagnetic modelling of the device. Also, a parametric study is presented in order to investigate how the different parameters affect the device performance, and optimise the design. A modal analysis describing the supported modes in the partially filled waveguide is also given. Finally, an investigation on the thermal behaviour of the structure is presented.

4.2 Switch Analysis and Design

4.2.1 Photo-induced Plasma Characterisation

The electrical dark conductivity of a semiconductor is directly related to the mobility μ_{e}, μ_{h} of the charge carriers (electron and holes) and carrier density n_0, p_0 and can be calculated as [1–3]

$$\sigma_{\mathrm{d}} = e\big(n_0\mu_{\mathrm{e}} + p_0\mu_{\mathrm{h}}\big) \tag{4.1}$$

By illuminating a semiconductor material with a laser beam, additional charge carriers are generated in the semiconductor material. The resulting increase in the free carrier density $n' = p' = N$ yields an increase $Ne\big(\mu_{\mathrm{e}} + \mu_{\mathrm{h}}\big)$ in the electrical conductivity –which is well-known as photoconductivity– and therefore the total conductivity is

$$\sigma_0 = \sigma_{\mathrm{d}} + Ne\big(\mu_{\mathrm{e}} + \mu_{\mathrm{h}}\big) \tag{4.2}$$

However, for a high resistivity semiconductor material (i.e., HRS) it can be assumed that its dark electrical conductivity is negligible ($\sigma_{\mathrm{d}} \simeq 0$), thus the total electrical conductivity is equal to the photoconductivity caused by the incident electromagnetic radiation

$$\sigma_0 = Ne\big(\mu_{\mathrm{e}} + \mu_{\mathrm{h}}\big) \tag{4.3}$$

Considering for simplicity an average effective mass for both electrons and holes $\widetilde{m}^* = (m^*_{\mathrm{e}} + m^*_{\mathrm{h}})/2$, the carrier scattering relaxation time $\tau \simeq [\widetilde{m}^*(\mu_{\mathrm{e}} + \mu_{\mathrm{h}})]/e$ and thus, (4.3) gives

$$\sigma_0 = \frac{Ne^2\tau}{\widetilde{m}^*} \tag{4.4}$$

Using the Drude model from (2.20) the frequency-dependent complex conductivity due to photo-induced carriers is

$$\sigma(\omega) = \sigma'(\omega) - j\sigma''(\omega) = \frac{\sigma_0}{1 + j\omega\tau} \tag{4.5}$$

where $\sigma'(\omega) = \dfrac{\sigma_0}{1+\omega^2\tau^2}$ and $\sigma''(\omega) = \dfrac{\sigma_0\omega\tau}{1+\omega^2\tau^2}$. Thus, from (2.13) the effective relative permittivity is given by

$$\varepsilon_{\mathrm{r,eff}}(\omega) = \varepsilon'_{\mathrm{r,eff}}(\omega) - j\varepsilon''_{\mathrm{r,eff}}(\omega) \tag{4.6}$$

where $\varepsilon'_{\mathrm{r,eff}}(\omega) = \varepsilon_{\mathrm{r}} - \dfrac{\omega_{\mathrm{p}}^2}{\omega^2 + \omega_\tau^2}$ and $\varepsilon''_{\mathrm{r,eff}}(\omega) = \dfrac{\omega_\tau}{\omega}\dfrac{\omega_{\mathrm{p}}^2}{\omega^2 + \omega_\tau^2}$, with $\omega_{\mathrm{p}} = \sqrt{Ne^2/\varepsilon_0\widetilde{m}^*}$ and $\omega_\tau = 1/\tau$ being the angular plasma frequency and angular scattering relaxation frequency, respectively.

Now, assuming a CW optical source the horizontal and vertical profiles of the photo-induced conductivity can be expressed by (1.24) and (1.34). The increase in the carrier density (due to the optical source) is calculated using Taurus Medici TCAD [4]. The optical illumination power density is assumed to be 40 W/cm^2, the wavelength of the laser source is $\lambda = 970$ nm, corresponding to the laser wavelength used in the experimental setup, and the beam width of uniform illumination is assumed to be 50 µm. A power density of this value has been chosen since it corresponds to a relatively low incident power (1.5 mW) and thus there is no requirement for a high power laser source. Moreover, using a laser illumination of

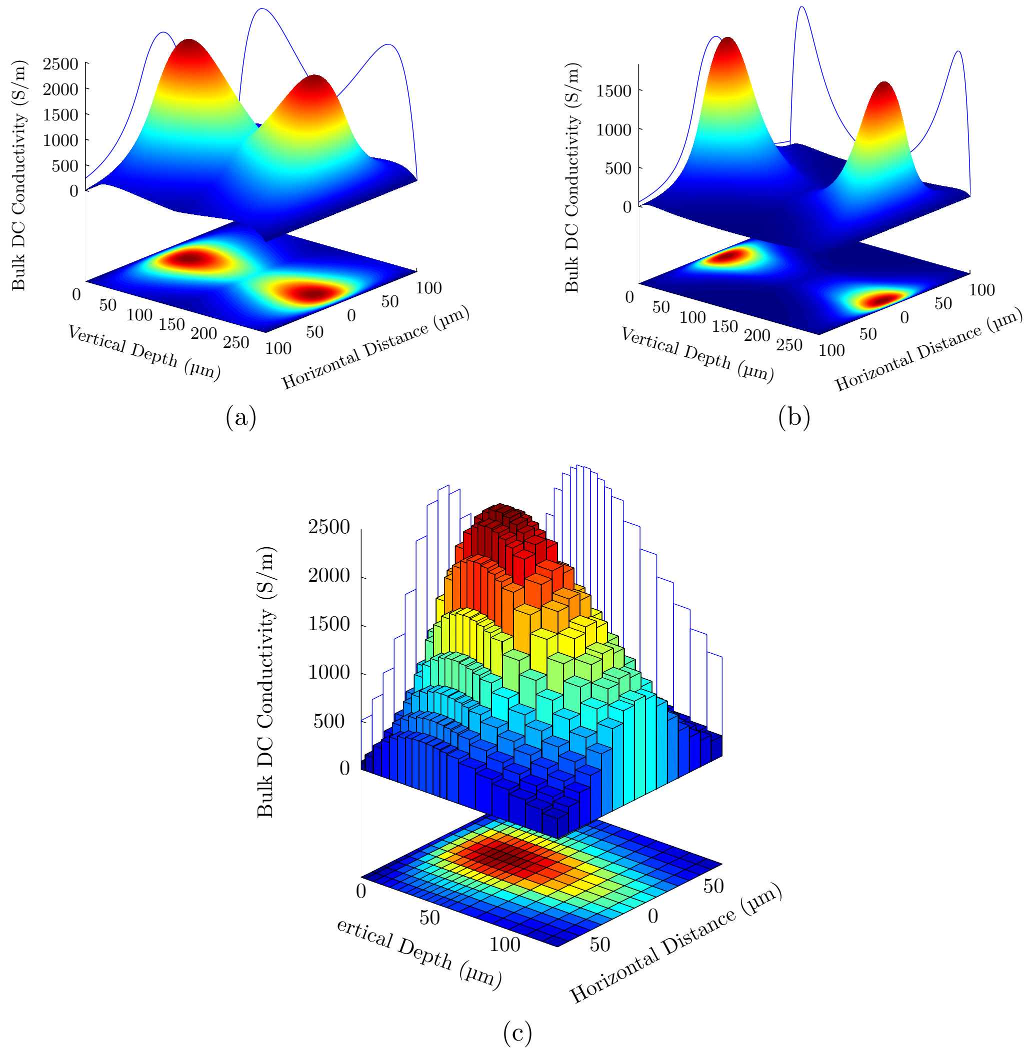

Figure 4.1: Bulk DC photoconductivity for double-sided laser illumination with (a) λ = 970 nm and (b) λ = 808 nm. (c) Discretised regions with λ = 970 nm. The horizontal distance corresponds to the x-direction and the vertical depth to the y-direction.

this power density prevents significant temperature rise, as will be explained in more detail in Section 4.4. The distribution of the DC photoconductivity within a 280 μm thick high resistivity silicon (HRS) substrate when illuminated from both sides, is shown in Fig. 4.1. As can be seen the maximum occurs at the beam center and at a depth of 50 μm. As a comparison, the photoconductivity distribution of a 808 nm laser source, which is commonly used for CW-mode optically-controlled structures [3], is also shown in Fig. 4.1(b). As can be seen, the maximum is located closer to the substrate surface, at a depth of 20 μm and decreases steeply thereafter. Hence, using a laser source of 970 nm provides larger regions of high carrier density inside the HRS slab. This is required with thicker substrates (here 280 μm) in order to achieve larger light penetration depth and thus avoid low conductivity regions at the center of the substrate. Using the numerical simulation results of the photo-induced carrier density and taking into account the Drude model for the conductivity, the vertical and horizontal distribution of the real part of the photoconductivity is calculated

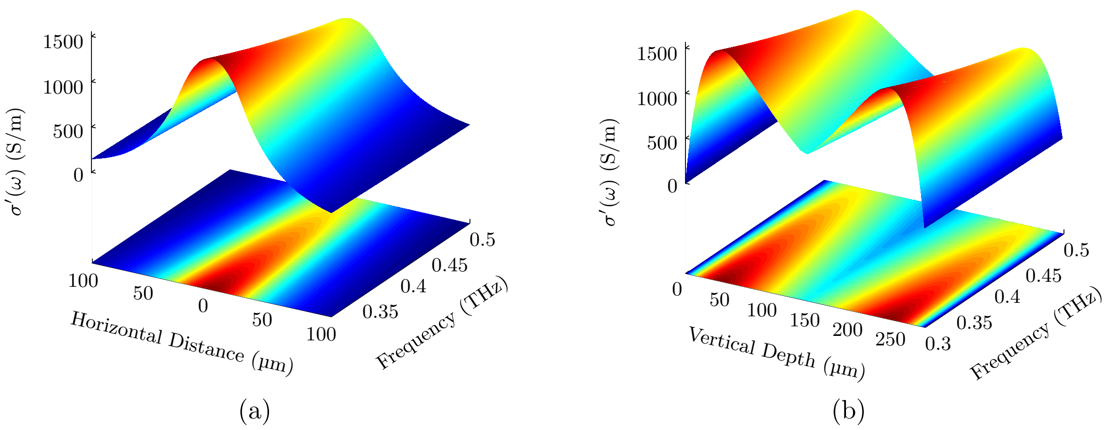

Figure 4.2: Real part of photoconductivity for λ = 970 nm as a function of frequency (a) along the horizontal direction at a vertical depth of y = 50 µm and (b) along the vertical direction at $x = 0$.

in the frequency range between 0.3 THz to 0.5 THz, (covering the operation frequency band of the optoelectronic switch) as shown in Fig. 4.2. The photoconductivity values plotted in Fig. 4.2(a) correspond to a vertical depth of 50 µm and the values plotted in Fig. 4.2(b) correspond to the illumination beam center at $x = 0$, where the photoconductivity peaks as shown in Fig. 4.1(a). As can be seen both profiles decrease with increasing frequency as expected, since the conductivity given by (4.5) is inversely proportional to the frequency.

4.2.2 Switch Design

The basic structure of the switch consists of a metal pipe rectangular waveguide (MPRWG) with internal spatial dimensions $a \times b$ = 560 × 280 µm² (i.e., WR-2.2 standard [6]) as shown in Fig. 4.3. A rectangular high resistivity silicon (HRS) slab with width d = 150 µm, height b = 280 µm and 1.16 mm long linear tapered ends is centered in the cross-section of the waveguide and placed in parallel to the side walls of the waveguide. The taper angle and the corresponding length of the tapered ends have been chosen to provide good impedance matching between the dielectric-filled and air-filled regions of the waveguide, as will discussed later in greater detail [8–12]. Here, the intrinsic resistivity of silicon is 10 kΩ · cm while its dielectric constant ε_r = 11.655 and loss tangent $\tan\delta$ = 0.0004, respectively, at 0.45 THz [7]. The HRS is illuminated with four spots of diameter $2r$ = 50 µm, through aligned circular apertures within the top and bottom broad walls of the MPRWG. The center-to-center distance between the adjacent apertures is 300 µm. The optical illumination power density is 40 W/cm², the optical wavelength is 970 nm and the beam width of uniform illumination is 50 µm.

The TCAD simulation results for the photoconductivity distribution within a HRS substrate, presented in the previous section, as well as the detailed analysis in Chapter 1, suggest, that the induced photoconductivity is inhomogeneous. Therefore, in order to accurately model the interaction between the plasma and the incoming THz wave, discretisation of the photoconductivity values is required for the full-wave simulation software (CST Microwave Studio [5]). To this end, in order to obtain an accurate plasma characterisation

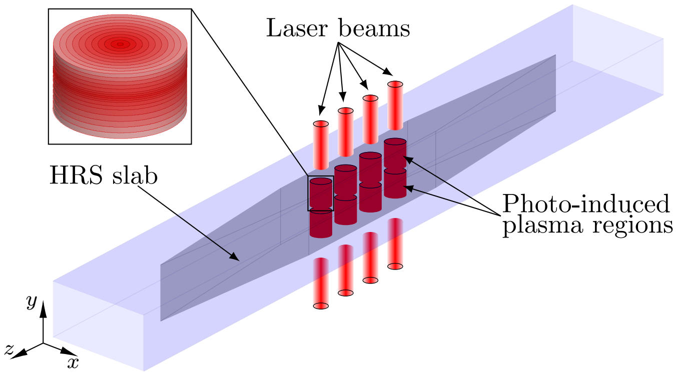

Figure 4.3: Perspective view of the THz optically-controlled switch with double-sided illumination. The switch consists of an air-filled metal rectangular waveguide partially-filled with high resistivity silicon illuminated through circular apertures on the broad metal walls.

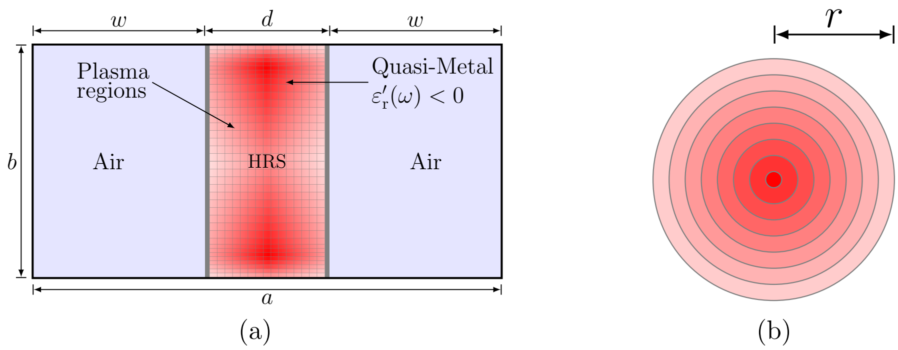

Figure 4.4: (a) Cross sectional illustration of the structure depicted in Fig. 4.3 with double-sided illumination and (b) top view of the photo-induced regions.

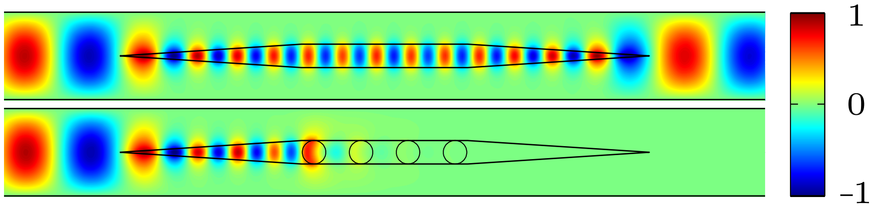

Figure 4.5: Normalized electric field pattern at 0.45 THz. Top: Without laser illumination and bottom: with double-sided laser illumination.

while keeping the total simulation time to a manageable level, each plasma region is divided into 15 cocentric cylindrical sub-regions along the horizontal x-direction and 38 sub-regions along the vertical $y-$direction, as shown in Fig. 4.4, where each region has constant photoconductivity. Although all the sub-regions have the same 10 µm size along the horizontal direction they are not equally sized along the vertical direction. As a result, the discretised distribution of the photoconductivity gives a more accurate approximation of the continuous profile when the illuminated regions are not evenly divided in the vertical direction [3]. It is clear that, due to symmetry, the 3-dimensional distribution can easily be obtained from the two 2-dimensional distributions by appropriate rotations about the axis of symmetry (i.e., the axis that passes through the center of the beam) as shown in Fig. 4.3.

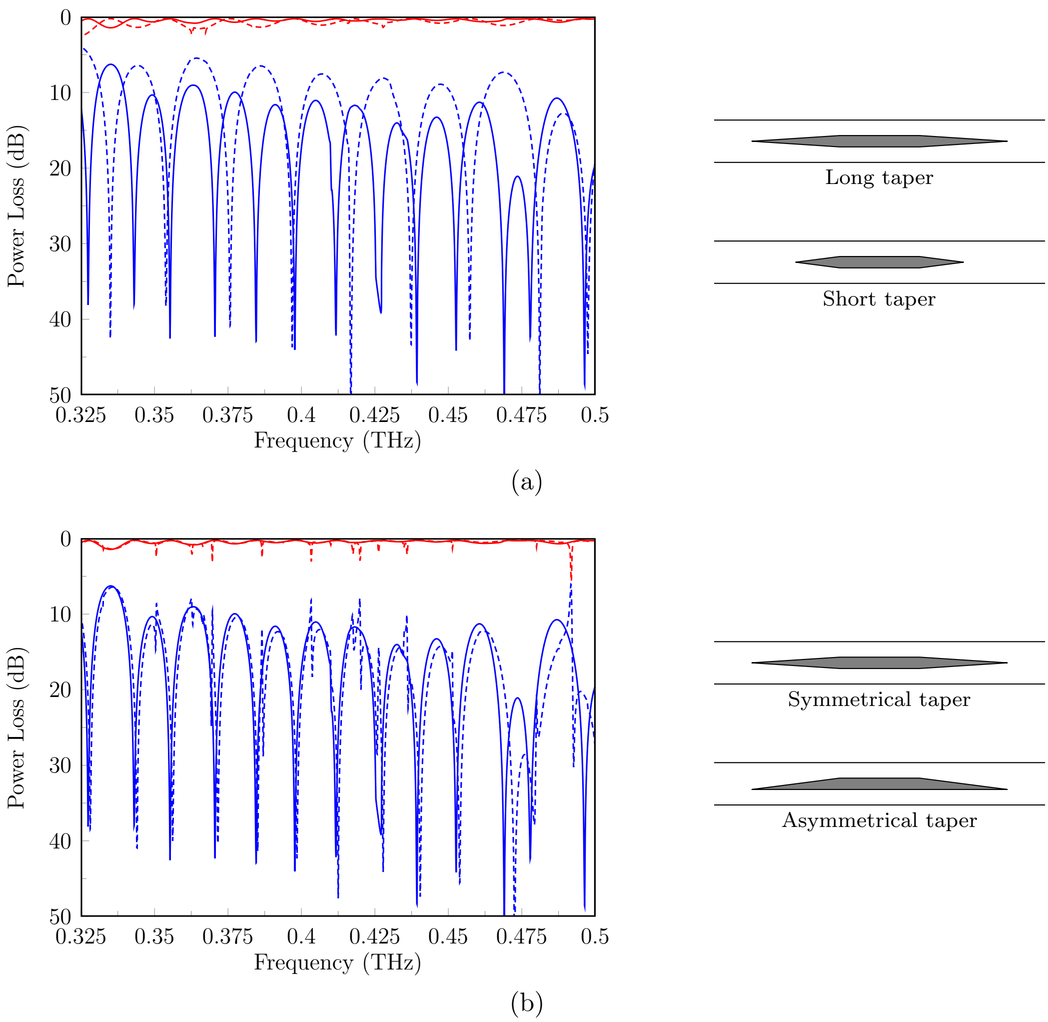

Figure 4.6: (a) Simulated reflection (blue curves) and transmission (red curves) characteristics without laser illumination for (a) different slab taper length as shown on the right panel (solid lines: 1.16 mm and dashed lines: 580 µm) and (b) different slab taper type as shown on the right panel (solid lines: symmetrical and dashed lines: asymmetrical).

Using the combined optoelectronic-electromagnetic modelling strategy adopted here, the electric field distribution within the waveguide can be generated, as shown in Fig. 4.5. It can be seen that the input THz wave is mainly confined within the HRS slab, and hence, choosing a slab width smaller than the width of the waveguide section, provides more efficient switching when illuminating the slab, due to greater interaction with the plasma regions. When the switch is optically excited (OFF state), effectively all of the incoming power is either absorbed or reflected by the plasma regions and practically no power is transmitted along the waveguide. On the other hand when the switch is in the ON state, the device operates as a typical rectangular waveguide and hence most of the power is transferred from the input to the output of the waveguide.

In order to further investigate the performance of the proposed switch design, various parametric studies were undertaken. First, different taper lengths and types were simulated, as shown in Fig. 4.6. A comparison of the reflection and transmission characteristics for a taper length of 580 µm and 1.16 mm is shown in Fig. 4.6(a), whereas, a comparison of

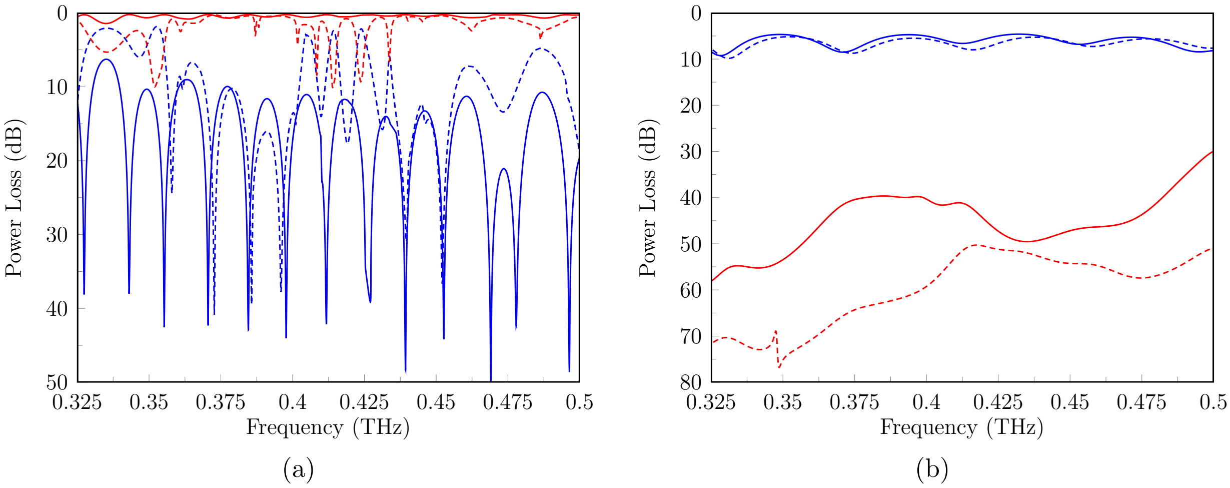

Figure 4.7: Simulated reflection (blue curves) and transmission (red curves) characteristics (a) without laser illumination and (b) with laser illumination. Solid lines: 50 µm holes. Dashed lines: 100 µm holes.

the power loss for two different taper types (i.e. symmetrical and asymmetrical taper) is presented in Fig. 4.6(b). As can be seen, smaller taper angle provides better impedance matching. However, a further increase of the taper length (beyond 1.16 mm) does not improve the device performance significantly and results in increased mechanical fragility. A significant increase in the physical length of the transformer, combined with the small cross-section of the slab, makes it vulnerable to breakage during assembly. To overcome this, the use of non-linear tapered ends (e.g., exponential) has been investigated in order to further reduce the taper angle while keeping its length constant. However, with taper length of 1.16 mm providing sufficiently good impedance matching, with a low risk of potential damage during assembly, the simpler design of the linear symmetrical taper with length 1.16 mm and angle 8^o is adopted.

Another parameter that has big impact on the performance is the size of the spots. Specifically, the region of the slab that is being illuminated across its width needs to be large, so that most of the propagating power is blocked. A parametric study of circular windows with different diameter of 50 µm and 100 µm is presented. As can been seen in Fig. 4.7 higher losses are introduced with larger hole radius since significant amount of the incoming power is radiated through the holes. However, with larger hole aperture, a more significant switching effect is obtained, since there is higher laser power absorption within the silicon slab.

Moreover, a study for different distances between two adjacent holes is conducted, as shown in Fig. 4.8, as well as a study of different number of holes. Changing the distance between the holes and hence the distance between discontinuities results in different reflection characteristics. Also, as can been seen in Fig. 4.9 an ON-OFF extinction ratio of approximately 30 dB is predicted with three circular holes on each broad wall of the waveguide, while a higher ratio of approximately 50 dB is predicted with four holes. As expected more plasma regions increase the level of ON-OFF ratio, but at the expense of longer device and more laser power.

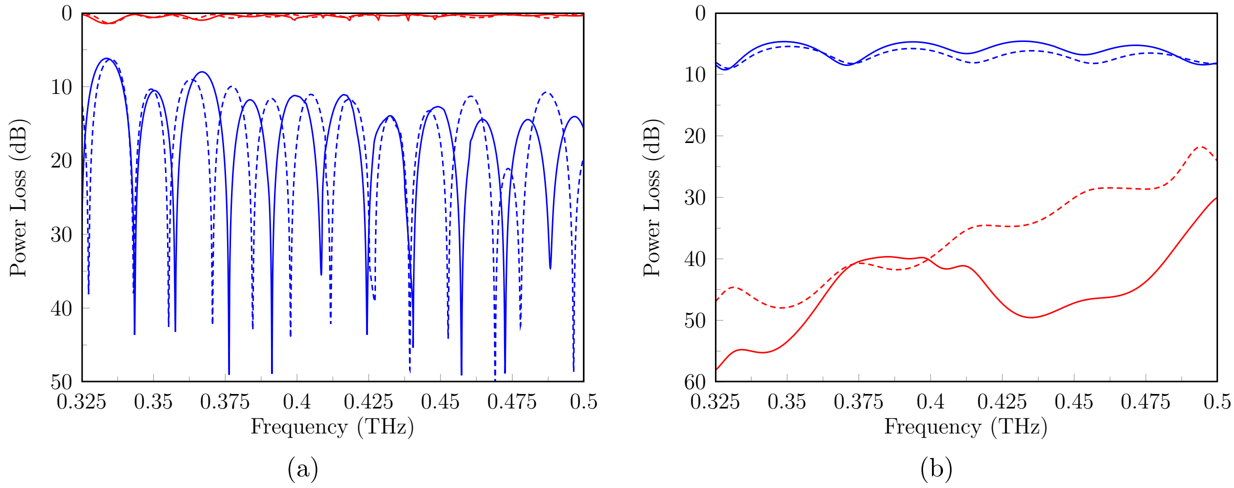

Figure 4.8: Simulated reflection (blue curves) and transmission (red curves) characteristics (a) without laser illumination and (b) with laser illumination. Solid lines: 300 µm distance between adjacent holes. Dashed lines: 150 µm distance between adjacent holes.

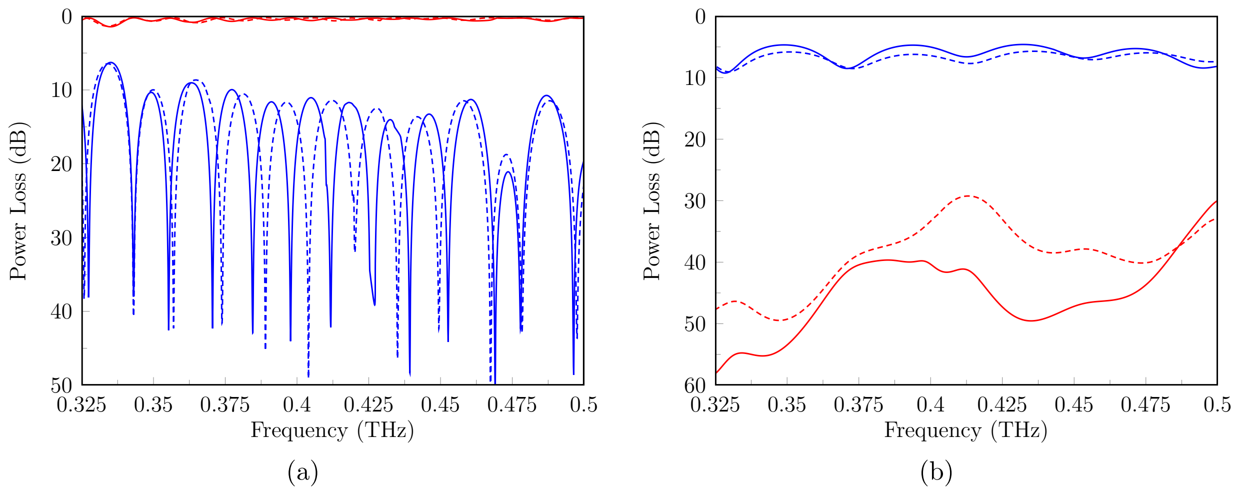

Figure 4.9: Simulated reflection (blue curves) and transmission (red curves) characteristics (a) without laser illumination and (b) with laser illumination. Solid lines: 4 holes. Dashed lines: 3 holes.

4.3 Modal Analysis

In partially-filled waveguides the supported modes in the general case are not transverse electric (TE) nor transverse magnetic (TM) with respect to the propagation direction but hybrid modes that can be characterised as longitudinal section electric (LSE) or longitudinal section magnetic (LSM). A complete analysis of such hybrid modes is beyond the scope of this work and can be found in [13, 14]. However, the dispersion characteristics for the LSE^x modes that are supported by the structure shown in Figs. 4.3 and 4.4 can be obtained by solving numerically the following modal equation

$$\frac{k_{x,\mathrm{a}}}{k_{x,\mathrm{d}}}\tan(k_{x,\mathrm{d}}d) - \frac{k_{x,\mathrm{d}}}{k_{x,\mathrm{a}}}\tan^2(k_{x,\mathrm{a}}w)\tan(k_{x,\mathrm{d}}d) + 2\tan(k_{x,\mathrm{a}}w) = 0 \tag{4.7}$$

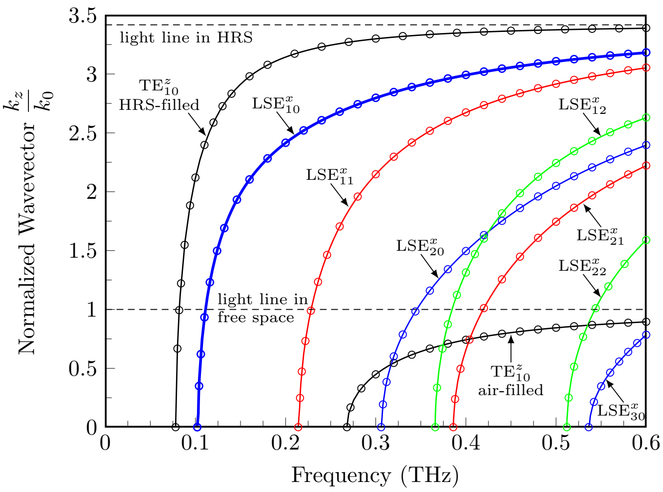

Figure 4.10: LSE^x modes in a partially-filled MPRWG. Solid lines: calculated values. Discrete symbols: simulated values using a full-wave solver. The fundamental TE$^z_{10}$ mode for an air-filled and HRS-filled MPRWG are also plotted. The light lines are also shown with dashed lines.

where $k_{x,\mathrm{a}} = \sqrt{k_0^2 - \left(\frac{n\pi}{b}\right)^2 - k_z^2}$ and $k_{x,\mathrm{d}} = \sqrt{\varepsilon_\mathrm{r} k_0^2 - \left(\frac{n\pi}{b}\right)^2 - k_z^2}$ are the x-component of the wave vector in the air and dielectric slab, respectively with $k_0 = \omega\sqrt{\mu_0\varepsilon_0}$ being the free-space wave number and ε_r the relative permittivity of the slab. The results are plotted in Fig. 4.10 where the cut-off frequencies for some of the LSE^x modes are shown. Here, only the LSE^x modes are shown because the waveguide is excited with the fundamental TE$_{10}$ mode and as such only the LSE^x modes can be excited. However, because there is no discontinuity along the vertical direction, only the LSE$^x_{m0}$ modes can be excited and due to symmetry only the LSE$^x_{m0}$ with odd m can actually be excited. Thus, for the switch described previously, the fundamental LSE$^x_{10}$ mode has a cut-off frequency at 0.102 THz while the first higher order mode (i.e, LSE$^x_{30}$) can be excited above 0.535 THz. For comparison, the cut-off frequency of an air-filled WR-2.2 waveguide is 0.268 THz while for a HRS-filled WR-2.2 waveguide is 78 GHz.

4.4 Thermal Analysis

In addition to the previous analysis, a thermal study is carried out in this section in order to take into account the heating effects from both the laser illumination and the waveguide excitation. When the device is connected to a power source electromagnetic losses will be introduced in the semiconductor block as well as on the waveguide metallic walls which cause the device to heat up. Moreover, the structure is excited by a CW laser source which results in further rise in temperature. However, at higher temperatures within the HRS slab, more electrons have enough energy to jump into the conduction band resulting in higher carrier concentration and thus higher conductivity within the HRS slab.

Specifically, a 2.5 mW power source [15], operating at 0.45 THz, is considered. Furthermore, in order to include the heating effect introduced by the laser source, a heat source of 1.5 mW is assigned at the surface of the HRS slab. This laser power corresponds to a measured power density of 40 W/cm² for a laser current of 1 A. Thus, the worst case scenario is considered where all the incident laser power is absorbed by the HRS slab. Moreover, the heat source has been designed as an array of four laser beams with beamwidth matching the size of the holes on the top and bottom walls. However, during the experiment, one large laser spot with diameter of approximately 3 mm was used to illuminate the holes on each waveguide wall. Thus, in the thermal modelling of the device it is assumed that the heating effect on the large metal walls is negligible due to the fast heat diffusion rate which results in better cooling of the gold walls. The steady-state temperature is calculated using CST Multiphysics Studio with Fig. 4.11 showing the temperature distribution in the structure, using an ambient temperature of 20°C (i.e. room temperature). It is obvious that the temperature inside the dielectric has not significantly increased reaching a maximum value of approximately 23.5°C. When the heat source power is increased to 4.5 mW, corresponding to a laser current of 2 A the temperature increases further with a maximum value of 26.5°C. In view of the above, it can be assumed that such a temperature increase will not have a significant influence on the material's conductivity and thus can be neglected.

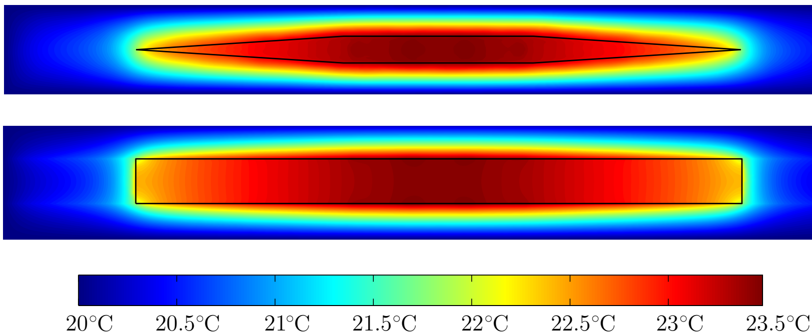

Figure 4.11: Temperature distribution for 1.5 mW laser power. Top: at the surface of the HRS slab. Bottom: side view.

4.5 Conclusion

In this chapter a new design of a terahertz optically-controlled waveguide plasma switch has been presented. The photoconductivity profile inside the dielectric slab has been studied extensively and a characterisation of the generated plasma is given. The switch design has been optimised through various parametric studies, while a modal analysis and a study of the thermal effects due to the laser illumination are presented. A detailed discussion about the switch behaviour and operation is presented alongside with its performance characteristics. Following the successful implementation of the plasma switch, various prototypes have been fabricated and experimentally tested, as will be presented in great detail in the following chapter.

The modelling results presented in this chapter show that the use of a combined opto-electromagnetic approach opens up completely new horizons in the design of real-time reconfigurable integrated terahertz devices, where various components can be implemented simply by adjusting the light pattern and the geometric characteristics of the beam spots.

References

[1] A. Ambroziak, “Semiconductor photoelectric devices”, *Iliffe Books*, London, 1968

[2] W. Platte, “Effective photoconductivity and plasma depth in optically quasi-CW controlled microwave switching devices”, *IEE Proc. J. Optoelectron.*, vol. 135, no. 3, pp. 251-254, Jun. 1988

[3] Y. Zhou and S. Lucyszyn, “Modelling of Reconfigurable Terahertz Integrated Architecture (RETINA) SIW Structures”, *PIER*, vol. 105, pp. 71-92, Jun. 2010

[4] http://www.synopsys.com/tools/tcad/devicesimulation/pages/taurusmedici.aspx

[5] http://www.cst.com/

[6] http://www.millitech.com/pdfs/recspec.pdf

[7] M. N. Afsar, H. Chi and X. Li, “Millimeter wave complex refractive index, complex dielectric permittivity and loss tangent of high purity and compensated silicon”, *Conf. Prec. Electrom. Meas.*, pp. 238-239, Jun. 1990

[8] F. Arndt, J. Bornemann and R. Vahldieck, “Design of multisection impedance-matched dielectric-slab filled waveguide phase shifters”, *IEEE Trans. Microw. Theory Techn.*, vol. 32, no. 1, pp. 34-39, Jan. 1984

[9] R. A. Waldron, “The theory of reflections in a tapered waveguide”, *Radio Electron. Eng.*, vol. 32, no. 4, pp. 245-254, Oct. 1966

[10] B. Y. Kapilevich and N. S. Simin, “Reflection from a dielectric wedge in a rectangular waveguide”, *Novosibirsk Electrotechn. Inst. Com.*, vol. 19, no. 1, pp. 135-140, Jan. 1976

[11] M. Khalal-Armirhosseini and H. Ghorbaninezhad, “Microwave impedance matching using waveguides filled by inhomogeneously dielectrics”, *Int. J. RF Microw. Comp. Aided Eng.*, vol. 19, no.1, pp. 69-74, Jan. 2009

[12] A. M. Marconnet, M. M. He, S. Sengele, S.-J. Ho, H. Jiang, N. J. Ferrier, D. W. van der Weide, V. Madhavan, N. Nelson and J. H. Booske, “Microfabricated silicon high-frequency waveguide couplers and antennas”, *IEEE Trans. Electron Dev.*, vol. 56, no. 5, pp. 721-729, May 2009

[13] C. A. Balanis, “Advanced engineering electromagnetics”, 1st ed., *Wiley*, New York, 1989

[14] R. E Collin, "Field Theory of guided waves", 2nd ed., *Wiley-IEEE Press*, New York, 1990

[15] http://www.rohde-schwarz.com/en/product/zvx-productstartpage_63493-8172.html

Chapter 5

Fabrication and Experimental Verification

Based on the design and simulation results reported in the previous chapter, the microfabrication process and experimental verification of a WR-2.2 rectangular waveguide switch are presented in detail. The device has been fabricated using bulk silicon-based microfabrication techniques with the waveguide being fabricated in two halves employing the split-block method. The overall fabrication process comprises four major steps, namely the manufacturing of the bottom die, top die, HRS slabs and waveguide flanges. Details of each individual step and the various sub-processes for optimum outcome are also given with potential issues that may significantly compromise quality being discussed. Moreover, the assembly of the prototypes is thoroughly explained with two different alignment approaches being investigated; a self-aligned approach (attached to the experimental setup) with the use of standard waveguide flanges and a second approach using plastic holders (detached from the experimental setup) offering increased flexibility in terms of spatial movement. Furthermore, the experimental setup for obtaining the behaviour of the prototypes is presented and the measured responses of the devices are discussed.

5.1 Microfabrication Process

The patterns/features on the devices are created using the method of Deep Reactive-Ion Etching (DRIE) [1–4]. This is an anisotropic etching method which uses the Bosch process (which has been originally developed by Bosch Inc.) [5] in order to create deep features i.e., high aspect ratio structures with vertical side walls. This process is applied in cycles with each cycle consisting of two steps, an etching step and a passivation step with sulfur hexafluoride (SF_6) being used in the former and octafluorocyclobutane (C_4F_8) in the latter. In the first step, dry chemical etching with almost vertical ion bombardment (i.e. isotropic plasma etch) is applied for a few seconds (typically 10-20 seconds) resulting in a silicon substrate etching depth of approximately 1 µm. Then, during the passivation cycle, the surface of the silicon substrate is coated with a "teflon-like" substance, forming a passivation layer, in order to protect the surface of the side walls from further etching. Next, because of the directional ion bombardment the plasma etches the passivation layer at the bottom of the features but not at the side walls. Once the protective layer is removed (i.e. etched),

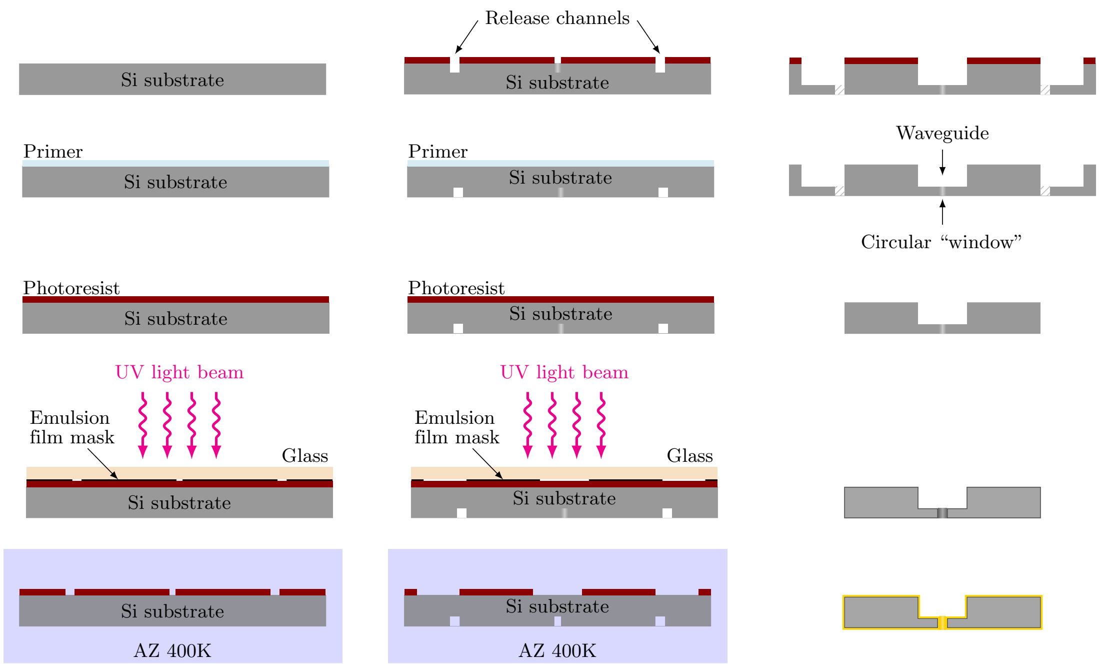

Figure 5.1: Sketch of the microfabrication process for the bottom die. First step is shown on the top left panel with the next one following underneath.

the silicon below the passivation layer is etched. As a result, the total etching time consists of a large number of small isotropic etch steps with each one etching only 0.5 µm to 1 µm of silicon. This approach results in more vertical features.

5.1.1 Bottom Die Fabrication

Although the aim is to use DRIE to pattern the silicon substrate, there are specific photolithography steps that need to be followed first, as shown in Fig. 5.1 [6–9]. First, a 100 mm diameter, single side polished, silicon wafer with thickness 525 µm and crystal orientation $< 1\ 0\ 0 >$, is dehydrated in the oven to remove the absorbed water from the wafer surface; the absorbed water is the result of exposing the silicon surface to the the clean room ambient conditions (i.e. humidity). An adhesion promoter, namely hexamethyldisilazane (HMDS), is then applied on the substrate by spinning a diluted solution onto the wafers in order to promote the adhesion of the photoresist. Next, the silicon substrate is spin-coated with AZ9260 photoresist, resulting in a resist film with expected thickness of approximately 10 µm [10]. The thickness of the photoresist is selected by taking into account the etch rate of the photoresist in comparison to the etching rate of silicon. Specifically, the etch rate of AZ9260 has been estimated to be 0.04 µm/min, while silicon etch rate is in the range of $2 - 3$ µm/min. Hence, a ratio of 1 µm of photoresist for every 48 µm of silicon is necessary.

After coating the substrate with photoresist, it is heated on a hotplate in order to reduce the solvent concentration of the resist film (i.e. softbake). This step is necessary in order to prevent photoresist contamination on the photomask (i.e. photoresist sticking on the mask) and improve the adhesion between photoresist and substrate. Moreover, it helps to minimise the dark erosion of the photoresist during development of the photoresist and avoid

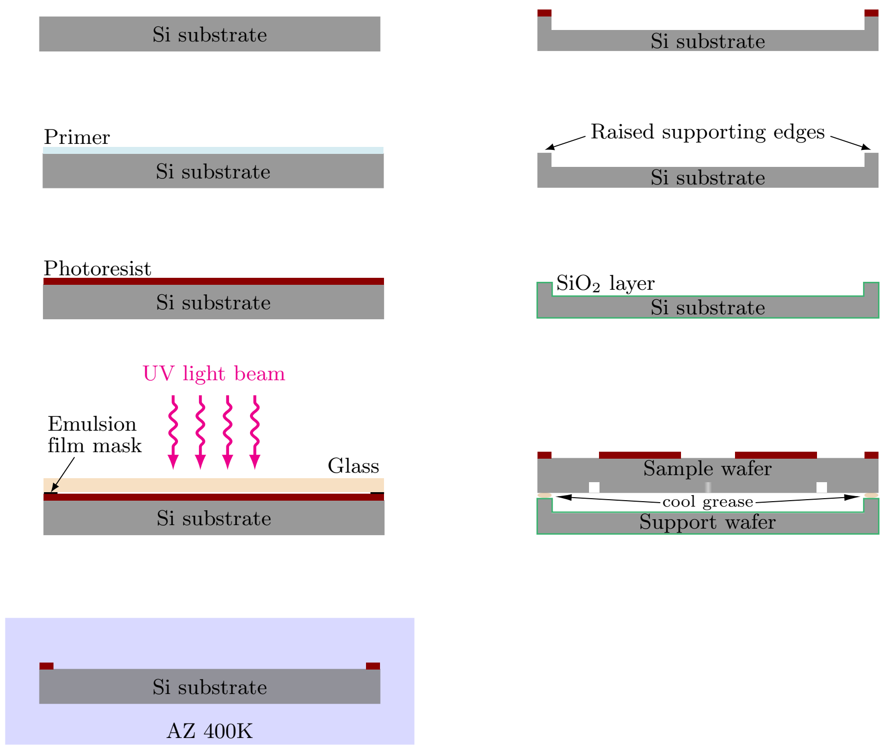

Figure 5.2: Fabrication process of the support wafer used during DRIE of the bottom dies.

bubbling of the solvent during dry etching. However, before exposing and developing the photoresist, it needs to rehydrate because water concentration drops during softbake. This is necessary since a certain water concentration is reqired during exposure in order to have a high development rate. Therefore, during the rehydration step, which is a delay time step between softbake and exposure, the missing water diffuses from the surrounding air into the photoresist film. However, sufficiently high air humidity of approximately 45% is needed for this proocess. The desired pattern is then transferred onto the wafer by selective exposure of the photoresist under ultraviolet (UV) radiation, with exposure wavelength of 360 nm using the Q4000 Quintel Mask Alignment System. During exposure, the chemical structure of the photoresist changes, becoming more soluble in the developer. Specifically, for positive photoresists, as the one used in this case, the parts of the photoresist which will be exposed through the pattern on the mask, are cleared by the developer solution and thus, on the mask the transparent regions are the ones which are going to be etched.

After exposure, the photoresist is developed using AZ 400K developer. In general, the developing time is reduced by increasing the exposure time. However, it is important to balance out these two factors because in the case that the photoresist is over-exposed, dark photoresist areas close to the exposed areas may also be illuminated and hence, cleared features after development are wider than expected. Also, in practice even the unexposed parts of the photoresist will start becoming soluble to the developer after a certain time and therefore over-developing should be avoided. Moreover, it is important to notice that any gaps between the mask and the photoresist surface or a rough substrate surface results in exposing parts of the photoresist that were meant to be dark. Finally, low power oxygen plasma treatment is then applied for a short time (approximately 3 min) in order to remove

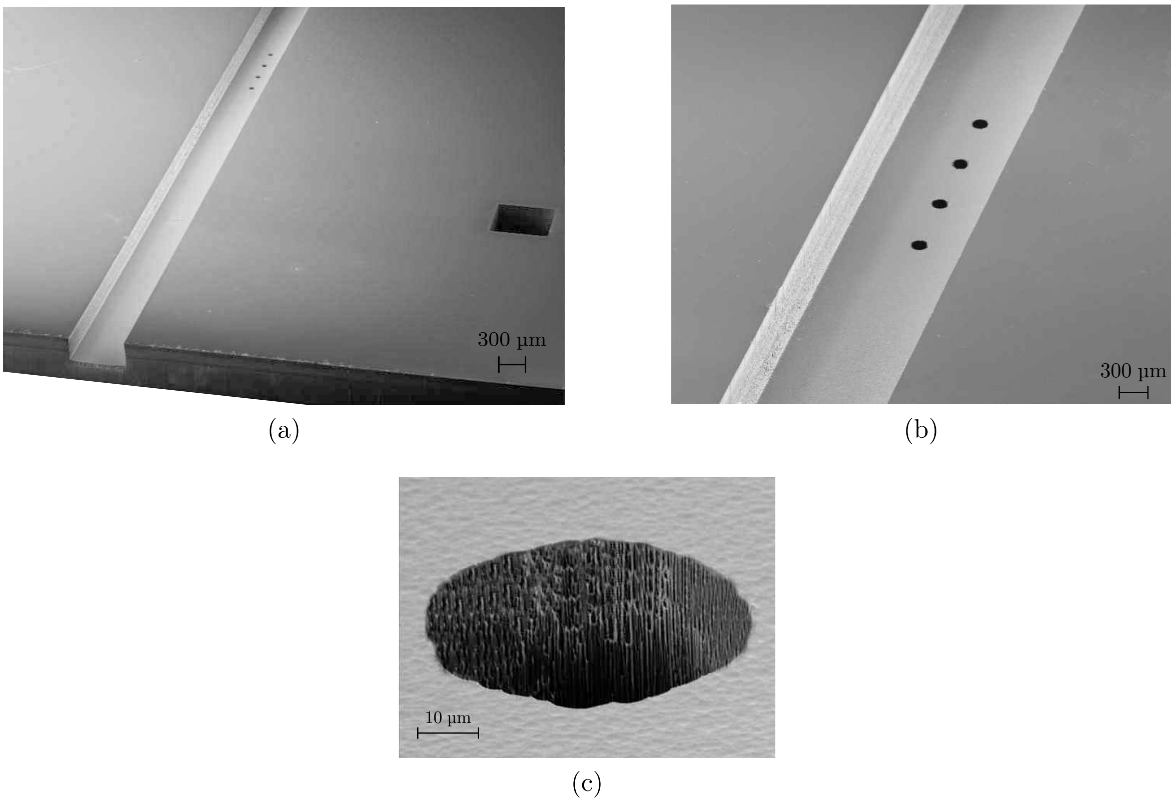

Figure 5.3: Fabricated WR-2.2 rectangular waveguide with four circular holes with 50 µm diameter. (a) Perspective view, (b) zoom in of the holes and (c) detailed view of a hole.

any photoresist residuals or thin photoresist film observed at the surface of the cleared features.

The above process is first applied on the rear (non-polished) side of a silicon wafer to form the pattern of the circular "windows" at the bottom of the waveguide. The pattern is then transferred to a depth of 245 µm by DRIE. It should be emphasized that the pattern transferred onto the wafer includes features with three different sizes, 50 µm, 70 µm and 100 µm. Each of these corresponds to a different etch rate. Thus, for a given etch time, various etch rates are observed and since we aim all the features need to be etched down at least to 245 µm longer etch time is required.

Next, the bulk photoresist is stripped with acetone and then the wafer is rinsed with isopropyl alcohol (IPA) using ultrasonic agitation in order to remove the photoresist contaminated acetone and with deionized (DI) water at the end. Subsequently, any photoresist residuals are removed using Shipley Microposit Remover 1165 with the wafer being submerged in a heated bath at 70 °C for 30 min. Finally, high power oxygen and argon plasma clean (using Asher) is applied in order to remove any remaining photoresist at the wafer's surface. In our case, it is critical to remove any organic contamination from previous processing or any particles from the cleanroom environment since a second photolithorgaphy will then be applied on the back surface of the wafer. However, with significant contamination, piranha etch (i.e. using a mixture of sulfuric acid (H_2SO_4) and hydrogen peroxide (H_2O_2)) should be used to clean silicon wafers, although not recommended unless required.

A second lithography step is performed on the top side (polished-side) of the wafer for the

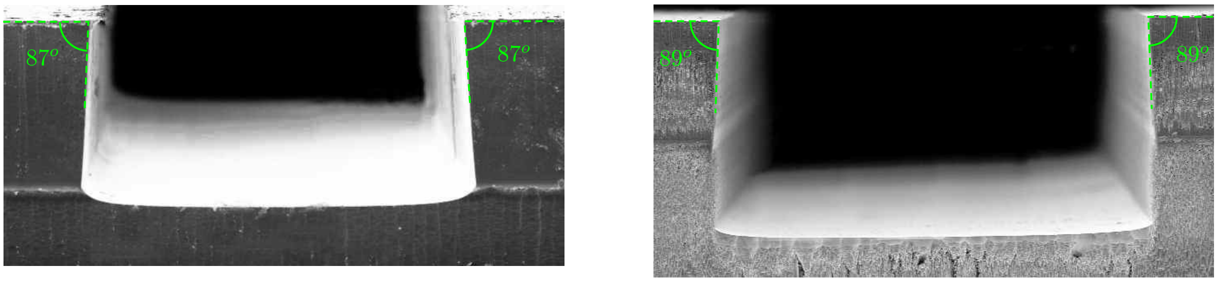

(a) (b)

Figure 5.4: SEM picture of the deep waveguide channel cross-section from a silicon wafer processed with DRIE at an angle of (a) 90° with respect to the wafer's primary flat and (b) 45° with respect to the wafer's primary flat.

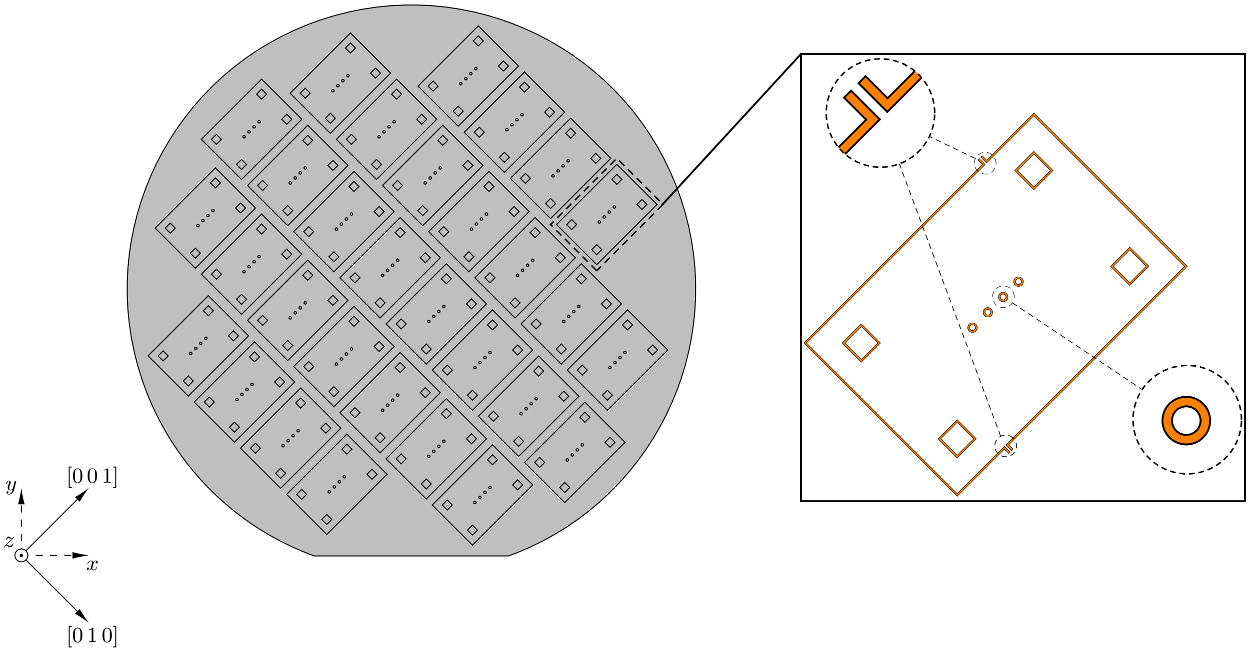

Figure 5.5: Schematic of the pattern alignment on the silicon wafer during DRIE processing. Left-hand side: Top view. Right-hand side: Detailed view.

fabrication of the rectangular waveguide sections, which is similar to the process performed on the back side. As explained previously, after a substrate dehydration step, an adhesion promoter is applied on the silicon wafer followed by spining a photoresist film on the surface. A softbake and rehydration step are performed before exposure of the photoresist. In order to obtain good alignment of the features on both sides of the wafer (i.e. the circular "windows" on the rear side aligned with the waveguide pattern on the front side) alignment marks are patterned opposite to each other on both surfaces of the wafer, as will be explained in greater detail in the following section. Once the wafer is exposed and the photoresist is developed, the waveguide pattern is transferred down to meet the original back-etch by DRIE.

Prior to etching, the process wafer (i.e. wafer having the devices) needs to be mounted onto a carrier wafer. This is necessary since the final structures detach from the process wafer when the etch has gone through the wafer thickness, damaging the chuck by exposing

Table 5.1: Waveguide bottom die fabrication process steps.

Fabrication Step	**Process**	**Parameters**
1. Rear side patterning	Lithography 10 µm	– HMDS Spin: 1000 rpm, 1000 rpm, 90 sec – AZ9260, 10 µm thick Spin (1st run): 500 rpm, 500 rpm/s, 10 sec Spin (2nd run): 2000 rpm, 2000 rpm/s, 60 sec Spin (3rd run): 3000 rpm, 3000 rpm/s, 2 sec – Softbake (HP): 60 °C for 5 min, 100 °C for 15 min – Exposure: 600 mJ/cm^2 – Develop: AZ400K:DI 1:4 for 5 min
	DRIE 245 µm (STS ICP)	– Recipe: Dark 3s (stored on STS system) Duration: 128 min
	Resist Strip	– 1165 @ 70 °C immersion (30 min) – DI rinse, O_2 plasma clean (10 min)
2. Front side patterning	Lithography 10 µm	Same as in step 1
	DRIE	Etch through to the support wafer in steps of 15 min with 15 min cooling in between
	Resist Strip	Same as in step 1
3. Support wafer preparation	Lithography 10 µm	Same as in step 1
	DRIE 200 µm (STS ICP)	– Recipe: Dark 4s (stored on STS system) Duration: 100 min
	SiO_2 layer	1100 °C for 24 hours
	Bond with device wafer	Cool grease, 65 °C for 2 min
4. Metallise rear side	Sputter coating	30 nm Cr (adhesion), 550 nm Au
5. Metallise front side	Sputter coating	Same as in step 4

it to the plasma. However, when using a carrier wafer there are several issues which need to be taken into account. In general, during DRIE the wafer is mechanically clamped to the chuck with Helium flowing between the chuck and the wafer for backside wafer cooling. When bonding the wafer under process with a carrier wafer a thermally conductive material is used in order to keep the process wafer at a constant temperature. However, bonding two silicon wafers together using some adhesive (e.g. photoresist, cool grease) inevitably changes the wafer temperature and in turn the actual etch. Especially, in this case, with deep features etched at the back side of the process wafer, the thermal contact between the sample and the support wafer will be poor resulting in rise of the sample's temperature. Therefore, with the etch process being sensitive to the wafer temperature, higher temperature could cause distortion in the features' size. An alternative way, which has been proven to improve the thermal contact between the support and sample wafer, is the use of cool grease. However, with the latter approach, wafer etching residuals of cool grease are trapped into the back side features and contaminate the wafer surface.

In order to overcome the above issues, a 5 mm wide support ring is formed at the perimeter

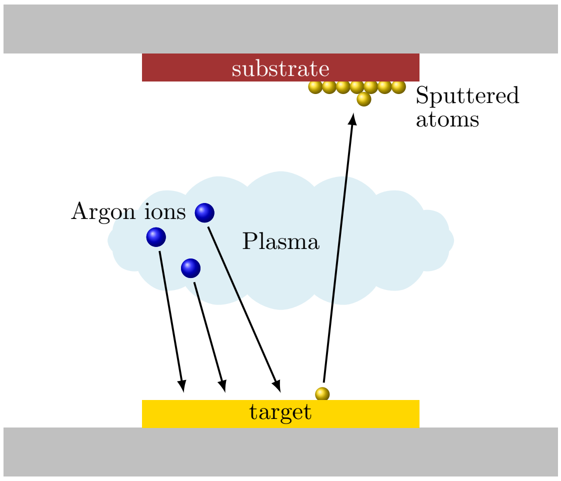

Figure 5.6: Schematic representation of an RF sputtering system.

of the carrier wafer prior to wafer bonding, by reactive ion etching, on which the process wafer is mounted using cool grease, as shown in Fig. 5.2. The carrier wafer then undergoes thermal oxidation (using a box furnace). During this process, a thin silicon dioxide layer (approximately 1 µm) is formed at the surface on both sides of the wafer, with the oxide layer acting as an etch stop during DRIE of the process wafer. The thermal oxidation is performed at 1100 °C, at which temperature the oxygen from the air diffuses into the silicon and reacts with it, forming silicon dioxide. Although, the use of the support ring improves the cooling of the sample, it has been found that it is still necessary to reduce the etch time to 15 min and let the sample cool for 15 min between etch steps using the gas flow as a means of cooling. The fabricated bottom die is shown in Fig. 5.3, where a perspective view of the waveguide channel and a more detailed view of the holes is presented.

In Fig. 5.4 a cross-section of the fabricated waveguide is shown. The difference between the two samples is that in the second sample the silicon substrate has been etched with the pattern edges having 45° alignment with respect to the primary wafer flat (Fig. 5.5), with the silicon substrate having a silicon crystal orientation $< 1\,0\,0 >$. In this case etching the Si results in more vertical sidewalls. As shown in Fig. 5.4(a) the sidewalls of the sample etched with an angle of 90° are negatively tapered with an angle of approximately 87° while the sidewalls sample in Fig. 5.4(b) are tapered with an angle of approximately 89°.

Finally, both sides of the structure are coated with gold (Au). However, a 30 nm seed layer of chromium (Cr) needs to be first sputtered on the silicon surface in order to improve the adhesion between the Au layer and silicon substrate. Then a 550 nm layer of Au is sputtered on the front side of the wafer to form the metal walls of the waveguide. In general, a wall thickness of approximately 5 skin depths is regarded as being enough to ensure complete isolation. However, a limiting factor with sputtering thick layers is the stress that builds up in the layer during the process. As a result, if the deposited film is too thick it will break or lose adhesion. Nevertheless, for thicker films different techniques can be used (e.g. electroplating), resulting in higher surface roughness of the deposited film compared to sputter deposition and hence have not be considered in this case. In view of the above, the thickness of the Au has been chosen to be approximately 4.5 times the skin depth at 0.325 THz. During sputter deposition, atoms are ejected from a solid target material (i.e. Au

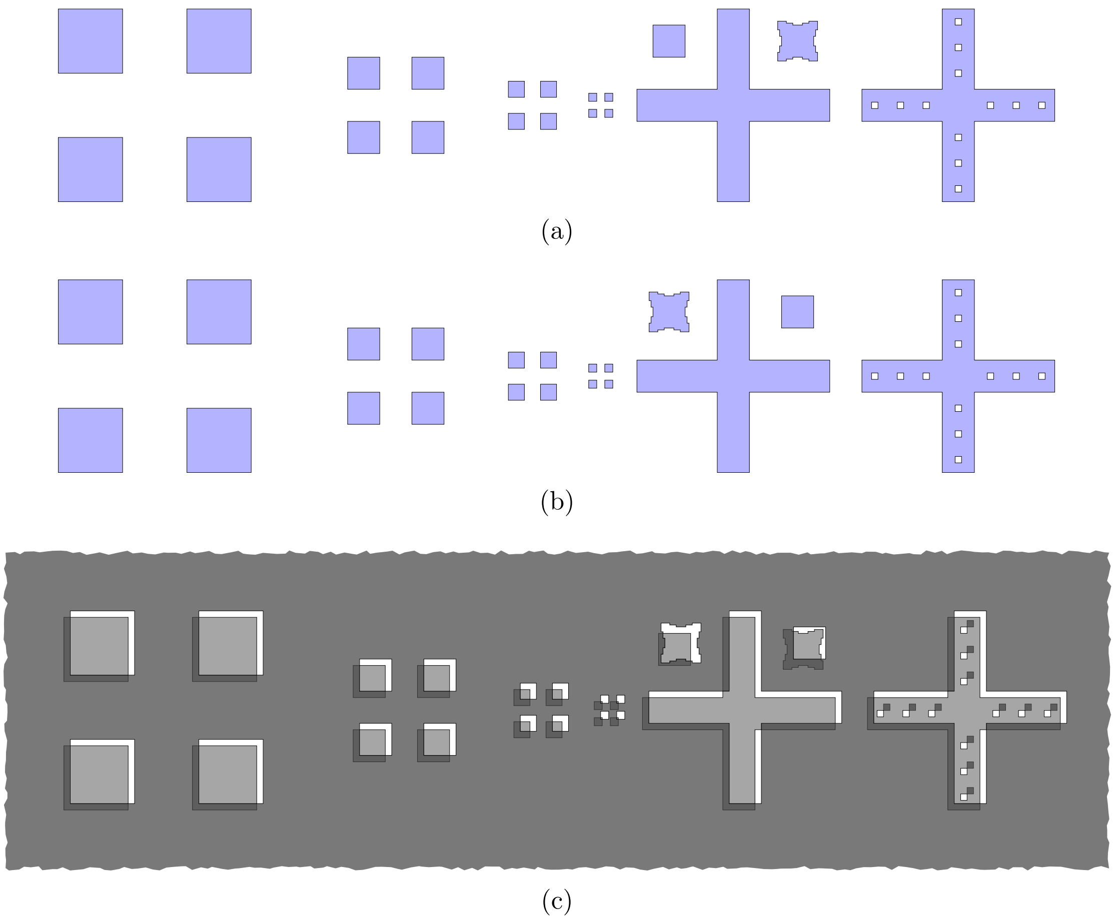

Figure 5.7: Alignment marks on the darkfield photomasks. (a) Alignment marks on the first photomask and (b) alignment marks on the second photomask. Features in blue colour are clear on the photomask. (c) Alignment features (light grey) on the back side of the wafer and alignment marks on the photomask (dark grey).

target) onto a substrate (e.g. silicon wafer), as shown in Fig. 5.6. The atoms' ejection is due to bombardment of the target by incident particles (i.e. argon atoms), which are supplied by a plasma source, with high kinetic energy. These particles cause adjacent energetic collisions of atoms in the target. When the latter reach the surface of the target with energy higher than the surface binding energy, atoms are ejected. The Au sputter deposition has been conducted in 10 minutes steps with 10 minutes cooling in between.

Also, prior to Cr or Au deposition at the sample's surface, the sample is plasma cleaned using Ar atoms which are large in size and can physically remove any particles at the sample's surface. Moreover, before deposition, Au and Cr targets are pre-sputtered in order to clean the target surface. This is particularly necessary for the Cr target, since the surface of the target is oxidised when exposed to ambient air. The same process is being used for the back side of the samples as well, in order to create a 550 nm reflective layer on the silicon substrate. The processing steps explained in detail previously are summarised in Table 5.1

5.1.2 Back-Side Alignment

In order to form the bottom die, the silicon is patterned using two photomasks. The first

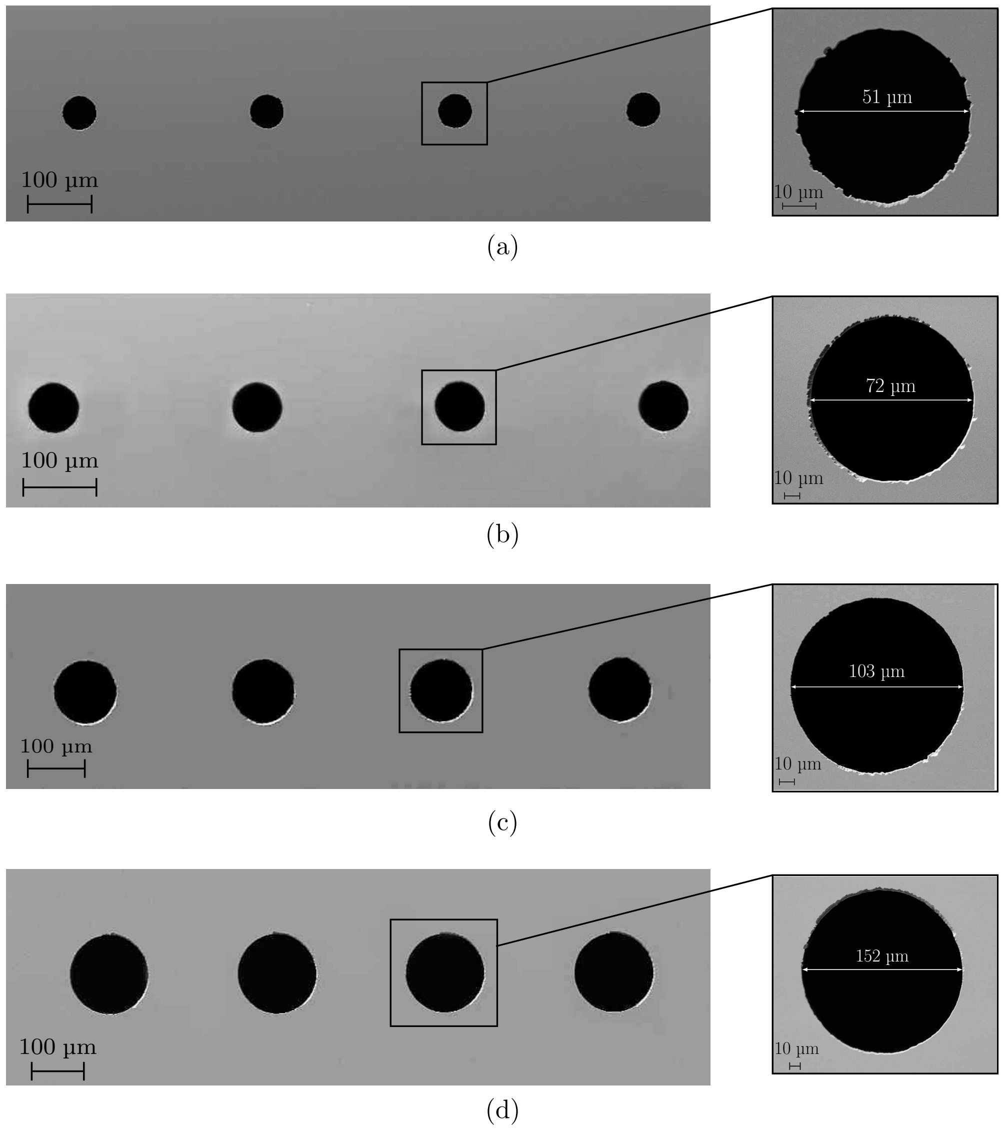

Figure 5.8: Top view of four circular holes etched on the top die with diameter of (a) 50 µm (b) 70 µm (c) 100 µm (d) 150 µm.

mask, which is used to pattern the rear side of the substrate, includes the circular holes and the second mask consists of the rectangular waveguide sections. In this case the features on both sides need to be aligned and hence, alignment marks are included on both photomasks, as shown in Fig. 5.7, and are located on both far ends of the mask.

Backside alignment is achieved by using infrared (IR) illumination, since the normal semiconductor materials (e.g. silicon) are transparent to IR wavelengths –which is normally invisible to the human eye but visible to some video cameras– providing images of the pattern on the back side of a substrate. Specifically, the mask aligner chuck allows the introduction of an IR light source under the wafer [11]. This is accomplished by two cavities created in the chuck into which a fiberoptic light cable is introduced, allowing the light to be directed upwards to the back of the wafer. Then by adjusting the stage and using a high magnification microscope the alignment marks on the mask are aligned with the back-side alignment features, which have already been etched, as shown in Fig. 5.7(c).

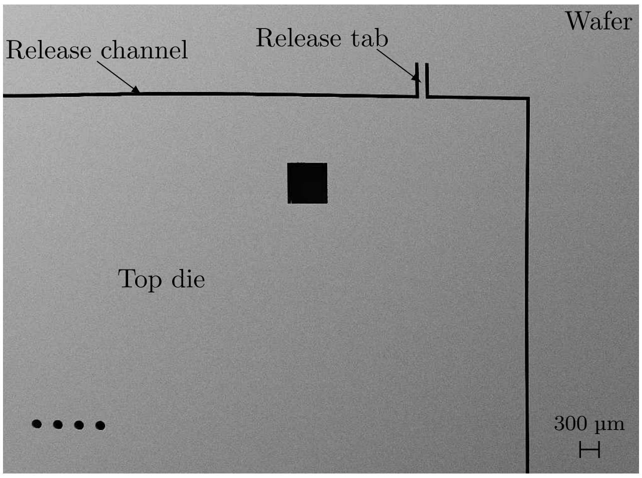

Figure 5.9: Partial view of the top die. The release channel and one release tab (which are used to release the device from the rest of the wafer) also shown.

The alignment marks have been placed strictly inside the region of the wafer which is visible using the IR light and must also fit within the field of view of the microscope objectives. In order to achieve accurate alignment in the x, y and θ orientations, three cross structure alignment marks with various sizes are included on both masks, as shown in Fig. 5.7(a)-(b). The misalignment offset using these alignment marks is 10 µm (which is also the resolution of the printed photomask).

5.1.3 Top Die Fabrication

Next, after the fabrication of the bottom die, the top die is developed using again a 100 mm, $< 1\ 0\ 0 >$, single-sided polished, 525 µm thick silicon wafer. The top half forms the top broad metal wall of the waveguide with circular “windows” in the centre. Similar lithography steps are applied here as well, with the only difference of a thicker photoresist film. Specifically, in this case the polished side of the wafer is spin-coated with a 15 µm photoresist film. The reason for using a thicker photoresist layer is the low etch rate of the 50 µm features which need a total time of approximately five hours in order to etch through. With an etch rate of 0.04 µm/min approximately for the AZ9260 photoresist, a film of 10 µm would be etched away after approximately 4 hours and 15 minutes and hence a thicker layer is required.

Also, the sample wafer needs to be mounted on a carrier wafer before etch through, as described previously. Thus, after dehydrating the carrier wafer in the oven for 30 min a thin layer (2 µm) of S1813 photoresist is spun on the entire wafer surface which acts as an adhesion between the carrier wafer and sample. Then the sample is placed on the carrier wafer and alignment between the two wafers is obtained using the primary flats. Next, the wafers are bonded together by applying light pressure on the sample and they are baked on the hotplate at 100 °C for 3 minutes until the photoresist is fully baked. Otherwise, any remaining liquid forms bubbles during DRIE, resulting in poor thermal contact. The sample is then etched through for 5 hours and 15 minutes using DRIE.

However, different size features included on the same wafer result in different etch rates and therefore, significantly different total time needed for the different features to etch through. In particular, with smaller features corresponding to lower etch rate, large surface

Table 5.2: Waveguide top die fabrication process steps.

Fabrication Step	**Process**	**Parameters**
1. Patterning	Lithography 15 µm	– HMDS Spin: 1000 rpm, 1000 rpm, 90 sec – AZ9260, 15 µm thick Spin (1st run): 500 rpm, 500 rpm/s, 10 sec Spin (2nd run): 1000 rpm, 1000 rpm/s, 60 sec Spin (3rd run): 4000 rpm, 4000 rpm/s, 2 sec – Softbake (HP): 60 °C for 5 min, 100 °C for 15 min – Exposure: 600 mJ/cm^2 – Develop: AZ400K:DI 1:4 for 5 min
	DRIE 425 µm (STS ICP)	– Recipe: Dark 3s (stored on STS system) Duration: 255 min
	Bond with device wafer	
	DRIE 100 µm (STS ICP)	– Recipe: Dark 3s (stored on STS system) Duration: 60 min
	Resist Strip	– 1165 @ 70 °C immersion (30 min) – DI rinse, O_2 plasma clean (10 min)
2. Support wafer preparation	Lithography 2 µm	– S1813, 2 µm thick Spin (1st run): 500 rpm, 500 rpm/s, 10 sec Spin (2nd run): 1000 rpm, 1000 rpm/s, 40 sec – Softbake (HP): 110 °C for 2 min
	DRIE 200 µm (STS ICP)	– Recipe: Dark 4s (stored on STS system) Duration: 60 min
3. Metallise rear side	Sputter coating	30 nm Cr (adhesion), 550 nm Au
4. Metallise front side	Sputter coating	Same as in step 3

area features are over-etched. In order to balance this effect, the size of the features on the mask are in the range of 50 µm to 100 µm (Fig. 5.8). Again, both sides of the wafer were sputtered coated with Cr and Au (with a thickness of 550 nm) forming the final broad metal wall of the waveguide on the polished side and a reflective layer on the non-polished side. In Fig. 5.8 a top view of the etched circular holes with different aperture size is shown. The devices are then released from the rest of the wafer through the release channel using release tabs, as shown in Fig. 5.9. The above processing steps are given in Table 5.2

5.1.4 HRS Slabs Fabrication

The fabrication of the tapered HRS slab, as shown in Fig. 5.10, is conducted in two steps. First, a HRS wafer (i.e. indicated wafer resistivity of > 10 kΩ·cm with ±30% resistivity tolerance) with initial thickness of 525 µm is thinned down to a final thickness of approximately 280 µm using isotropic reactive ion etching (RIE). During this process, the silicon substrate is being bombarded by SF_6 ions, with high plasma power. Although the initial wafer surface is polished (with indicated total thickness variation < 5 µm), after RIE, the surface is no longer optically flat with an expected etch rate variation of 10% across the wafer surface. For a total etch depth of 245 µm, a final thickness variation of approximately < 25 µm is

Figure 5.10: Illustration of a HRS tapered slab.

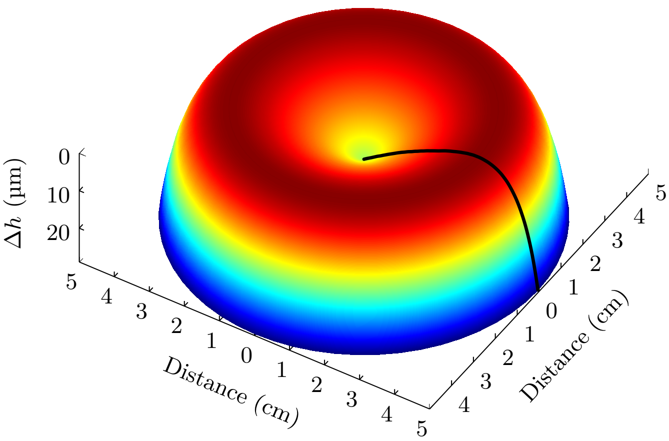

Figure 5.11: Measured wafer thickness variation. Dark red corresponds to the reference value ($\Delta h = 0$) and dark blue corresponds to maximum thickness variation.

expected. After inspection of the wafer, using an optical profilometer, the thickness across the wafer has a maximum measured variation of $\Delta h < 30$ µm as shown in Fig. 5.11, matching the estimated value. However, the thickness changes rapidly close to the edge of the wafer, resulting in smaller total thickness near the edge, and hence this part of the wafer is not being used for device fabrication. The thickness variation across the surface from the center of the wafer to a diameter of 90 mm is approximately 15 µm.

Once the wafer thickness is adjusted to the internal height of the rectangular waveguide, the slabs are developed using photolithography and DRIE on the processed wafer. As already explained, in order to pattern the slabs on the wafer surface, AZ9260 photoresist is spin-coated and the wafer is etched through after being mounted on a carrier wafer using resist S1813 as an adhesion layer. The photoresist is then stripped using Shipley Microposit Remover 1165 and any photoresist residuals are then removed using oxygen and argon plasma, as given in Table 5.3. A tapered fabricated slab placed inside the waveguide is shown in Fig. 5.12

5.1.5 Waveguide Flange Fabrication

This section describes the fabrication of waveguide flanges used to provide good alignment between the sample and waveguide heads used in the experimental setup. As described in the previous sections, photolithography was used to transfer the pattern of the flanges onto the wafer. The processing steps are the same as the ones explained in section and are summarised in Table 5.4. Then the process wafer is bonded with a backing wafer and the pattern is etched through using DRIE. The photoresist is then removed using organic solvents and finally the silicon wafer is cleaned with plasma in order to remove any organic

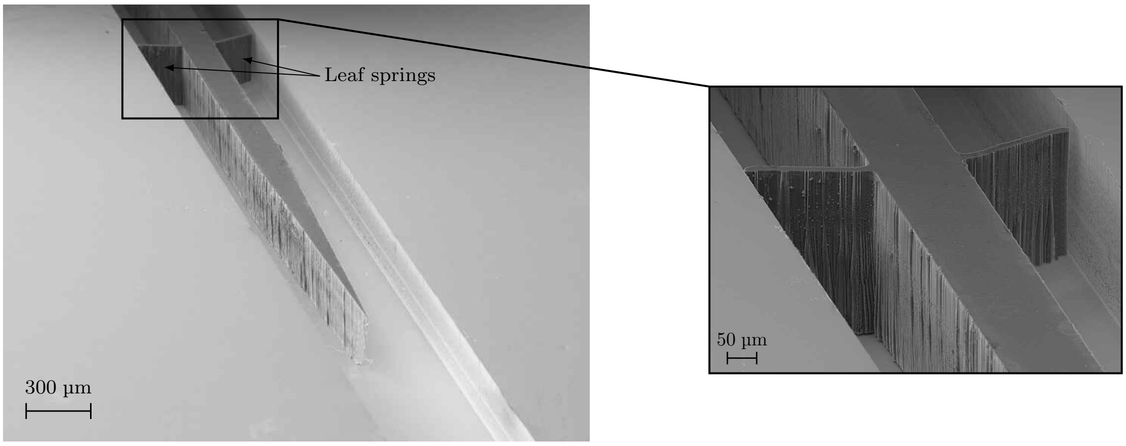

Figure 5.12: Scanning electron microscope pictures of the waveguide having spatial dimensions of $a \times b = 560 \times 280$ µm². The HRS tapered slab and the leaf springs are also shown.

contamination. Both sides of the wafer are then sputtered-coated with chromium and gold forming a layer of 550 nm.

The flange connection face has been designed according to the WR-2.2 waveguide flange standard, including etched holes for bolts and dowel pins which are used to ensure accurate alignment as shown in Fig. 5.13. Also, a rectangular aperture with spatial dimensions 10.02×1.07 mm² has been created so that the final waveguide device can fit into. Finally,

Table 5.3: HRS slabs fabrication process steps.

Fabrication Step	**Process**	**Parameters**
1. Thinning	RIE isotropic 245 µm (STS ICP)	– Recipe: Isotrop 4 (stored on STS system)
2. Patterning	Lithography 10 µm	– HMDS Spin: 1000 rpm, 1000 rpm, 90 sec – AZ9260, 10 µm thick Spin (1st run): 500 rpm, 500 rpm/s, 10 sec Spin (2nd run): 2000 rpm, 2000 rpm/s, 60 sec Spin (3rd run): 3000 rpm, 3000 rpm/s, 2 sec – Softbake (HP): 60 °C for 5 min, 100 °C for 15 min – Exposure: 600 mJ/cm^2 – Develop: AZ400K:DI 1:4 for 5 min
	DRIE 180 µm (STS ICP)	– Recipe: Dark 3s (stored on STS system) Duration: 60 min
	Bond with device wafer	
	DRIE 100 µm (STS ICP)	– Recipe: Dark 3s (stored on STS system) Duration: 30 min
	Resist Strip	– 1165 @ 70 °C immersion (30 min) – DI rinse, O_2 plasma clean (10 min)
3. Support wafer preparation	Lithography 2 µm	– S1813, 2 µm thick Spin (1st run): 500 rpm, 500 rpm/s, 10 sec Spin (2nd run): 1000 rpm, 1000 rpm/s, 40 sec – Softbake (HP): 110 °C for 2 min

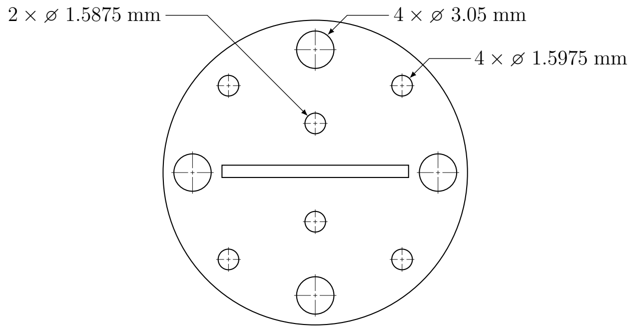

(a)

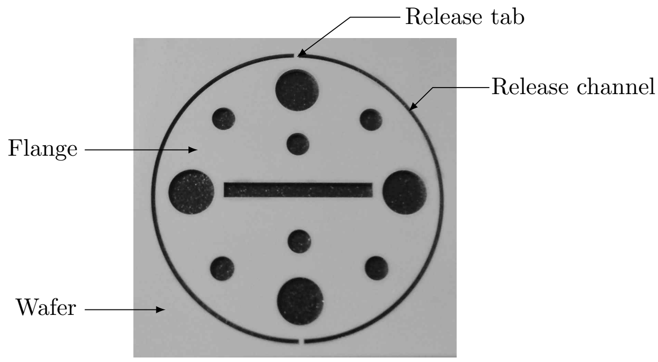

(b)

Figure 5.13: WR-2.2 standard waveguide flange. (a) Schematic and (b) fabricated.

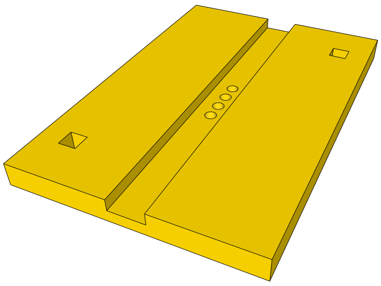

(a)

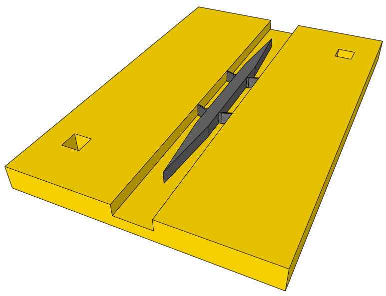

(b)

Figure 5.14: Illustration of (a) a bottom die consisting of a WR-2.2 waveguide with four circular holes for laser illumination. (b) Illustration of the bottom die as shown in (a) including a HRS tapered slab. Two square holes placed at the two opposite corners of the die are used for alignment of the top and bottom dies.

the waveguide section and the flange are joined using epoxy adhesive in order to provide more stiff support.

5.2 Assembly of the Prototypes

The assembly of the final devices is performed with the aid of a microscope since their dimensions are of the order of hundreds of microns and, therefore, a high degree of precision is required. One of the challenges was to place the HRS slab inside the fabricated waveguide

Table 5.4: Waveguide flanges fabrication process steps.

Fabrication Step	**Process**	**Parameters**
1. Patterning	Lithography 10 µm	– HMDS Spin: 1000 rpm, 1000 rpm, 90 sec – AZ9260, 15 µm thick Spin (1st run): 500 rpm, 500 rpm/s, 10 sec Spin (2nd run): 1000 rpm, 1000 rpm/s, 60 sec Spin (3rd run): 3000 rpm, 3000 rpm/s, 2 sec – Softbake (HP): 60 °C for 5 min, 100 °C for 15 min – Exposure: 600 mJ/cm^2 – Develop: AZ400K:DI 1:4 for 5 min
	DRIE 400 µm (STS ICP)	– Recipe: Dark 3s (stored on STS system) Duration: 135 min
	Bond with device wafer	
	DRIE 125 µm (STS ICP)	– Recipe: Dark 3s (stored on STS system) Duration: 45 min
	Resist Strip	– 1165 @ 70 °C immersion (30 min) – DI rinse, O_2 plasma clean (10 min)
2. Support wafer preparation	Lithography 2 µm	– S1813, 2 µm thick Spin (1st run): 500 rpm, 500 rpm/s, 10 sec Spin (2nd run): 1000 rpm, 1000 rpm/s, 40 sec – Softbake (HP): 110 °C for 2 min
3. Metallise rear side	Sputter coating	30 nm Cr (adhesion), 550 nm Au
4. Metallise front side	Sputter coating	Same as in step 3

(Fig. 5.14). With the use of extra fine tip tweezers, in order to avoid damaging the leaf springs, the slabs were put in place at the center of the waveguide. Since the width of the dielectric slab is significantly smaller than the width of the waveguide the use of the leaf springs is crucial in order to keep the slab in position during the experiment. The next step was to form an electrical contact between the top and bottom half of the waveguide. With both wafer surfaces in contact been polished, and thus optically-flat, after been metallised with Cr/Au they formed a good electrical contact.

The two dies are then bonded using silver conductive adhesive. The adhesive is applied at the Au/Au interface of the dies, through two square holes (etched through) on the top die, providing mechanically and electrically stable bond. The top and bottom dies are first aligned using an alignment apparatus shown in Fig. 5.15, in house-machined specifically for these devices. Both dies are kept in alignment position by applying a small force through a spring. The adhesive is then applied through two square apertures to achieve a void-free large area bonding. Finally, the prototypes are bonded with the fabricated flanges using epoxy adhesive, as explained in the previous section in more detail. An illustration of the final device is shown in Fig. 5.16(a), whereas in Fig. 5.16(b) an alternative (sub-optimal) alignment approach without flanges is shown, as will be discussed later.

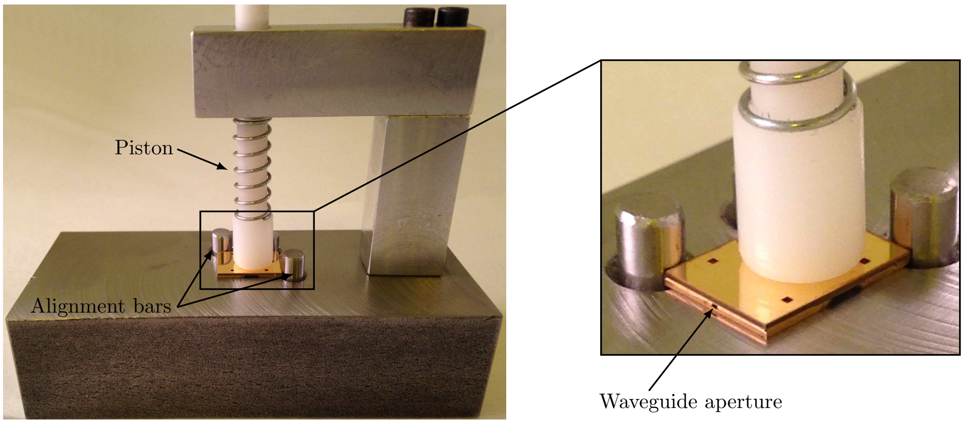

Figure 5.15: Alignment setup for aligning the two halves of the device.

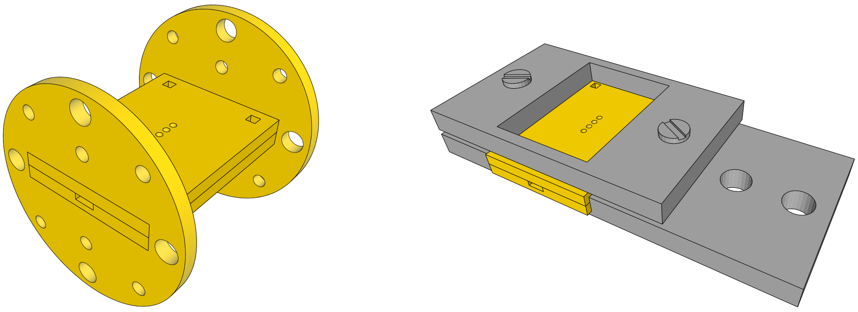

Figure 5.16: Two types of experimental setup used for the power loss measurement of the prototypes. (a) The device is self-aligned with the fabricated flanges. (b) The device is mounted on a plastic holder attached to a linear translation stage.

5.3 Experimental Verification

5.3.1 Resistivity Measurements

As explained in the previous chapter, it is necessary to use a high resistivity silicon substrate in order to obtain highly conductive regions under laser illumination. However, with the wafer having been exposed to plasma treatment, it is necessary to estimate the impact on the resistivity of the substrate material. Therefore, the resistivity of the wafer is measured using a four probe measurement setup, as shown in Fig 5.17.

The apparatus consists of four probes linearly arranged at a distance s from each other. The probe diameter is 1.5 mm and the spacing between adjacent probes is approximately 2.5 mm. The resistivity of the substrate is measured by measuring the induced voltage drop at the two inside probes when a constant current flows in the outer two probes, passing through the unknown resistance of the sample. In order to reduce leakage currents, an insulating material needs to be used as a boundary at the bottom of the semiconductor sample. It is well known that the resistivity for an arbitrary shaped sample, when using in-line probes with equal probe spacing can be calculated from [12]:

$$\rho = 2\pi sk\frac{V}{I} \tag{5.1}$$

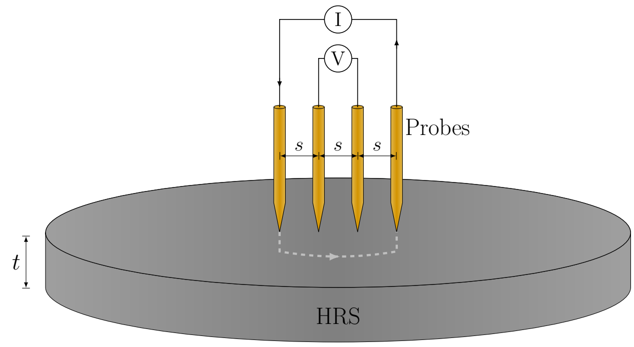

(a)

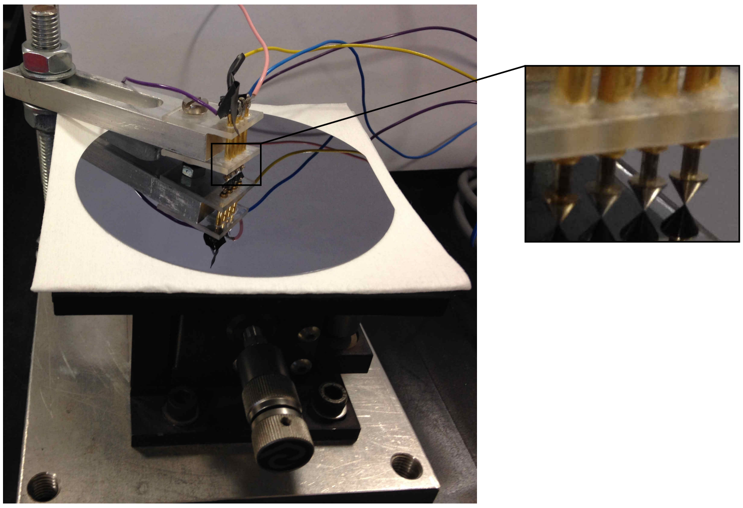

(b)

Figure 5.17: (a) Schematic configuration of a collinear four-probe array for resistivity measurements and (b) experimental setup of the four-point probe station.

where V is the measured voltage drop between the inner probes, I is the constant current source, s is the probe spacing and k is a correction factor. With the samples not being semi-infinite in either the lateral or the vertical dimension the calculated resistivity value must be corrected. Thus, the correction factor k is a function of the sample dimensions (i.e. thickness, diameter for circular samples or width for square samples). When the sample thickness is smaller than the probes spacing, with no significant interaction between thickness and edge effects, k can be assumed to be the product of independent correction factors:

$$k = k_1 k_2 k_3 \tag{5.2}$$

where k_1 is the correction factor for sample thickness, k_2 for sample dimensions, k_3 for probes placement relative to the sample's edges. With an insulating boundary at the sample's bottom surface:

$$k_1 = \frac{\dfrac{t}{s}}{2\ln\left[\dfrac{\sinh\left(\dfrac{t}{s}\right)}{\sinh\left(\dfrac{t}{2s}\right)}\right]} \tag{5.3}$$

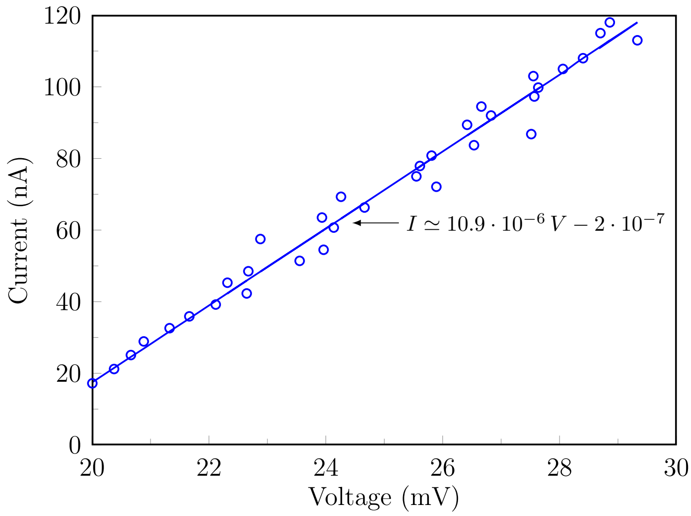

Figure 5.18: Measured current as a function of the voltage drop across the probes for a HRS wafer with 300 µm thickness.

Thus, for a thin sample (i.e. $t \leqslant s/2$) it can be assumed that $\sinh x \simeq x$ for $x << 1$ [12]:

$$k_1 = \frac{1}{2\ln 2}\frac{t}{s} \tag{5.4}$$

Moreover, the correction factor k_2 with regard to sample size can be applied. For a circular sample (e.g. silicon wafer) k_2 can be calculated as [12]:

$$k_2 = \frac{\ln 2}{\ln 2 + \ln\left[\dfrac{\left(\dfrac{D}{s}\right)^2 + 3}{\left(\dfrac{D}{s}\right)^2 - 3}\right]} \tag{5.5}$$

with $k_2 \simeq 1$ when the sample's diameter is $D \geqslant 40s$. In this case with $s = 2.5$ mm k_2 can be assumed to be unity as the diameter of the wafer being measured is 100 mm. Finally, if the probe distance from the wafer boundary is at least 3 to 4 probe spacings, it can be assumed that there is no interaction between the probes and the edges of the wafer and thus $k_3 \simeq 1$.

Thus, for a thin sample which satisfy the conditions for $k_2 \simeq 1$ and $k_3 \simeq 1$, (5.1) and (5.4) give [12]:

$$\rho = 4.532t\frac{V}{I} \tag{5.6}$$

Therefore, by extracting the slope I/V from Fig. 5.18. (5.6) gives the sample's resistivity with sample thickness t. Using the measurement setup shown in Fig. 5.17 the resistivity of a wafer (with initial indicated resistivity value of $>$ 10 kΩ·cm ±30%) has been measured before and after plasma exposure for an initial thickness of 500 µm and final thickness of 300 µm. In both cases the measured resistivity value was approximately 12.5 kΩ·cm.

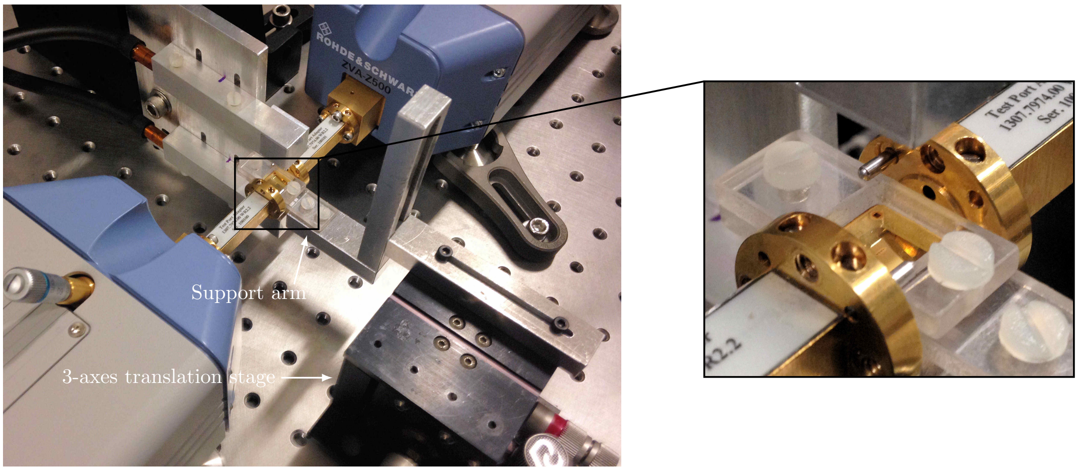

Figure 5.19: Experimental setup for measuring the frequency response of the prototypes with no flanges. A support arm extended from a 3-axis translation stage is used for alignment.

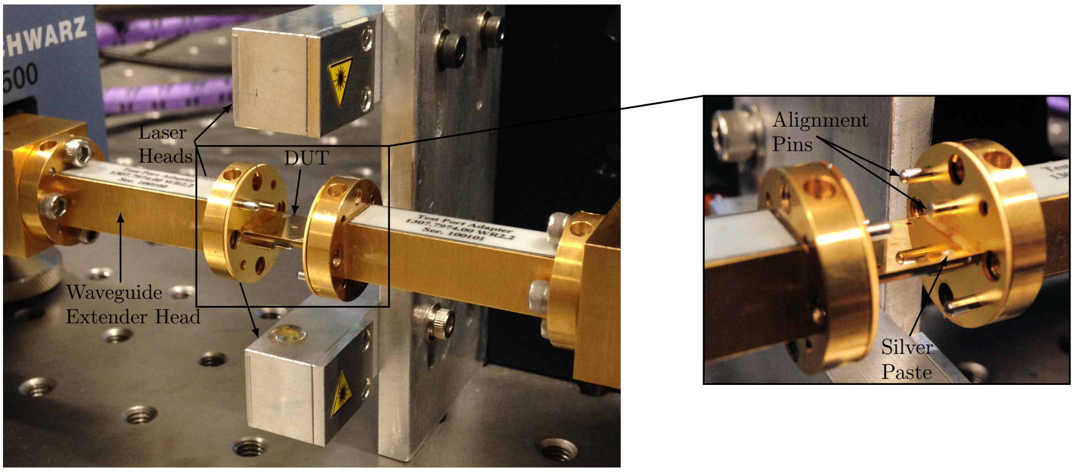

Figure 5.20: Experimental setup for measuring the frequency response of the prototype with the use of fabricated flanges for alignment.

5.3.2 Waveguide Measurements

In this experiment in order to measure the power loss of the fabricated prototypes two different experimental setups are used. In the first setup, the sample is mounted on a linear translation stage, with the use of a support plastic holder, providing x, y and z translation, as shown in Fig. 5.19. Although this setup provides three degrees of freedom, accurate alignment between the device and the Vector Network Analyser (VNA) heads is very difficult to achieve and hence an insertion loss of approximately 10 dB is measured across the frequency band from 0.325 THz to 0.5 THz.

Aiming for an improved alignment between the extender heads and the device under test, a different approach is used. In this case flanges, having the same size as the flanges of the extender waveguide heads, are fabricated from bulk silicon wafers and are coated with chromium and gold as explained earlier. Alignment between the device and the extender heads is obtained using the fabricated flanges, as they include pin holes which are used for alignment with the flanges of the VNA heads (Fig. 5.20). Moreover, the two laser heads are

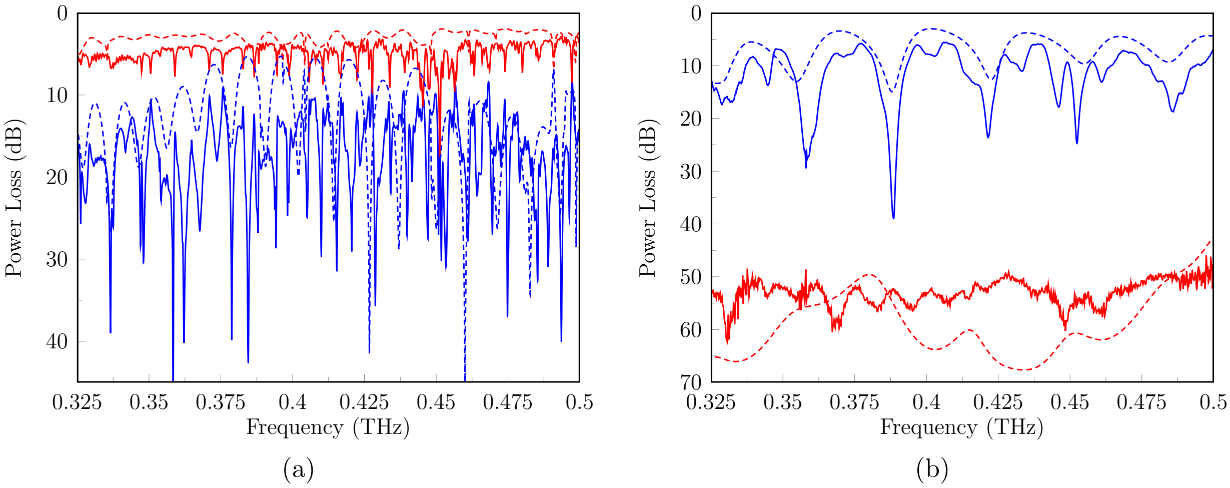

Figure 5.21: Reflection (blue curves) and transmission (red curves) characteristics of a prototype with four circular holes with diameter of 70 µm etched in both broad waveguide walls. (a) Without laser illumination and (b) with laser illumination. Solid lines: Measured results. Dashed lines: Simulated results.

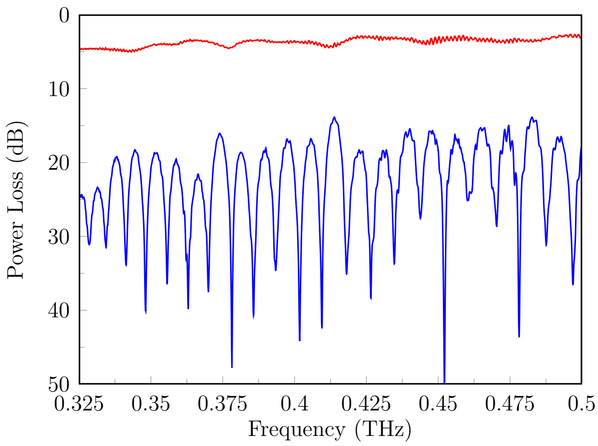

Figure 5.22: Measured results for the reflection (blue curve) and transmission (red curve) characteristics of a WR-2.2 air-filled waveguide prototype. Four circular holes with diameter of 50 µm are etched in both broad waveguide walls.

mounted on a mounting angle bracket so that the spot size on the sample can be adjusted. An IR microcamera and a mirror are used in order to view the illumination spots on both sides of the sample. The power loss (transmission and reflection characteristics) of different samples is measured through fully calibrated measurements (SOLT). The results are shown in Fig. 5.21.

As can been seen, an ON-OFF ratio of approximately 45 dB across the whole frequency band is obtained. Also, a good agreement between the measured and simulated results (obtained from CST Microwave Studio) is shown. When the device is not illuminated, an insertion loss of approximately 5 dB is shown. This power loss can mainly be attributed to the misalignment between the device and the extender heads and the poor electrical contact between the heads and the device since they are not bolted together in our setup. Specifically,

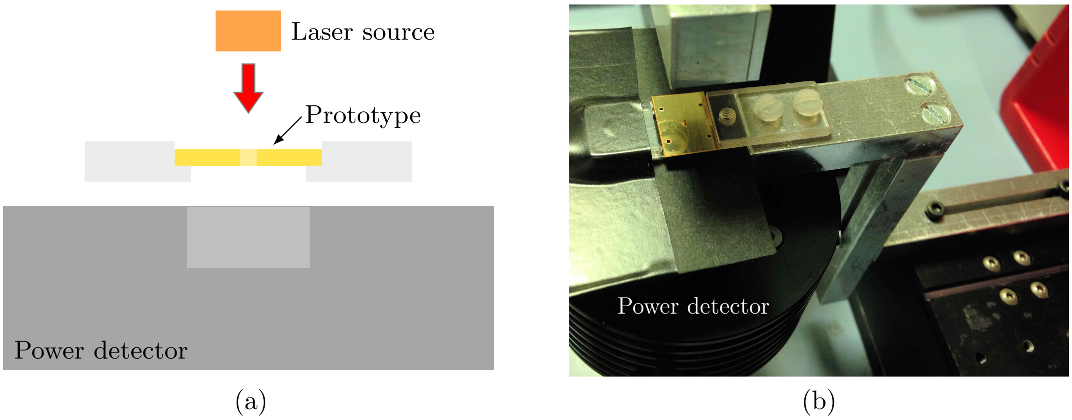

Figure 5.23: Experimental setup used to measure the laser power. (a) Schematic and (b) illustration.

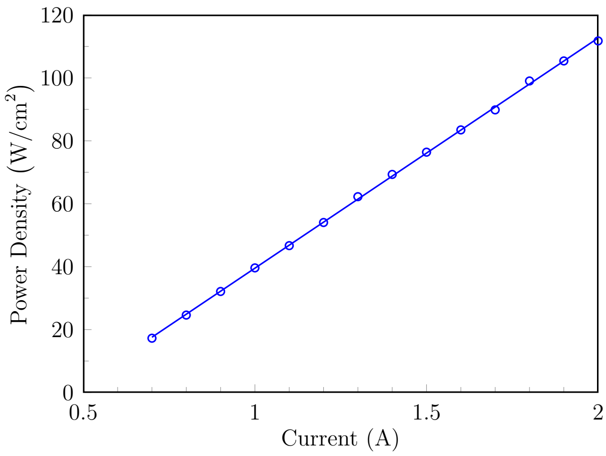

Figure 5.24: Measured laser power density using the experimental setup in Fig. 5.23.

when the device is mounted on the heads with the flanges, a small air gap is introduced at the interface, which results in a further increase of power losses. As can be seen in Fig. 5.22, where the measured reflection and transmission characteristics of a reference air-filled waveguide are presented, the insertion loss is approximately 4.5 dB.

It is also interesting to note that by using HRS as the photoconductive material, a high photo-induced carrier density can be obtained inside the slab, due to its characteristics and mainly due to the longer carrier lifetime, when compared to other semiconductors. On the other hand, the switching speed of the device is limited by the long carrier lifetime of the HRS material, with the switching time between the ON and OFF state being dependent on the charge carrier lifetime. Specifically, for a HRS this time is approximately 1 µs.

In this experimental setup, a large laser spot (which is estimated to be approximately 3 mm) is used, in order to illuminate all four circular holes etched on each waveguide wall. Thus, only a fraction of the incident laser beam is actually absorbed in the HRS slab and contributes in the photogeneration of free carriers inside the HRS slab, with the rest being reflected from the gold surface of the waveguide wall. The laser power which contributes to the photoexcitation of the HRS slab is measured with a power meter detector in the experimental setup shown in Fig. 5.23. As can be seen in Fig. 5.24, the power density increases linearly with increasing current and specifically, for a laser current range of 0.7 A to 2 A a power density range from 18 to 115 W/cm^2 is measured.

5.4 Conclusion

In this chapter the fabrication and experimental validation of the THz optically-controlled waveguide switch prototypes are presented. All the fabrication and assembly steps for the development of the prototypes are explained in detail. A further discussion of the challenges involved during this process as well as during the testing of the devices is presented. A high ON-OFF ratio is achieved with good impedance matching highlighting the good accuracy levels both at the fabrication and assembly of the devices.

References

[1] J. W. Bowen, S. Hadjiloucas, B. M. Towlson, L. S. Karayzas, S. T. G. Wootton, N. J. Cronin, S. R. Davies, C. E. McIntosh, J. M. Chamberlain, R. E. Miles, and R. D. Pollard, "Micromachined waveguide antennas for 1.6 THz", *IET Electron. Lett.*, vol. 42, no. 15, pp. 842-843, Jul. 2006

[2] A. Pavolotsky, D. Meledin, C. Risacher, M. Pantaleev and V. Belitsky, "Micromachining approach in fabricating of THz waveguide components", *J. Microelectr.*, vol. 36, no. 7, pp. 683-686, Jul. 2005

[3] C. D. Nordquist, M. C. Wanke, A. M. Rowen, C. L. Arrington, M. Lee and A. D. Grine, "Design, fabrication, and characterization of metal micromachined rectangular waveguides at 3 THz", *Int. Symp. Antennas Propag.*, pp. 1-4, Jul. 2008

[4] M. A. Jackson, "Micro and nanomanufacturing", *Springer*, 2007

[5] http://www.freepatentsonline.com/5501893.html

[6] M. Madou, "Fundamentals of microfabrication : the science of miniaturization", 2nd ed., *CRC Press*, 2001

[7] D. Lishan, R. Westerman, S. Lai, M. DeVre, D. Purser and D. Johnson, "Process and equipment challenges for MEMS deep silicon etching", *Micro 2003 - DSC*, Aug. 2003

[8] K. E. Bean, "Anisotropic etching of silicon," *IEEE Trans. Electron Dev.*, vol. 25, pp. 1185-1193, 1978

[9] B. Wu, A. Kumar and S. Pamarthy, "High aspect ratio silicon etch: A review", *J. App. Phys.*, vol. 108, no. 5, p. 051101, Sep. 2010

[10] Microchemicals, "Photolithography: Theory and applications of photoresists, etchants and solvents", 2012

[11] Neutronix-Quintel, "Users guide for Quintel mask alignment system Q4000", 2000

[12] D. K. Schroder, "Semiconductor Material and Device Characterization", 3rd ed., *Wiley*, 2006

Chapter 6

Conclusions and Future Work

In this work, a novel optically controlled THz switch was presented as an illustrative component of a more general approach to implementing optically controlled reconfigurable structures with the use of MPRWG components. The complete physical behaviour of the switch has been studied in great detail whereas prototype devices, validating its behavior, have been fabricated with their associated challenges being identified and discussed.

In order to obtain accurate and meaningful full-wave electromagnetic simulations a thorough investigation of the various modelling approaches in commercial software packages has been undertaken. This was necessary in order to fully explore their limitations and provide guidelines, as well as deeper insight, in the modelling of arbitrary structures. With, this exhaustive study, newcomers to the field of numerical EM simulators, as well as experienced designers, will be able to predict the performance of passive metal-based THz components with more confidence in the generated results.

Moreover, the photoconductivity effects have been studied independently first and then in conjunction with the propagating electromagnetic wave. The inhomogeneous photoconductivity inside a high resistivity silicon slab has been characterised and an accurate discretisation of the photo-induced plasma regions is presented. Also, the thermal characteristics of such devices have been studied in conjuction with the illuminating power. The temperature distribution has been presented providing deeper insight. Finally, with manufacturing tolerances having a significant effect on the device performance at the terahertz frequency range, the fabrication process has been presented in great detail with a view to highlight potential issues; the most appropriate methodologies have been proposed and explained. Additionally, the alignment challenges during the experimental setup have been discussed with two different alignment methods being compared and contrasted. As it has been shown, even small misalignment offsets may result in significant compromise in the device performance.

The presented technique can be applied as a generic approach to implementing novel real-time tunable terahertz components such as power splitters, phase shifters, absorbers and antennas. Hence, real-time tunable systems can easily be realised by employing such components. Moreover, this method is inherently suited for fully integrated circuits where the systems are patterned onto a HRS wafer. However, in this case the close proximity of structures would make such systems more vulnerable to interference. As a result, an investigation on the compromise in performance and limitations posed by interference would be useful in order to optimise the design of integrated applications.

An alternative method to the metal-based waveguides for the guidance of THz radiation, is the use of dielectric waveguides (similar to optical fibers). With ongoing research on identifying sufficiently transparent materials at the terahertz frequency range (e.g. polymers), dielectric-waveguides exhibiting low absorption losses could be adapted.

A different direction for further work would be the use of laser illumination to control in real-time the pattern of metamaterials. With metamaterials having received a great interest in recent years, this approach would offer the opportunity to change the geometric characteristics (i.e. pattern) of the metamaterial structure resulting in a real-time optically control response.

Alternatively, different illumination techniques can be studied in order to explore their characteristics. For example, various modulated laser sources can be employed to investigate the photoconductivity effects.

At terahertz frequencies the natural approach to manufacture this type of devices is using cleanroom microfabrication techniques because of their accuracy and low tolerance characteristics. However, a potentially strong candidate for cheap solutions in the future would be 3D printing. Although this method is still in its infancy and currently limited by the features size, in principle it could be used to create cost-effective components.